

# **Working Up Hills: Dynamics Over Sloping Topography With Bottom-Enhanced Diffusion**

**Benjamin W. Diehl**

Submitted in partial fulfillment of the  
requirements for the degree  
of Doctor of Philosophy  
in the Graduate School of Arts and Sciences

**COLUMBIA UNIVERSITY**

2012

©2011

Benjamin W. Diehl

All Rights Reserved

## ABSTRACT

# Working Up Hills: Dynamics Over Sloping Topography With Bottom-Enhanced Diffusion

**Benjamin W. Diehl**

The deep ocean circulation is known to have influence even at the surface, through means such as the Meridional Overturning Circulation (MOC). Initial theories on abyssal circulation and mixing have been improving, based on observation of both physical and numerical experiments. By tracing this progression, key aspects are identified but the explanations and relationships between them still contain gaps. Vertical diffusivity is one such component known to influence the strength of the MOC and is a part of the least understood leg of that circulation. Observations in particular have identified intense regions of mixing occurring near, and likely caused by, rough topography. Though the pieces are all present from this brief description, the exact relationships between them are still unclear, and observations cannot fully be generalized without more direct knowledge of how the phenomena interact.

With these issues in mind, two models were used for simulating two dimensional abyssal canyons having constant sloping topography and bottom-intensified mixing acting on an initial uniform stratification. The first model uses finite volumes on a uniform z-coordinate grid, and it was set up and used to verify general sensitivity and confirm the choice of experimental variables while keeping the rest constant in a base state. The second model, developed specifically for use in this investigation, employed finite element techniques with a nonuniform mesh. A variational problem was created from derived streamfunction-vorticity equations plus advection-diffusion of a sole tracer, potential temperature. Preliminary simulations confirmed that both models were capable of simulating the desired phenomena, notably an upslope flow along the topography, and had otherwise comparable results.

Two diagnostics were used for analyzing both models: the minimum value of streamfunction is a proxy for flux of a bottom boundary layer, and an estimate of thickness for the bottommost layer is a minimum length of communication into the fluid interior. These two diagnostics were studied in relation to changes in the amount of bottom enhanced mixing and also to changes in slope angle of the underlying topography. The boundary layer thickness increases with slope angle, a trend thought to continue well beyond tested values. Likewise, the streamfunction minima closely follow a linear relationship determined by the maximum diffusivity. Additionally, the variability within the values for both diagnostics are seen to decrease in response to either diffusivity decreases or slope length increases. Tangent investigations focusing on slope length and effects of periodic domains add support to the results as well as demonstrate potential robustness of the identified trends. With this restriction in mind, all slopes (0.0025-0.0075) and diffusivities (0.05-0.3 $m^2/s$ ) generate intense layers over 100m high with over 0.1Sv of up-slope flow, comparable to that observed in along-canyon flows.

# Table of Contents

<b>1</b>	<b>Introduction</b>	<b>1</b>
<b>I</b>	<b>Theory and Model Formulation</b>	<b>13</b>
<b>2</b>	<b>Background and Equations</b>	<b>15</b>
2.1	Meridional Overturning Circulation . . . . .	15
2.2	Boundary Mixing and Dynamics . . . . .	17
2.3	Equations . . . . .	22
<b>3</b>	<b>Finite Differences: The MITgcm</b>	<b>25</b>
3.1	Equations and Parameterization . . . . .	25
3.1.1	Discretization and Algorithms . . . . .	29
3.2	Diagnostics and the Base Case . . . . .	32
3.3	Other Checks . . . . .	38
<b>4</b>	<b>Finite Elements: The FEnICS Project</b>	<b>45</b>
4.1	Equations . . . . .	45
4.1.1	Strong $\psi - \omega$ Form . . . . .	45
4.1.2	FEniCS Equations . . . . .	47
4.2	FEniCS Components and Equation Implementation . . . . .	51
4.3	Preliminary Examination . . . . .	54
4.3.1	First Simulation . . . . .	54
4.3.2	Resolution . . . . .	59

<b>II Analysis and Discussion</b>	<b>65</b>
<b>5 Results and Analysis</b>	<b>67</b>
5.1 Model Comparison . . . . .	67
5.2 Model Diagnostics . . . . .	71
5.2.1 Diffusion . . . . .	72
5.2.2 Topography . . . . .	76
5.2.3 Slope Length . . . . .	81
5.3 Further Directions . . . . .	85
5.3.1 Upper Cells . . . . .	85
5.3.2 Periodic Domain . . . . .	88
<b>6 Summary and Discussion</b>	<b>97</b>
<b>Bibliography</b>	<b>102</b>

# List of Figures

1.1	Schematic for Stommel’s theory of deep circulation. This shows two generation points, cyclonic flow across each basin, and western intensified flow connecting the basins [Stommel 1958]. . . . .	2
1.2	Zonal section of diffusivity in the Brazil Basin, shown with a nonuniform colorscale. Comparing to the topography, in black, low diffusivity aligns with smooth topography on the left, while the more intense diffusivities occur over the rougher region on the right. The larger diffusivities extend hundreds of meters into the water column [Polzin <i>et al.</i> , 1997]. . . . .	5
1.3	Observed dissipation profiles from a tracer experiment in the Brazil Basin as plotted by Ledwell <i>et al.</i> [2000]. The topography is shown for the longitude where the tracer was injected, 18.5°W. The exponential diffusivity profile described in the text is proportional to these profiles. . . . .	6
1.4	Diffusion profiles from a meridional transect in the South Atlantic [Polzin <i>et al.</i> , 1997]. The offset between profiles aligns them roughly above the physical location they were taken relative to the topography, shown in black. The bottom enhanced diffusion has a definite exponential component. . . . .	7



2.2 Pictured are two methods to visualize the creation of a bulk flow up a sloping boundary induced by diffusion of a stably stratified fluid. On the left the isopycnals are shown curving downward to satisfy a no-flux boundary condition. This creates a situation on the boundary with a horizontal gradient that allows the fluid to move toward and up the slope. On the right, arrows A-C indicate mass fluxes caused by vertical mixing. In order to maintain B another flux at D must be established [Phillips, 1970]. . . . .	18
2.3 Force diagram of stratified fluid over sloping topography. Solid line is the density contour which is horizontal in the interior, a line extended to the boundary with dashes. In curving to meet the boundary it not only creates the pressure forced up-slope flow which was the focus of Phillips but also a countering downward buoyancy forced flow. Also included is the possible geostrophic current that would result in an along-slope component. . . . .	20
3.1 Diagrams of the discretization methods. a) Shows the Arakawa C-grid which staggers the placement of velocities and other tracers. The horizontal velocities are located in the east/west cell faces, the vertical velocities in the top/bottom faces, and other tracers in the center of each cell formed by specified nodes. b) Shows a method of allowing the boundary to intersect the grid. The height is specified at the cell boundaries and the center, here $h_w$ and $h_c$ indicate the fraction of the west cell face and the center in the fluid interior, which augments the finite volume being considered at these places. . . . .	30
3.2 The MITgcm output after one day of simulation initialized with the base case parameters. The left shows the horizontal velocities, while the middle shows the same for the vertical. In combination it is clear that an upslope layer has already formed. The right shows potential temperature, with the contours drawn every $0.02^\circ$ clearly dipping to meet the boundary. . . . .	33

3.3 Streamfunction of initial parameters at 20 days. The green circles show where the streamfunction is at its minimum for each column above sloping topography excluding a buffer region near the boundary. The layer height for each column is the distance of this location above topography, and the average of all columns' heights is defined as the diagnostic $\delta$ , written within the sloping region. . . . .	35
3.4 Plots showing the development of the upslope layer over time for the base case. The top plot shows $\psi_{min}/100$ and the extrema of velocities versus time. The left column shows streamfunction, the middle horizontal velocity and the right vertical velocity at times of 1, 7, 20, and 50 days. This reveals a bottom layer forms and quickly reaches maximum strength, after which it slowly weakens. . . . .	36
3.5 Shows the interface between cells at three horizontal resolutions. These three plots are all from the 20day timestep of runs with a 400m and $\kappa_{max} = 0.3m^2/s$ . Grid spacing is shown with black circles for horizontal spacings of 200, 750, and 1000m from left to right. This demonstrates the direct dependence on the grid, for this numerical phenomena. . . . .	37
3.6 Shows an array of streamfunction plots testing the labeled parameters. All plots shown are at 20days and vary from the base case only in the way described; a) Base case has no changes, b and c) the 400m rise is translated up(down) to increase(decrease) the length of the sloping region, d) the decay scale of $\kappa_{max}$ is halved, e) the domain is extended upward, and f) hydrostatic balance is assumed. All the variations shown have visible effects, besides that of hydrostatic balance. . . . .	40

3.7 Shows sensitivity to viscosity coefficients, noting that $\kappa_h$ is almost identical to $\nu_h$ . The columns are $\psi$ , U and W. The rows are of simulations with $\nu_h$ 100 times higher than lower, then the same changes to $\nu_v$ . While the horizontal coefficients have almost no effect, vertical viscosity plays a huge part in suppressing or allowing the vertical waves seen at the grid scale. . . . .	43
4.1 Shows $\psi_{min}$ vs time along with plots of streamfunction near the spinup of 20 days. The circles on the green line indicate the times where snapshots are shown. The nine snapshots are labeled by the number of days elapsed in simulation, progressing two days at a time, from left to right then top to bottom. The normal spinup is centered showing the scale all plots have. Within the 16 days displayed, an upper negative cell makes two full oscillations of the domain length, demonstrating the transience of this upper region. . . . .	55
4.2 Shows timeseries for streamfunction minima for a variety of simulations. The diagnostic $\psi_{min}$ was calculated as normal for a variety of simulations. Except for the ones noted in the legend, all values are from the base case. The first three simulations, in green, blue and red, show rises of 200, 400, and 600m at base diffusivity of $\kappa_{max} = 0.1m^2/s$ . The last two, in yellow and cyan, show the base rise of 400m with lower and higher diffusivities. All series were shifted by a constant so that the value of $\psi_{min}$ was 0 at 20 days. . . . .	57

4.3 Shows the base simulation at 20days with different meshes. The simulations were of the base case with $\kappa_{max} = 0.3m^2/s$ and meshes with different levels of refinement. Streamfunction is plotted the mesh is visible in extension above each plot. Starting with m0) a coarse mesh with 20 nodes per side, the resolution is doubled once (m1), twice (m2) and finally a third time (m3). The nonuniform refinement focuses on the top boundary where the interfacial perturbation seems to begin (n4) and then doubles that resolution (n5). See text for details. . . . .	61
4.4 Shows two methods of further investigating the oscillation between streamfunction cells. The left displays the wave-height in terms of both the main independent variables. Here, the larger oscillations are seen to occur at higher slopes and diffusivities in general, yet there are cases such as central slopes at highest diffusivity where small amplitudes are found. The right plot shows the same wave-height with respect to a derived horizontal velocity, found from $\psi_{min}$ . The lack of apparent correlation further emphasizes the absence of straightforward explanation. . . . .	62
5.1 Shows streamfunction snapshots at 20 days with the base case parameterization, as simulated by both the MITgcm and FEniCS. The bottom cell is extremely similar qualitatively between the two simulations. The upper cells show some differences that can be attributed to the temporal variability of the upper cells. . . . .	69
5.2 The effects of diffusion when the rise in topography is held constant at 400m. The diagnostics were calculated from six simulations all after 20 days of spin-up. The blue curve shows the dependence of the streamfunction magnitude is approximately linear. The green curve shows the influence on the layer height diminishes as diffusivity increases through the range. . . . .	72



5.6 A normalization of $\psi_{min}$ plotted against the rise of the topography. The colors separate the data into four series based on $\kappa_{max}$ and were normalized as such. The $\kappa_{max}$ -series have each been shifted by their means and then weighted by the standard deviation to reveal the similarity between the curves, independent of scale. The coefficient of variance for each series is listed as also show a clearly decreasing trend with diffusivity. . . . .	79
5.7 Layer thickness as a function of slope. Diffusivities are indicated by color across the whole array of slope angles. A linear trend was found for each and plotted with a dashed line. While three cases are approximately linear, the weak diffusivity not on shows a different form but even has a smaller layer at the steepest slope. . . . .	80
5.8 Three streamfunction plots with different size domains. The base case streamfunction is shown in the center, b. The case to the left and right have a smaller and larger Ra respectively, by a factor of 8, so that the length scales are both halved and doubled. The small case, a, shows a definite decrease in $\psi_{min}$ while only having one large cell. While the large domain, c, does show even more complexity than usual in the extra room above topography, the most significant aspect is the more intense upward flow. . . . .	82



- 5.12 Streamfunction snapshots from four periodic domain simulations. These plots are all at the 20 day mark, allowing for the normal spin-up, and have the color scheme used in previous streamfunction plots. They have four separate values for limits on colors adapted to the individual snapshots extrema. The periodic simulations show more waves at the interface than the slope-type models even with their meshes refined at the center. The right-slope has a stronger bottom cell on all of them but there are cases of the right and left cell being the one to flow over the peak as well as cases where they appear to meet at the peak. . . . . 91
- 5.13 Repeats two previous figures adding data from periodic-domain simulations. A)The left figure shows that the linear trends from the slope-type model holds for the simulations when just considering the right half of the periodic domain. Circles show the slope-type simulations and their linear regression, pluses show the periodic data. Slope angles for the simulations are relative to rises of 200, 300, and 400m. In addition the slope of the linear regressions are shown for each. B) The right plot repeats a topographic dependence and while showing significant difference shows the ridge-type model has the extrema consistently shallower than the slope-type. . . . . 94

# Acknowledgments

I would like to express my most sincere gratitude for my advisor, Dr. Andreas Thurnherr, for all the guidance and support he offered, which was so happily given and received. Simply discussing the problems with him never failed to renew and strengthen both my interest and motivation toward research. I was continually impressed by this and his general helpfulness.

I would also like to thank the additional members of my committee Prof. Marc Spiegelman, Prof. Adam Sobel, Prof. Tamay Ozgokmen, and Prof. Lorenzo Polvani. All of whom offered invaluable guidance, suggestions and encouragement; from teaching me the fundamentals of fluid mechanics and numerical modeling, to reassurances about departmental procedures, to asking enlightening questions leading me down paths I would not have thought to consider otherwise.

For the entire length of my graduate experience I was funded by the U.S. National Science Foundation: as a fellow of the IGERT Joint Program in Applied Mathematics and Earth and Environmental Science and by Grant OCE-0751967.

In addition, I would like to mention my gratitude to my fellow APAM classmates as well as those from DEES, especially Ophir Gaathon and Xinfeng Liang. The friendships and support were a vital part of all I accomplished over these past years. From seemingly mundane conversations that allowed a refreshing break from studying, to honest responses helping me gain a better perspective; all of the interactions were appreciated.

Of course the support from my family has been an immeasurable help, through the graduate school process and my entire life leading up to it. My mom, dad, and sister must be thanked most, especially for their lack of frustration when continually hearing about the stress from research troubles and writing trials. Thank you.



# Chapter 1

## Introduction

When most people think of the ocean, waves, surf, and shells are mostly what comes to mind. Thoughts will also give a sense of vast areas of water and of a habitat for many unique creatures. Living in an age where environmental awareness is constantly increasing, more and more might think about the relationship to climate as well. Even with this increased awareness, it is rare that descriptions will go much below the surface. Understanding the ocean and its dynamics can draw many parallels from this lay-person thought. For a long time the ocean was considered little more than an aquatic-surface or a slab of water. Yes, it was known to be very deep, and often efforts were made to discover what biology exists below, out of sight, as well as attempts to map the topography. Still, the existence of depth would be insignificant if the ocean were just vast emptiness. Originally when the only forcing was assumed to be wind, the simple lack of proximity implied the depths are stagnant and therefore not interesting nor important.

The assumed unimportance of the ocean depths has been diminishing as more is discovered, whether the findings are about the ocean itself or findings that are related to it. So often discoveries are spurred by need: submarines traversing the depths (WWI, 1915) and cables (TAT-1, 1958) spanning the oceans demanded knowledge of topography. As climate models advanced it was quickly understood that a slab ocean was not enough, and by the late 1960's NOAA's Geophysical Fluid Dynamics Laboratory had developed the first coupled ocean-atmosphere climate model



Figure 1.1: Schematic for Stommel’s theory of deep circulation. This shows two generation points, cyclonic flow across each basin, and western intensified flow connecting the basins [Stommel 1958].

[NOAA, 2011]. While interest has increased and changed general notions, some ideas have persisted since their formulation.

The basis to modern deep ocean circulation theory was largely developed in the late 1950s and 60s. Stommel proposed a theory based on thought experiments on deep water formation and geostrophy [Stommel, 1958]. Starting with an estimate on what upward velocities are present, it was assumed that the opposing deep-water formation points are very localized. The dark circles in the Weddell Sea and North Atlantic in Figure 1.1 are just such points, and are supported from observations. Geostrophic balance suggests the flow connecting the large area of upward velocities and local sinking must be poleward everywhere but at the equator, as is pictured. Finally, western boundary currents are placed as needed to finish the schematic. In collaboration with Arons, Stommel expanded these ideas into a model for stationary flow patterns in a series of papers [Stommel and Arons, 1960a; 1960b; 1972]. As is visible in the schematic (1.1), the poleward flows plus imposed western boundary currents result in basin-wide cyclonic flows. This picture of deep circulation is

described for its prevalence even though the authors admitted on creation that it includes oversimplifications that are unrealistic.

Investigation into average vertical velocities of the ocean, similar to that required in the Stommel schema, have been performed, such as the now classic calculation of Munk [1966]. Munk started by reducing the standard advection-diffusion equations to a two-term equation for the vertical in steady state,

$$\kappa_v \frac{\delta^2 c}{\delta z^2} + w \frac{\delta c}{\delta z} = 0. \quad (1.1)$$

The coefficient of diffusivity of heat in the vertical is represented by  $\kappa_v$ , vertical velocity is  $w$ ,  $z$  is the vertical coordinate, and  $c$  represents concentration of a given tracer. Having reduced the governing equation to this two term form, determining the remaining free parameters requires exactly two tracer profiles. The first pair of tracers used were salinity and potential temperature, which each determined a scale height,  $\kappa/w$ , since they have independent diffusivities. The scale height was found by fitting an exponential to the given tracer profile, and while not confirming Equation 1.1 the fit is consistent. Additional chemical tracers, including  $^{14}C$  and  $^{226}R$ , allow unique determination of velocity and diffusivity due to the addition of a decay constant to the RHS of (1.1) and so having solutions of a different form. Together these four tracers were consistent in determining both  $w$  and  $\kappa_v$ , producing the values of  $w = 1.4 \times 10^{-7}$  m/s and  $\kappa_v = 1.3 \times 10^{-4}$  m<sup>2</sup>/s. Additional confirmation for the vertical velocity was then obtained by showing that estimates of deep water formation are comparable. These values are often quoted in general when referring to vertical dynamics in the ocean but do not include lateral processes nor data from the bottom or topmost 1km of the ocean. They are only representative of a basin-wide average for mid-depths.

While care must be taken to use values like this properly, investigation of driving mechanisms can take advantage of them, as a starting point for studies. One such study used an idealized three dimensional basin to study the meridional overturning [Marotzke and Scott, 1999]. The numerical model was used to compare the influence of downward convection efficiency and diapycnal mixing rate on the strength of the overturning. By independently varying these opposite legs of an overturning circu-

lation, it is shown that the upward flux is more important in determining the rate of the entire cycle. Though previous studies had already shown that the vertical mixing was a factor for determining the strength of meridional overturning, [Bryan, 1987; de Verdiere, 1988], the described study also shows that the overturning's strength is insensitive to the efficiency of the downward convection [Marotzke and Scott, 1999]. With both sides of this argument investigated, Marotzke and Scott's [1999] result adds even more significance to the vertical diffusivity and its effectiveness.

Estimated values of vertical diffusivity as well as vertical velocity, in combination with a schematic for the global flow patterns, may give the impression of deeper knowledge about the ocean depths than exists at this point. Looking at data from the World Ocean Circulation Experiment, Hogg and Owens [1999] report some deviation from Stommel-Arons theory predictions. The data from neutrally buoyant floats released in the Brazil Basin in the 1990s are supportive of deep western boundary currents existing, yet similarities to Figure 1.1 fade as focus moves away from the boundary. Key differences observed are that the flow is largely zonal, and the predicted poleward component cannot even be identified consistently. Hogg and Owens [1999] propose that the zonal tendency could be related to mixing over the mid-ocean ridge (MOR).

The MOR has been a dominant feature in related studies which begin to rectify Stommel's original neglect of all topography. One such study, much in line with Hogg and Owens' [1999] proposal and revealing distinctly different dynamics than the previous schematic (1.1), was done by Huang and Jin's [2002]. They used a numerical model representing a large area in the south Atlantic including topography. Their domain includes two basins: the Brazil and Angola basins separated by a realistic MOR. Several mixing profiles were specified over the MOR only while the outer half of each basin had a lower background level. Even with a constant low mixing profile throughout, the result was contrary to the predicted Stommel-Arons flow. Strong currents formed following the MOR and inducing anticyclonic flow in both basins [Huang and Jin, 2002]. These results show importance of mixing and emphasize how vital topography can be in determining flows.

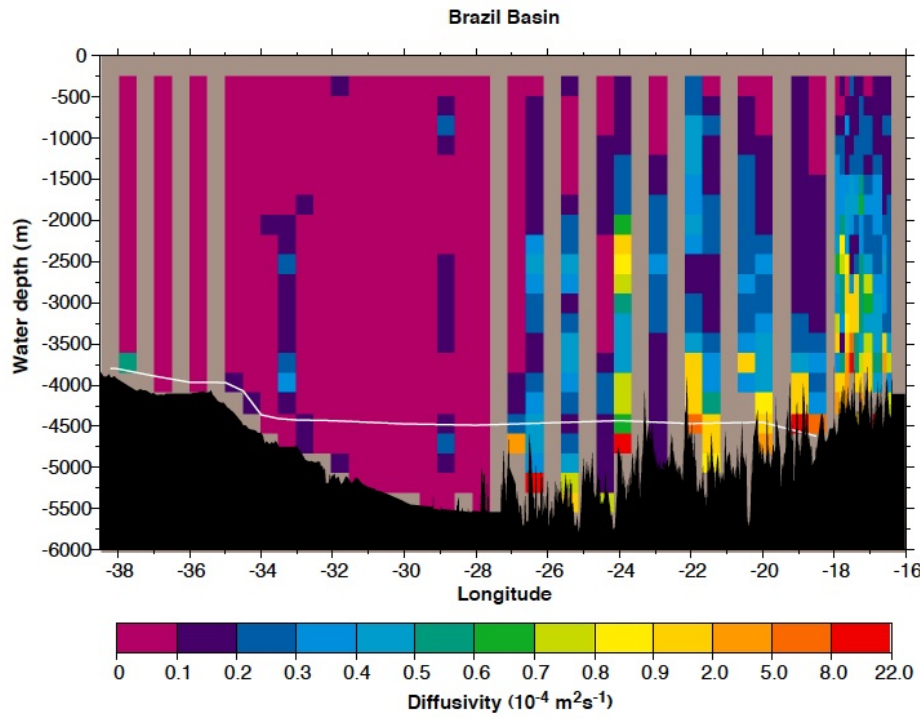


Figure 1.2: Zonal section of diffusivity in the Brazil Basin, shown with a nonuniform colorscale. Comparing to the topography, in black, low diffusivity aligns with smooth topography on the left, while the more intense diffusivities occur over the rougher region on the right. The larger diffusivities extend hundreds of meters into the water column [Polzin *et al.*, 1997].

With this importance in mind, observations near mid-ocean ridges will be further emphasized. These submerged mountain ranges are defining features of their ocean basins and consist of regions of rough topography that can generate turbulence as they interact with tides and other flow [St. Laurent *et al.*, 2001]. Any locally enhanced diffusivity, when integrated over the large scale of these ridges, has the potential to be significant in the global averaged diffusivity. A good example of the increased diffusivity related to the mid-ocean ridges can be seen in Figure 1.2, from Polzin *et al.* [1997]. The data presented is taken from two separate zonal cruise passes across the South Atlantic Basin, with bathymetry, shown in black, from the eastward track when west of  $-32^\circ$  and from the westward pass for the remainder.

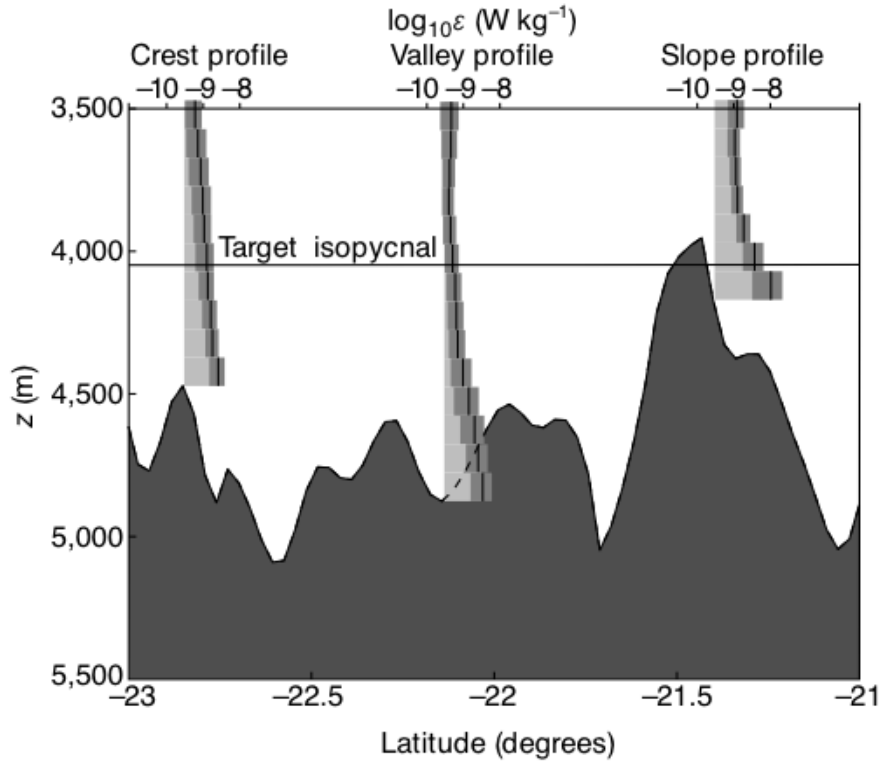


Figure 1.3: Observed dissipation profiles from a tracer experiment in the Brazil Basin as plotted by Ledwell *et al.* [2000]. The topography is shown for the longitude where the tracer was injected,  $18.5^{\circ}\text{W}$ . The exponential diffusivity profile described in the text is proportional to these profiles.

The diapycnal diffusivity is inferred from microstructure velocity measurements and displayed using a nonuniform color scale. Only the intense values are affected by this, so the values in reds and yellows are far greater than similar color steps in the calmer regions. This method of plotting still portrays the dramatic increase in diffusivity over the ‘rougher’ topography, which extends upward hundreds of meters over most of that region.

Individual dissipation profiles taken over rough topographic areas with the Brazil Basin show a distinct, if not unexpected feature (Figure 1.3). Bottom intensification is not surprising as Figure 1.2 shows similar in the diffusivity field. The dissipation profiles shown, from [Ledwell *et al.*, 2000], are moving from a more southern profile

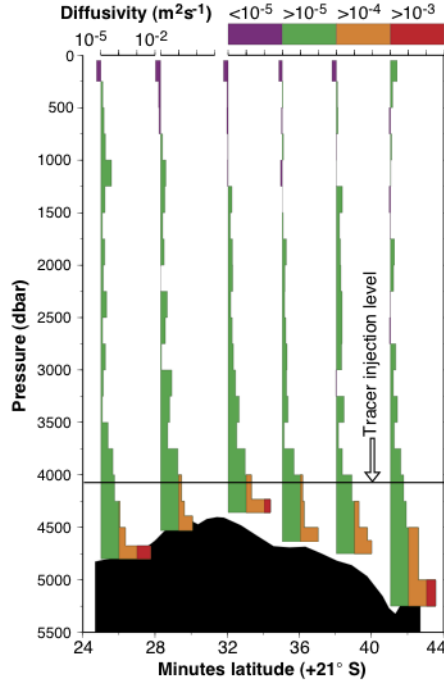


Figure 1.4: Diffusion profiles from a meridional transect in the South Atlantic [Polzin *et al.*, 1997]. The offset between profiles aligns them roughly above the physical location they were taken relative to the topography, shown in black. The bottom enhanced diffusion has a definite exponential component.

positioned over a crest, left of the figure, to a northern profile taken over sloping topography, on the figure's right. All three show stronger dissipation at the topography with the rightmost two resembling exponentials. While the rightmost profile indicates exponential decay most strongly, the center also resembles this form and is most relevant to this study, being located above and within a canyon. Some calculation must be done to apply this trend in dissipation to diffusion, but the general equivalence between the two has only a few components; the usual form, as in Ledwell *et al.* [2000] is

$$\kappa = \frac{\Gamma\epsilon}{N^2}.$$

Here  $\kappa$  is diffusion,  $\epsilon$  dissipation,  $\Gamma$  is a mixing efficiency set to an experimentally derived 0.2 [Turner, 1979] and  $N^2$  is the observed mean buoyancy frequency. If  $N^2$  was constant, this equation would be a simple proportionality; even with spatial dependence, buoyancy frequency changes slowly enough that the exponential form of dissipation still passes through to diffusion. Another set of observations directly shows the exponential nature of diffusion, Figure 1.4. Here a logarithmic scale has

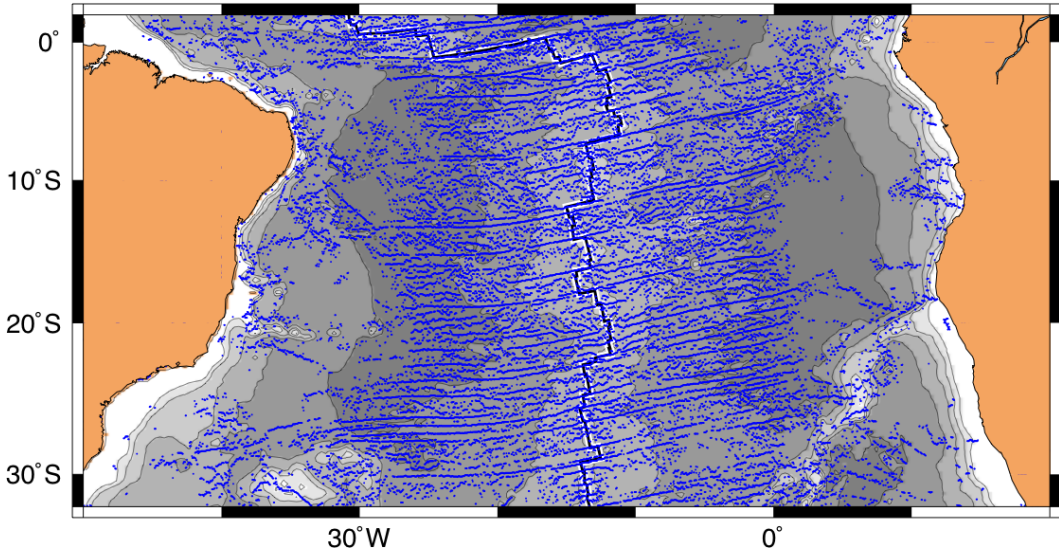


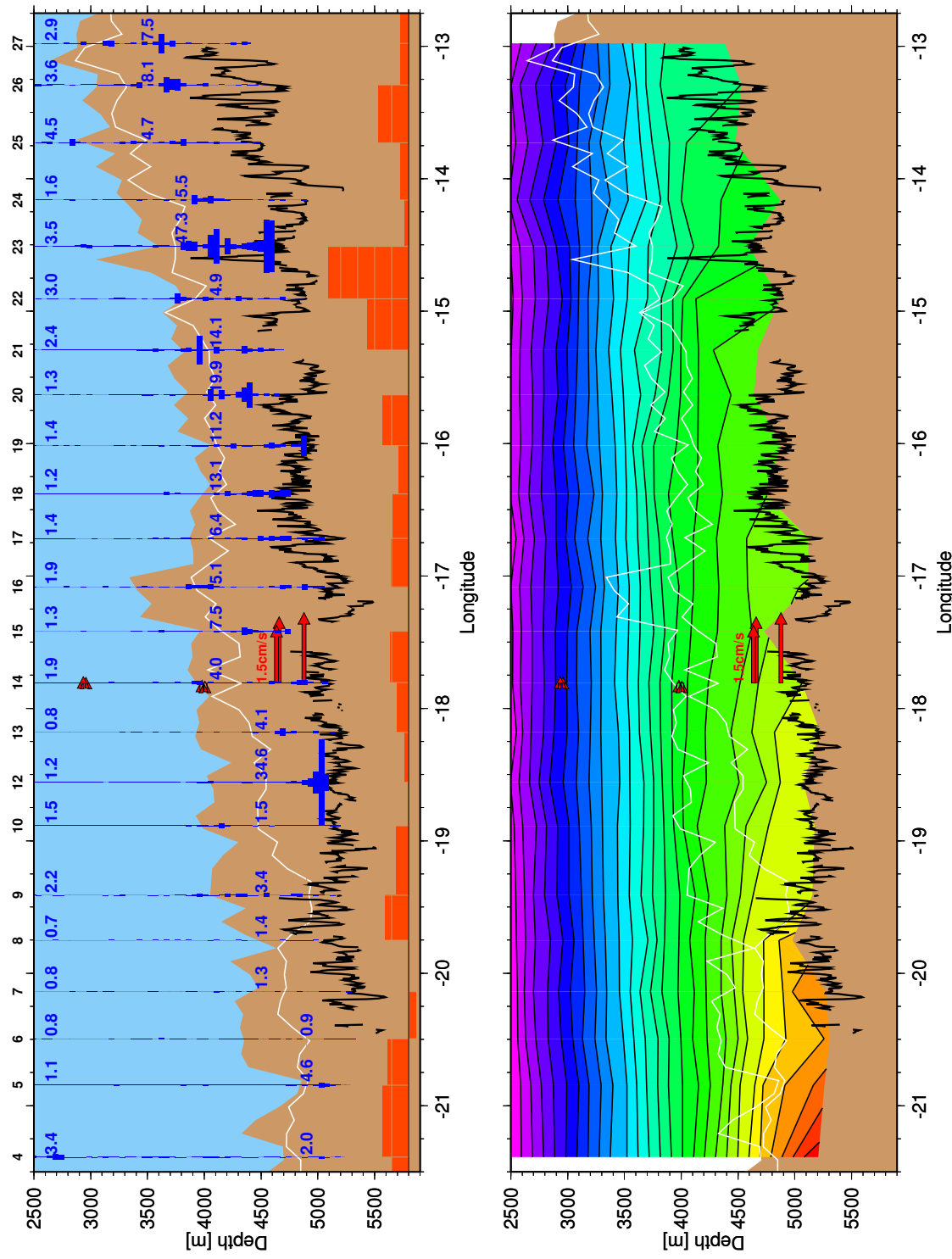
Figure 1.5: Derived from data from Smith and Sandwell [1997] this figure shows the regularity of canyons along the Mid-Ocean Ridge in the Brazil Basin. Individual points are determined by local depth maxima and connected to neighbors to establish canyons. Even after filtering canyons that are shorter than 40km the regularity and abundance is very apparent [Thurnherr and Speer, 2003].

been used as noted above the leftmost profile. All the profiles have been offset to align them to the topography above which they were taken. With this scale it is clear that an exponential dependency on height dominates near the seafloor.

The significance of the canyons mentioned becomes apparent when the prevalence of such features is seen. Thurnherr and Speer [2003] showed graphically that these exist in a very regular manner as can be seen in Figure 1.5, from their study. The South Atlantic is pictured centering around the MOR, which can be seen from lighter grays representing higher topography. Using bathymetry data, an algorithm was developed to identify canyons based around connecting local depth maxima to form valleys with certain characteristics, which included shallow slope and valley lengths of over 40km [Thurnherr and Speer, 2003]. The identified canyons are plotted in blue, which can be seen to occur regularly throughout the region on both sides of the MOR.

One canyon within the Brazil Basin, in Figure 1.5 at about  $22^{\circ}S$ , was the location of study [Thurnherr *et al.*, 2005] that included a two-year current-meter record that exemplifies intense flow within MOR canyons. Figure 1.6 gives a detailed look at the canyon centered around the location of velocity data and including many dissipation profiles both up and down stream. The bathymetry within the canyon is shown in both representations of this section as a black jagged line, with white lines for the canyon walls. Within these walls the observations showed a very significant flow averaging  $1.5\text{cm/s}$  up-canyon, but the measured velocities decreased once above the canyon. The top of Figure 1.6 shows dissipation in blue which are numbered above, in black. The depth-averaged value within the canyon is displayed in blue above the bathymetry line with units of  $10^{-10}\text{W/kg}$ . This is significantly higher than the average value between 2000m and the mean of the two canyon walls, printed in blue at 2700m. The scale of the blue dissipation bars can be compared to the maximum value observed, by station 12, which has a 50dbar segment averaging  $3.2 \times 10^{-8}\text{W/kg}$ . Additionally, this plot also shows the horizontal density gradient observed at the top of the canyon with red blocks having a zero at the 5500m depth line. A full block above this line indicates eastward-decreasing density twice as strong as the

Figure 1.6 (*facing page*): Two plots from observations taken within a Brazil Basin canyon. Both figures have a black line showing the bathymetry within the canyon and have the two year mean of along-canyon velocity displayed at the position it was observed. The canyon walls are shown with white lines, with the top figure shading up to the higher wall. The top figure displays dissipation profiles in blue with depth-averaged value displayed at 2700m (for average found between 2000m and the canyon top) and within the canyon (for average below canyon walls) in units of  $10^{-10}\text{W/kg}$ . The red blocks with a zero at 5800 indicate the strength of the density gradient above the blocking topography with each block being  $10^{-7}\text{kg/m}^3\text{m}^{-1}$ . The bottom figure also displays density, though the contours here were chosen to be evenly spaced at the western boundary. The top figure is from Thurnherr *et al.* [2005] and the bottom, using the same dataset, from a personal communication [Thurnherr 2011].



Region	Area	Mean dissipation ( $10^{-10}Wkg^{-1}$ )	Buoyancy-flux contribution
Above plain	40%	0.9	14%
In canyon	15%	9.3	53%
Above MAR	45%	1.9	33%

Table 1.1: Estimates of buoyancy flux across the interface between the AABW and NADW using the average of observed dissipations below 2km. By splitting into three regions and listing areas of each, the importance of dynamics in such canyons can not be dismissed. These calculations are from [Thurnherr *et al.*, 2005].

estimated temporal variability of  $10^{-7}kg/m^3m^{-1}$ . The second portion of Figure 1.6 shows potential density within this canyon section. Contours were chosen to be spaced uniformly at the western edge of the section. This choice clearly shows how isopycnals within the canyon dip downward to meet the rising slope, and so follow the general trend seen at the sill height indicated by the gradient. The two views of density and a buoyancy frequency on order of  $10^{-3}s^{-1}$ , [Thurnherr *et al.*, 2005], support the previous assertion that the exponential nature of dissipation does pass to diffusivity. Though the dissipation shown in Figure 1.6 is not clear enough to discern this form alone, it does support bottom intensification and so is not considered contradictory.

Density measurements at the top and bottom of the ridges indicate that flows similar to what is seen in Figure 1.6 should exist throughout many other canyons [Thurnherr and Speer, 2003]. Using this assumption the observations from the single Brazil Basin canyon were generalized over the rest of the ocean. In partitioning for this generalization, the abyssal plains were separated from the MOR; these regions are very distinct in terms of diffusion as seen in Figure 1.2. Further, the MOR canyons were isolated as well, which for example, would include only the middle profile from Figure 1.3. The result is three regions which can be compared in terms of the amount of dissipation and upward buoyancy flux from the Antarctic

Bottom Water (AABW) to the North Atlantic Deep Water (NADW) occurring. For emphasis, Table 1.1 lists these two terms as well as relative area the partitions contain[Thurnherr *et al.*, 2005]. This partitioning clearly shows the 15% of the AABW-NADW interface located above MOR-canyons dominate in terms of dissipation and buoyancy-flux. While observed due to even finer scale features, the Lucky Strike rift valley in the North Atlantic has been observed to have even more intense flows than that seen in the Brazil Basin [St. Laurent and Thurnherr, 2007; Thurnherr *et al.*, 2008]. The sills present in such regions present additional complexities, yet most closely fit the canyon partition of Table 1.1. The fact the rift valley showed even greater velocities and flux means these observations are do not contradict the above generalization either.

Focusing on the prevalent canyons along the MOR, with the observational description of Brazil Basin in mind, a numerical study was devised to test the generality. To fully support such a study, Part I will more thoroughly review the literature in Chapter 2 focusing on the Meridional Overturning Circulation, and physics of up-slope low; solidifying the basis for a generalized numerical model. From this point, two models will be developed in their own chapters, 3 and 4, explaining parameterization choices and preliminary testing done to support these choices. Part II presents the main simulations and analysis, making use of two diagnostics formed in development and finally discusses these results.

## Part I

# Theory and Model Formulation



## Chapter 2

# Background and Equations

### 2.1 Meridional Overturning Circulation

With the basic abyssal circulation theory touched upon and some related observations already presented in the way of motivating and describing the focus for this study, it will still be worthwhile to take a step back and review more of the theory and numerical results from the literature. The topics that branched out from basic deep circulation theory can also be approached from the direction of the Meridional Overturning Circulation and relatedly, the thermohaline circulation. The term thermohaline circulation has grown in context and usage, yet Wunsch [2002] presents a clear description while acknowledging the ambiguity that has developed around it. The second in his list of definitions for thermohaline circulation, ‘the abyssal circulation’, fits with the way Ch 1 began its description; however, the list continues, including another six definitions in quick succession. Each definition includes different tracers, fluxes, and/or driving forces and each could be considered appropriate in its own situation. Making use of the third definition, ‘the meridional overturning circulation of mass’ (MOC) is different enough from the introductory explanations to be revealing while still describing the same phenomena.

The choice of focus on mass is useful as this tracer affects all others. Heat and salt are the other tracers most relevant to dynamics which are related to the name ‘thermohaline’ and complete the set primarily considered. Though there are

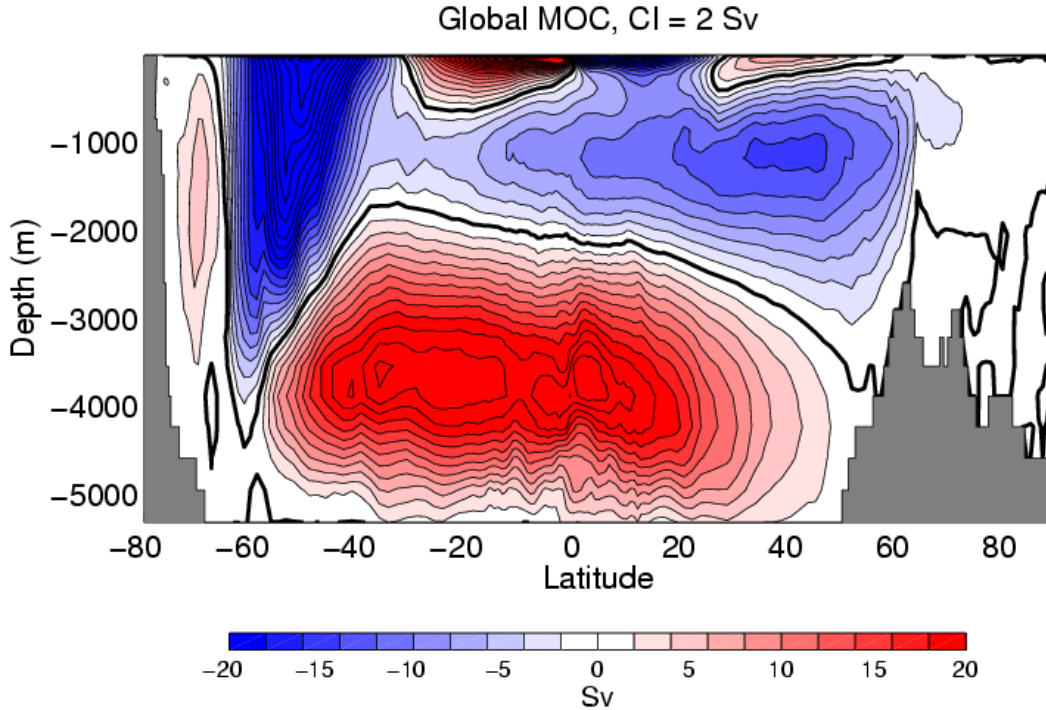


Figure 2.1: A zonally integrated snapshot of flux over a simulated Atlantic Ocean from the Pilot Ocean Model Intercomparison Project [2003].

many possible ocean forcings, like the upper ocean's differential heating and salinity sources/sinks, most of these are thought to have mainly local effects. The two big exceptions, wind and tides, are thought to be the initial source of energy for the majority of the ocean, which has thus been accepted as a mechanically driven system [Wunsch and Ferrari, 2004]. When the entire Atlantic basin is integrated zonally the essence of the MOC appears, a vertical cell where water flows poleward near the surface and then sinks as can be seen in Figure 2.1. The downward leg of the circulation is the same as the formation point included in the Stommel theory [Stommel, 1958]. The deep water spreads southward, and upwelling occurs to complete the circuit.

Thermodynamic models have been used to show that surface gradients of salinity directly correlate with the strength of the MOC [Gade and Gustafsson, 2004]. Other numerical studies were performed, altering these gradients by imposing fresh-water

flux at high-latitudes [Fedorov *et al.*, 2007], which when increased would weaken the thermohaline circulation. In performing these experiments they found that the other factors controlling the strength of the circulation were the spatial distributions of forcing and diffusion. Sensitivity to vertical diffusion has also been shown for the strength of heat and salinity transport at the sea-surface [Cummins and Foreman, 1998]. Convective mixing near the poles, while important for determining deep water properties, does not appear to be an important factor for MOC strength. In fact Marotzke and Scott [1999] explained their numerical result, where decreasing the convective mixing efficiency actually increased the strength of the overturning, stating that convection ‘drains the system of potential energy’.

The upward branch of the meridional cell has been known to be a determining factor in the strength of the overturning [Bryan, 1987]. Although increased upwelling strengthens the cell, numerical simulations having misplaced upwelling can show the opposite trend. A numerical investigation done by Boning *et al.* [1995] showed specifically that a weakened MOC results from excessive mid-latitude upwelling. Within their models, the presence of numerically induced upwelling created a shortcut in the circulation and thus diminished the northward heat transport. With observed interior mixing being much too weak to affect overturning [Ledwell and St. Laurent, 2011] there is much need to improve Stommel’s zeroth order approximation for upwelling and thus diffusivity.

## 2.2 Boundary Mixing and Dynamics

Other indications that upwelling is a key aspect in abyssal dynamics results from investigation into what has simply become known as the Missing Mixing Problem. It has been almost 50 years since Munk’s [1966] estimate of vertical diffusivity as  $10^{-4} m^2/s$ , yet direct measurements both near the surface [Gregg, 1987] and even near much of the seafloor (away from the MOR) [Polzin *et al.*, 1997; Mauritzen *et al.*, 2002] yield values at least an order of magnitude lower, Figure 1.2. Since stirring and advection along potential density surfaces, called isopycnals, do not require

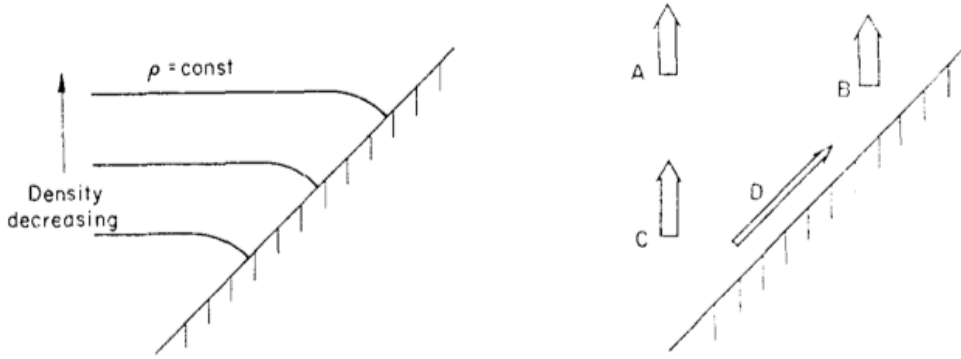


Figure 2.2: Pictured are two methods to visualize the creation of a bulk flow up a sloping boundary induced by diffusion of a stably stratified fluid. On the left the isopycnals are shown curving downward to satisfy a no-flux boundary condition. This creates a situation on the boundary with a horizontal gradient that allows the fluid to move toward and up the slope. On the right, arrows A-C indicate mass fluxes caused by vertical mixing. In order to maintain B another flux at D must be established [Phillips, 1970].

diapycnal mixing to achieve Munk's figure, there is a possibility the influence of local hotspots of mixing are moved this way instead of a more globally-uniform balance [Ramsden, 1995]. Armi [1978] originally proposed the solution of boundary mixing providing the heat flux to balance the interior using the same physics and determined a parameterization for an average diffusivity. The investigation of the turbulent boundary layer with a parameterized effective diffusivity was continued by Ivey [1987] in laboratory experiments. Concern has arisen that boundary mixing may not be effective since it does not produce buoyancy fluxes for net mixing [Garrett *et al.*, 1993]. Further, the parameterization is most effective if the stratification of the turbulent layer is similar to that of the interior which is not what is seen in many density profiles. This difference can be seen in Figure 1.6 as the sloping isopycnals create a weaker stratification near the boundary than further in the interior.

A big insight was provided by Phillips [1970] in his laboratory experiments of stratified fluids over sloping topography, which is a central feature of the MOR

canyons simulated here. Assuming a stably stratified fluid over a solid boundary, it can be assumed that no mass is fluxing through the boundary. Over a flat bottom this is the trivial case of horizontal isopycnals and so the expected stagnant system will slowly mix by molecular diffusion. With the presence of the sloping topography, the isopycnals are forced to bend downward to be perpendicular to the boundary, as seen in Figure 2.2. This creates a small area where there is a lateral gradient in density and adjustment creates a flow toward, and consequently up, the slope. Another method of describing this induced bulk flow is through fluxes if a quasi-steadystate is assumed.

A vertical flux would exist in the interior, as represented by A in the right plot of Figure 2.2B, having been generated from the vertical diffusion of mass. Moving horizontally to the boundary would have a similar flux, shown by B, for the same reason. For these fluxes to be maintained, the mass at levels A-B must be replenished. Point A has can be sustained by a similar flux existing from below it, represented by C. To maintain B, already near the boundary, a flux, indicated by D in the figure 2.2, must exist. If the flux D did not exist the point at B would grow less dense and adjustment processes would create a horizontal flux from A to B which would connect the points C and B as well.

Experiments by Ivey and Corcos [1982] looked at the influence of mixing in a stratified fluid, forced by oscillations at a vertical boundary, which can be considered one of the limiting cases for slope in the Philips description. In Ivey and Corcos' physical models the vertical mass flux was found to be dependent on the turbulence parameters, dependent on the model's oscillating-grid, and the mean density gradient. Laboratory experiments relaxing the vertical boundary mixing into a variable slope were carried out creating a parameterization for the transport [Phillips *et al.*, 1986]. The setup here used an oscillating grid lying on a frame to create a constant slope angle that could be changed between experiments. The viscosity and diffusivity were assumed proportional to the properties of the grid and its oscillations, allowing determination of a formula for boundary-layer thickness,

$$\delta = \frac{4\nu\kappa}{N^2 \sin^2 \alpha}^{1/4}. \quad (2.1)$$

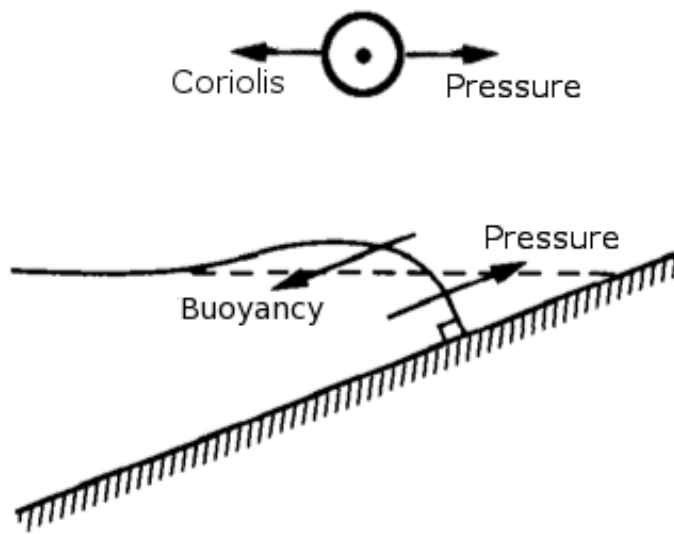


Figure 2.3: Force diagram of stratified fluid over sloping topography. Solid line is the density contour which is horizontal in the interior, a line extended to the boundary with dashes. In curving to meet the boundary it not only creates the pressure forced up-slope flow which was the focus of Phillips but also a countering downward buoyancy forced flow. Also included is the possible geostrophic current that would result in an along-slope component.

Further, buoyancy transport from Ivey and Corcos experiments were found to have the same form even though the domain geometries were different [Phillips *et al.*, 1986].

Additional features of upslope flows are visible in the layer depicted by Figure 2.3. The isopycnal shown demonstrates how such contours tend to overshoot the level where they equal the interior. The overshoot creates a slight bulge adding the possibility for an additional flow. The dotted line in the figure, 2.3, represents the level the isobars would be if allowed to be horizontal, like would occur over flat bathymetry. As already explained, the isopycnals are perpendicular when they intersect the boundary, satisfying a no-flux boundary condition, and so pressure forces an upward flow. In addition to this, the bulge creates opportunity for the development of a counter-flow, back down the slope, forced by buoyancy differences. Additionally, there is also the possibility for geostrophic flows that would develop along the slope, when Coriolis effects are considered. When estimating effects from all three types of flow, Garrett [2001] found the net mixing involved was found to be small.

With it already established that the ocean is a mechanically driven system [Wunsch and Ferrari, 2004], the problem of exactly where the mixing occurs became a focus of many studies [Gregg, 1987; Mauritzen *et al.*, 2002]. Observational studies have shown that the mixing in the interior of the ocean is much to weak [Ledwell and St. Laurent, 2011] which directly implies the boundaries must be important. Following possible pathways originating from wind and tides, the energy for global mixing and has been considered [Dell, 2010]. Such studies leave open the possibility that most of the global mixing may be explained by spatially localized regions of enhanced mixing [Bryden and Nurser, 2004]. Encouraged by this remaining opportunity, equations for investigating one known instance of intensified mixing are formulated.

## 2.3 Equations

In determining how to model an idealized canyon with sloping bottom, the reviewed literature provides the insight needed to both ensure inclusion of the needed parameters as well as reasoning for neglecting others. The needed equations to perform the current study will be considered, justifying the inclusion or exclusion of most terms along the way. While it is necessary to cover physical phenomena (like diffusivity) and domain characteristics that implicitly define the model scenario (like canyon walls) decisions on fundamentals such as needed variables must also be made.

To start, the domain needed for a simulating an abyssal canyon will be considered. Characteristics reported from observation [Thurnherr *et al.*, 2005] will be the basis for idealizing the domain. A canyon running directly east-west is imagined so that the x-axis, being horizontal, is positive eastward, directly along the canyon axis. The z-axis is vertical and the y-axis can complete a right-handed system with positive pointing north across the canyon. Depths in the domain will be negative, indicating the distance down into the canyon: a choice that implicitly places the domain between two solid boundaries, in the y-directions. Depending on the influence and existence of cross-canyon flows, justification can be made for simplifying the model to two dimensions. The Rossby radius of deformation,  $L_R$  would normally be called to justify such assumptions, but in this case is the same order as the observations for canyon width. Evaluating  $L_R = NH/f_c$  with Coriolis forcing of order  $f_c = 10^{-5}s^{-1}$ , abyssal buoyancy frequency observed being  $N \leq 10^{-3}s^{-1}$ , and estimating a scale height from Figure 1.2 of  $H \approx 500m$ , gives  $L_R$  of less than 50km compared to 20-40km canyons. This is large enough that Garrett *et al.*'s [1993] primary cross-canyon flow could begin to form. Still, wanting the reduction to two-dimensions since it simplifies the problem and increases the tractability of computations, the implication of results is relaxed. Instead of results being general over the width of the canyon, it is maintained that an upslope flow must form which can be represented in two dimensions. So with this model simplification, results will be applicable to within these flows.

Diffusion was already determined as a primary component for forcing the over-

turning and must be included. Besides viscous diffusion, two dynamically active tracers rely on their own diffusion, temperature and salinity. For the purpose of simplification they can be thought of similarly and reduced to a single effect, even though each would have their own rates of diffusion and own terms coupling to the dynamics. While feasible to adjust the terms mentioned to create a cumulative tracer, the naive approach was taken and salinity made inactive and neglected aside from a constant contribution through the equation of state.

The equation of state brings pressure and then density into consideration, before invoking Navier-Stokes or the primitive equations. Looking over the entire  $100\text{km}$  domain, a Rossby number of just under unity is calculated given velocity magnitudes of  $2 - 3\text{cm/s}$  [Mauritzen *et al.*, 2002]. Given these realistic values, the question of geostrophy would be unanswered even in a three dimensional situation with Coriolis included. The appropriateness of hydrostatic balance is also questionable, even in the closed domain case. Because diffusion will be explicitly specified, the creation of buoyancy is possible which could disrupt such a balance. Restriction to sufficiently smooth diffusivity profiles, however, should be able to regain this balance. Density can be given with an equation of state in terms of temperature and pressure only, since salinity is constant. Further, density is only important in terms of deviation from its mean in the term with gravity, so Boussinesq approximations apply.

Combining all the simplifications and assumptions mentioned the governing equations are

$$\frac{Du}{Dt} + \frac{1}{\rho_c} \frac{\delta p'}{\delta x} = \nu_x \frac{\delta^2 u}{\delta x^2} \quad (2.2a)$$

$$\frac{Dw}{Dt} + \frac{g\rho'}{\rho_c} + \frac{1}{\rho_c} \frac{\delta p'}{\delta z} = \nu_z \frac{\delta^2 w}{\delta z^2} \quad (2.2b)$$

$$\frac{\delta u}{\delta x} + \frac{\delta w}{\delta z} = 0 \quad (2.2c)$$

$$\frac{D\theta}{Dt} = \kappa_x \nabla^2 \theta + \frac{\delta}{\delta z} (\kappa_z \frac{\delta \theta}{\delta z}) \quad (2.2d)$$

$$\rho' = \rho(\theta, p_o(z)) - \rho_c.. \quad (2.2e)$$

Standard variable choices are used;  $u$  and  $w$  are the velocities in the horizontal and vertical direction. The total derivative is defined as  $\frac{D\cdot}{Dt} = \frac{\delta\cdot}{\delta t} + u \frac{\delta\cdot}{\delta x} + w \frac{\delta\cdot}{\delta z}$ .

The variables potential temperature, pressure and density are  $\theta$ ,  $p$  and  $\rho$ , while thermal diffusivity and viscosity are  $\kappa$  and  $\nu$  respectively. The subscripts indicate components in the given direction, primes indicate perturbation from a mean and the subscript c indicates a reference constant. While still being of a rather general form these equations exclude many components extraneous to the study at hand, so they are a good starting point to configuring specific models as will be done next.

## Chapter 3

# Finite Differences: The MITgcm

When first considering how to model the MOR canyons, like that of Figure 1.6 on page 10, an established model was chosen as the best place to start. The option of testing in a nonhydrostatic case was desirable, as well as the possibility to go from two to three dimensions. Most importantly the ability to specify spatially-varying vertical diffusivity was required. The MITgcm [Marshall *et al.*, 1997] contained all these options so was an ideal starting point. The model is an ongoing project so the checkpoint used for final runs in this thesis, checkpoint 63a, is likely no longer the most current

### 3.1 Equations and Parameterization

The MITgcm is a z-coordinate finite volume model that was developed and has core support based at Massachusetts Institute of Technology [Marshall *et al.*, 1997]. While this model supports much more than just an ocean, this is the only piece used

in this thesis. The ocean portion is based on the Primitive Ocean Equations;

$$\frac{D\vec{v}_h}{Dt} + f\hat{\mathbf{k}} \times \tilde{\mathbf{v}}_h + \frac{1}{\rho_c} \nabla_z p' = \nu_h \nabla^2 \vec{v}_h \quad (3.1a)$$

$$\epsilon_{nh} \frac{Dw}{Dt} + \frac{gp'}{\rho_c} + \frac{1}{\rho_c} \frac{\delta p'}{\delta z} = \epsilon_{nh} \nu_v \frac{\delta^2 w}{\delta z^2} \quad (3.1b)$$

$$\nabla_h \cdot \vec{v}_h + \frac{\delta w}{\delta z} = 0 \quad (3.1c)$$

$$\frac{D\theta}{Dt} = Q_\theta \quad (3.1d)$$

$$\frac{DS}{Dt} = Q_S \quad (3.1e)$$

$$\rho' = \rho(\theta, S, p_o(z)) - \rho_c. \quad (3.1f)$$

Having decided that the physical scenario is adequately governed by the equations from the previous chapter, Equations 2.2, it can be seen that the MITgcm is more than adequate to satisfy these needs. The similarities and differences in these two set of equations will be used to guide the discussion on the fundamentals of setting up the MITgcm. The first two equations here, (3.1a)-(3.1b), are the horizontal and vertical momentum equations, respectively, where  $\vec{v}_h$  and  $w$  are the horizontal and vertical velocities. The MITgcm allows full three dimension but the horizontal velocity, and all other horizontal terms,  $\cdot_h$ , reduce easily to one horizontal direction. The Coriolis parameter is denoted  $f$ , which will be ignored due to looking at the mean of the upcanyon flow, as is explained in Section 2.3. A nonhydrostatic weighting coefficient,  $\epsilon_{nh}$  is present and used to test if hydrostatic balance is a reasonable assumption. The fourth equation, (3.1d), governs potential temperature and is written in terms of a general forcing,  $Q_\theta$ , which will include the diffusive terms driving all the simulations in the study. The form taken by the expansion of temperature forcing, which will match (2.2d), allows separate specifications of vertical and horizontal diffusivity. More importantly the vertical diffusivity is not required to be constant but will contain a spatial dependence necessary for bottom intensification of mixing. The MITgcm equation for salinity (3.1e), is directly analogous to the previous tracer even in expansion of its its generalized forcing,  $Q_S$ . To simplify the study the salinity is made inactive by two specifications. The forcing term for salinity is set to zero and the entire model is initialized to a constant salinity of

35ppt. These actions allow assurance that salinity is inactive while avoiding the complications involved in removing it. As an example, the constant value of salinity makes the contribution to the equation of state trivial. Thus the final equation, (3.1f) is equivalent to the expected form matching (2.2e).

Basing parameters on realistic values was a priority when the decisions about this study's base case were made. The domain size was no exception and was chosen to be quantitatively similar to the canyon described before (Figure 1.6), so the observed phenomena will be most easily associated to phenomena appearing in the numerical results. The primary feature for the domain is that of the slope angle. An initial value of 0.005 was decided on as it is the same order as is representative of the MOR slope, [Thurnherr and Speer, 2003], and also leaves room for realistic values that are both steeper and shallower. Depths of 500-1000m are reported for these canyons [Thurnherr *et al.*, 2005], inspiring the choice for a 1km domain height. The domain length was chosen to allow realization of the mentioned slopes while having the bathymetry rise less than the 1km domain height; 100km is adequate and allows room for a portion to be flat at maximum depth. Specifically, these choices leave room for a 20km plain to be included before sloping bathymetry rises 400 meters over 80km. Keeping the aspect ratio for grid spacing equivalent to the domain, 100 nodes in each direction was assumed sufficient resolution for the expected phenomena. To be explicit, the resulting uniform z-grid from these numbers is 100 vertical levels spaced 10m apart as well as 100 grid points in the horizontal with 1km in between. The depth is specified for each of the x-locations, sloping up to the western boundary and explicitly enforcing a closed domain by having the first and last point specified as 0 depth.

Differential equations specified on a domain need initial conditions and boundary conditions before it is possible for them to be well-posed. A closed domain was used for simplicity, which implicitly specifies some boundary conditions and reduces the choices for the others. Closed boundary conditions on velocity are primarily limited to free-slip or no-slip. No-slip conditions are thought to be the more realistic of the two and therefore primarily used. The initial condition for velocity will

simply be the stationary state, identically zero everywhere. Salinity, though inactive will be set to a uniform background of 35ppt as mentioned before. While for our tracer temperature, the no-flux condition used in the description of upslope flow is necessary and, with initial condition, sufficient. The needed initial condition determines the buoyancy gradient which will be feeding the system and resulting dynamics. The potential temperature field will be centered around a mean of 3 or 4°C and couples to the velocity equations through a linear equation of state using a thermal expansion coefficient of  $2 \cdot 10^{-4} K^{-1}$ . This leaves the buoyancy frequency as the defining parameter, which will start as a constant,  $N=10^{-3} s^{-1}$ , representative of the Brazil Basin canyon 1.6.

The remaining terms to be examined from the governing equations, Equations 3.1, are the coefficients on forcing terms. The nonhydrostatic coefficient,  $\epsilon_{nh}$ , determines the use of hydrostatic balance, which will be qualitatively tested, and set to zero afterwards if nonhydrostatic contributions are unneeded. The other coefficients are the viscous and thermal diffusion,  $\nu$ . and  $\kappa$ . respectively allowing for different values in the vertical,  $\cdot_v$ , and horizontal,  $\cdot_h$ , directions. Kinematic viscosity will be relatively straightforward having constant values in each of the vertical and horizontal directions, and the horizontal component of diffusivity will similarly be a constant. The vertical component of turbulent diffusivity, considered a main focus of the study, will have spatial dependency. This parameter will exponentially decay from the topography, a form supported by observations such as the profiles in Figure 1.4 among others [Ledwell *et al.*, 2000]. Though explicitly dependent only on the height above the bottom, the sloping topography creates an implicit horizontal dependence and gradient for this component of diffusivity. Specification of the exponential profiles rely on two parameters, a maximum value,  $\kappa_{max}$  and a decay length or e-folding depth. The first simulations will use the large value of  $0.1 m^2/s$  to ensure results, and a scale of 500m.

### 3.1.1 Discretization and Algorithms

Besides physical parameters there are several numerical settings that must be described and considered. Some of these were decided implicitly when the MITgcm was chosen. This model is a z-grid finite volume model; these characteristics largely determine the spatial discretization as well as determine viable algorithms. Especially with the case of spatial discretization, effects of some of these choices have already been approached indirectly. Considerations such as choice of algorithms will be new topics altogether.

The spatial discretization is what was being specified when choosing number of nodes and layers for the domain. The z-grid associates a vertical coordinate with physical depth as opposed to other choices such as  $\sigma$ -coordinates that create terrain-following levels. Both the z-coordinates and the x-coordinates were chosen to be uniformly spaced, but the MITgcm does not treat all variables as located directly on the grid points. The model incorporates finite volume techniques, very similar to finite difference with flux forms of the equations, and an Arakawa C gridding. The Arakawa C grid, Figure 3.1a, is a method of staggering the location at which the variables are represented; combined with considering small volumes around the points, this helps satisfy non-divergence criteria. As the image shows, velocities are calculated in between grid points and are represented more similarly to a flux through boundaries of rectangular cells created by four neighboring points, indicated by arrows on Figure 3.1a. With these placements velocities are associated specifically with the west and bottom of the cells, which although seems to omit the east and top, has those specified in terms of the neighboring cells.

With the model inclusion of staggered variables, there are consequences on how the topography is realized, in addition to those from representing a boundary with a z-grid. Partially filled cells are aptly named to mean the finite volume methods are not always acting on the same amount of fluid, nor are the fluxes calculated using equal areas. The MITgcm tracks two cell thickness percentages to augment the standard cell size. Figure 3.1b demonstrates a cell of full height, labeled  $\Delta z$ , as well as the heights for cells with only portion falling within the interior of the domain,

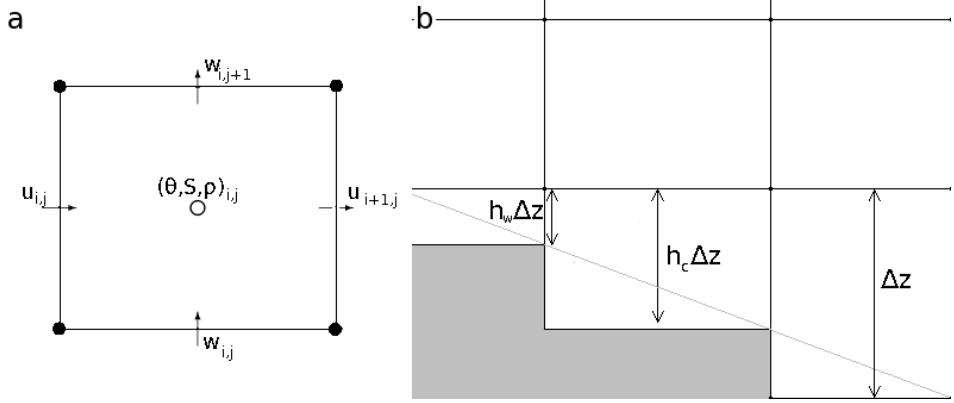


Figure 3.1: Diagrams of the discretization methods. a) Shows the Arakawa C-grid which staggers the placement of velocities and other tracers. The horizontal velocities are located in the east/west cell faces, the vertical velocities in the top/bottom faces, and other tracers in the center of each cell formed by specified nodes. b) Shows a method of allowing the boundary to intersect the grid. The height is specified at the cell boundaries and the center, here  $h_w$  and  $h_c$  indicate the fraction of the west cell face and the center in the fluid interior, which augments the finite volume being considered at these places.

as measured at the center and western edge. The western cell height,  $h_w \Delta z$ , aligns with the Arakawa C-grid location for the horizontal velocity and will affect that flux accordingly. Like was mentioned in the description of the gridding, the east boundary is not specified to avoid redundancy since that same location is the west for a neighboring cell. The central cell height,  $h_c \Delta z$  weights the volume containing the other tracers, including potential temperature and density.

Time can be discretized by setting a step size, but how the previous time steps are combined and even how the current state interacts with itself has a variety of choices. This leads into the advection schemes that calculate a flux for each tracer at each point in time. To start the advection operator is discretized by integrating over small volumes, and resulting in the model calculating fluxes to update the variables. The algorithms used are upwind-biased third-order direct space time (DST) methods [MIT, 2011], which incorporate the time and spatial discretizations

in one step. Within the MITgcm, the DST-method determining the flux,  $F$ , of an arbitrary tracer at position  $i$ ,  $\tau_i$  is given by the equations

$$F_i = u(\tau_{i-1} + a_0(\tau_i - \tau_{i-1}) + a_1(\tau_{i-1} - \tau_{i-2})) \quad \forall u > 0 \quad (3.2a)$$

$$F_i = u(\tau_i - a_0(\tau_i - \tau_{i-1}) - a_1(\tau_{i+1} - \tau_i)) \quad \forall u < 0. \quad (3.2b)$$

where the coefficients  $a_0$  and  $a_1$  are

$$\begin{aligned} a_0 &= \frac{1}{6}(2 - |\nu_c|)(1 - |\nu_c|) \\ a_1 &= \frac{1}{6}(1 - \nu_c^2). \end{aligned}$$

The bias of this scheme becomes apparent by noting that positive and negative velocities are treated differently in 3.2. The fact the scheme is upwinding can be seen by inspecting the term weighted by  $a_1$ . When the velocity is positive this term depends on  $i - 1$  and  $i - 2$  and when negative at  $i + 1$  and  $i$ , in both cases this is in the direction the flow is coming from, thus upwind. The coefficients themselves include dependence on the Courant number,  $\nu_c$ , a nondimensional constant determined largely by the discretization of the model. This number is related to a necessary but not sufficient condition for stability, the Courant-Friedrichs-Levy (CFL) condition given by

$$\nu_c = \frac{u\Delta t}{\Delta x} \leq C.$$

The value of the limiting bound,  $C$ , depends on the numerical scheme being used and for (3.2)  $C = 1$ . The CFL inequality is requiring that the domain of dependence for the differential equation be located in, or equal to, the domain for the numerical method. If this was not the case, information about the state of the variable would be coming from outside the area considered by the numerical method. The condition does not provide sufficiency for stability and so the use of small timesteps, of 20 seconds, provides a wide safety margin of  $\nu_c = 0.02$  even at velocities of up to 1m/s.

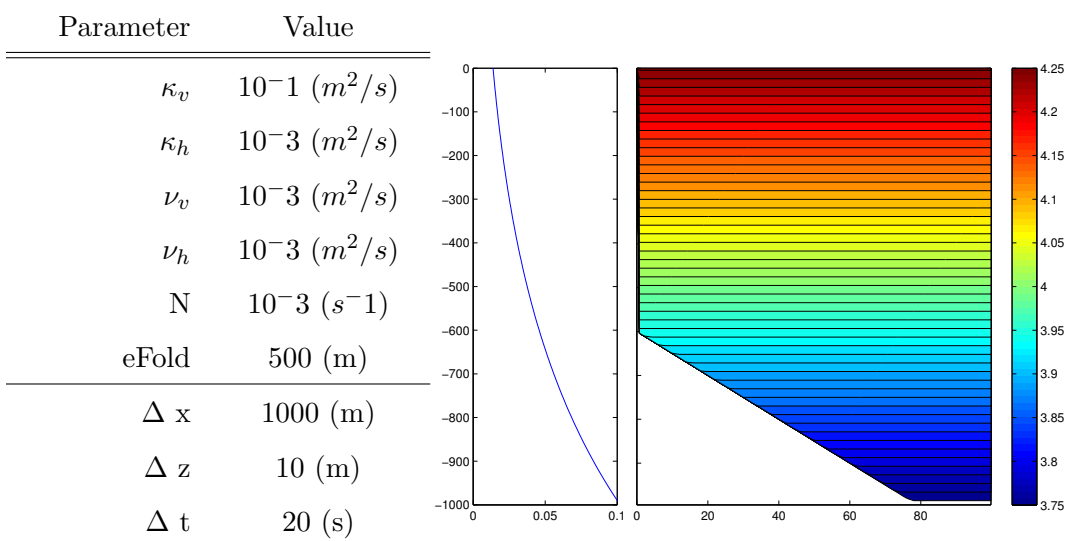


Table 3.1: A summary of the base case simulation parameters. The left includes the values specified in the setup of the MITgcm simulation. The right contains two plots, an image of the potential-temperature used in initialization and the full profile for diffusivity.

## 3.2 Diagnostics and the Base Case

Having described the main parameters, the next step is to go through simulations of a more simplified subset working up to a base case scenario. Cases with either no slope or no diffusion were each run and the expected stagnant result occurred. The initial case as described previously, has its parameters listed in Table 3.1. To the right of the table is a plot of the initial temperature for the domain, and a profile of  $\kappa_v$  from a column over the plain which reaches maximum depth. The displayed case uses no-slip boundary conditions on the bottom and walls, a free-surface, and includes non-hydrostatic terms.

After one day of simulation, dynamics are already developing. Figure 3.2 shows the model output for this timestep with horizontal velocity on the left, and vertical velocity in the center. The potential temperature, on the right, has contours every  $0.02^\circ$  that bend down to intersect the sloping topography. For data like velocity,

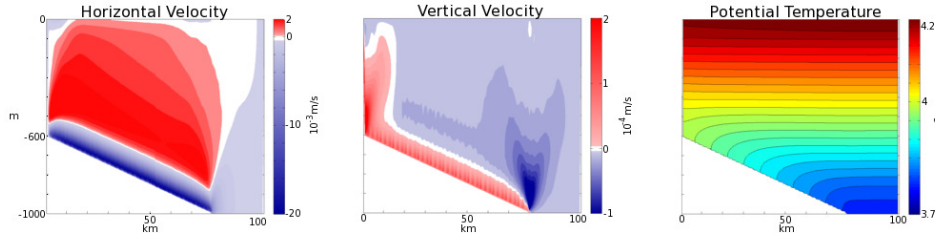


Figure 3.2: The MITgcm output after one day of simulation initialized with the base case parameters. The left shows the horizontal velocities, while the middle shows the same for the vertical. In combination it is clear that an upslope layer has already formed. The right shows potential temperature, with the contours drawn every  $0.02^\circ$  clearly dipping to meet the boundary.

with a range including zero, a primarily two-color scheme is adopted. There is a band about zero in white, blue will always be negative and red always positive. The upslope flow central to this study can already be seen, having horizontal velocities on the order of 1cm/s while the vertical is two orders weaker. Though detectable, determining characteristics of the region flowing upslope using side-by-side plots of horizontal and vertical velocities is cumbersome. Instead of visually aligning the blue area of the horizontal velocity figure with the red portion of the vertical velocity a numerical process is considered. Since specifically calculating the height of the boundary layer could be done but would not be overly informative, this idea is generalized.

To include the wanted information about the bottommost layer while also making other characteristics more accessible, the streamfunction,  $\psi$ , is considered. While the form of streamfunction is standard there is some ambiguity in its sign. Here, the vertical velocity term will be the negative one, namely

$$u = \frac{\delta\psi}{\delta z} \quad \text{and} \quad w = -\frac{\delta\psi}{\delta x}. \quad (3.3)$$

Being a mainly straightforward process, Matlab was used to calculate  $\psi$  using an algorithm based on the inverse of a gradient operator. The gradient operator was constructed using first order finite differences. Central differences are used wherever possible, resorting to right or left differences near boundaries. The operator can then

be used in calculations of the streamfunction. The benefits of streamfunction include allowing a single field to be considered instead of the two components of velocity. The domain-wide minimum of streamfunction,  $\psi_{min}$ , represents of integration of velocity over the column-segment accumulating the most westward flux. Knowing that the bottom boundary layer contains the strongest negative velocities, it can be assumed  $\psi_{min}$  is located in the upslope layer and not in a separate cell elsewhere. Mainly due to indicating this characteristic,  $\psi_{min}$  was adopted as a diagnostic for further analysis.

A diagnostic for approximating the height, or thickness, of the upslope layer can also be found from the streamfunction. The location of the minimum of  $\psi$  for a given column specifies where the upslope portion of flow stops. This is easier to find than estimating the deepest point where the vectorized velocity is no longer approximately upslope. However, the extrema of  $\psi$  for a single column is very susceptible to noise, especially in the presence of perturbations that will appear. To make a diagnostic for average layer height that is more robust, information from more columns is included. Figure 3.3 shows an example from 20 days of simulating the initial parameters. Column-minima of streamfunction plotted on top in green circles. The columns included are restricted to the area over the sloping boundary and at least 10 grid points from the boundary. Calculating the distance above the topography at which each of these minima occur results in column-wise approximations for the thickness of the upslope layer. The average of these is defined as the second diagnostic,  $\delta$  or layer height, which is 218m for the example given.

Having multiple diagnostics defined, standardizing a spinup time is considered next. The calculated field of streamfunction is used in combination with the velocities in determining an adequate spinup time. Figure 3.4 shows the initial case simulation from several different timesteps; each row is labeled with the simulation time that has elapsed, written in days. The top is a plot of the three variables versus time; domain-wide extrema of horizontal (minima) and vertical (maxima) velocity are plotted in blue and red respectively. To allow use of the same scale, the magnitudes of the streamfunction minima has been adjusted by a factor of 1/100,

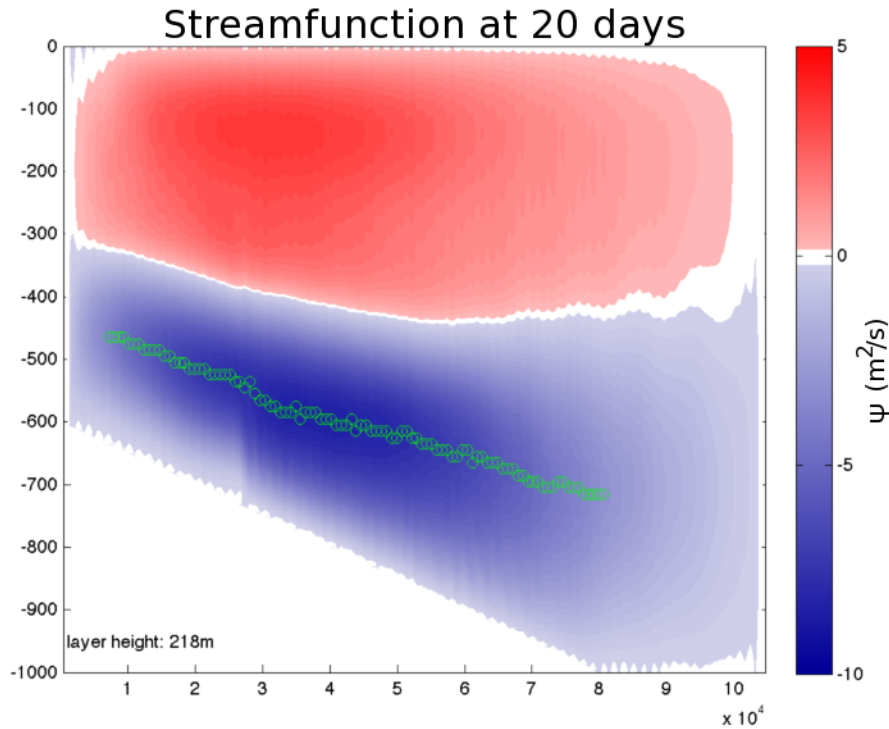


Figure 3.3: Streamfunction of initial parameters at 20 days. The green circles show where the streamfunction is at its minimum for each column above sloping topography excluding a buffer region near the boundary. The layer height for each column is the distance of this location above topography, and the average of all columns' heights is defined as the diagnostic  $\delta$ , written within the sloping region.

plotted in green. The first row shows the domain as the cells are just developing having had only one day of simulation pass. The most extreme values from the 100 day timeseries occur very early on, at about 7 days, and the model variables are shown at this time in the second row. The third time shown is at 20 days which is about when the values settle down judging from the timeseries at the top. This time compared to the 50 day state, bottom row, show that the cells have already fully formed and, for the most part, that only the magnitudes are decaying hereafter.

The difference between times plotted in Figure 3.4 show several other notable phenomena occurring. Looking at the times of 7 and 20 days in particular show

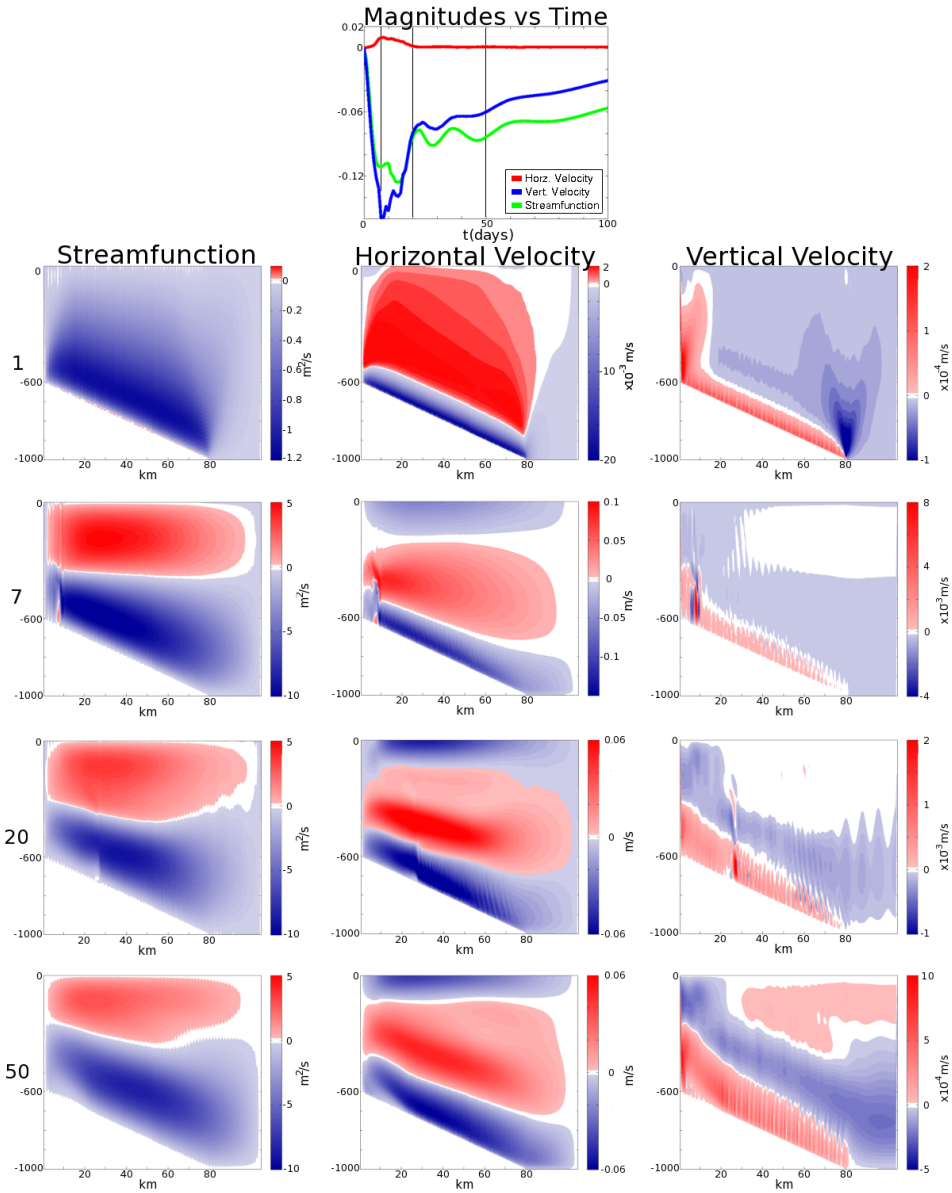


Figure 3.4: Plots showing the development of the upslope layer over time for the base case. The top plot shows  $\psi_{min}/100$  and the extrema of velocities versus time. The left column shows streamfunction, the middle horizontal velocity and the right vertical velocity at times of 1, 7, 20, and 50 days. This reveals a bottom layer forms and quickly reaches maximum strength, after which it slowly weakens.

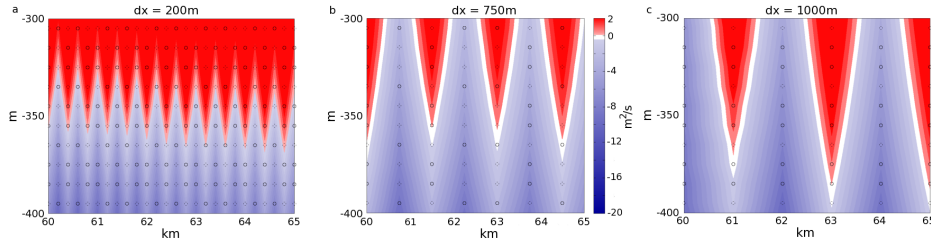


Figure 3.5: Shows the interface between cells at three horizontal resolutions. These three plots are all from the 20day timestep of runs with a 400m and  $\kappa_{max} = 0.3\text{m}^2/\text{s}$ . Grid spacing is shown with black circles for horizontal spacings of 200, 750, and 1000m from left to right. This demonstrates the direct dependence on the grid, for this numerical phenomena.

a wave reflecting off the top boundary and propagating down the slope. Since the boundaries are imposed on the model, reflections caused by them are not realistic and so should be suppressed if possible. The spinup time should allow most of these transient effect to disperse so as not to influence the lasting state. Using the high velocity of 10cm/s, twenty days allows a parcel to travel about 170km which is over twice the sloping region (80km). With this in mind, twenty days was chosen as the spinup period being the shortest period that can confidently be thought of as fully developed. Besides increasing the tractability by keeping computational expense of simulations down, a shorter spinup time helps prevent the investigated dynamics from decaying. Due to the model’s finite and closed domain, any dynamics will decay to the stagnant fully mixed steady-state. The progress of this decay can already be seen when comparing 20 to 50 days. The cells appear fully formed in the earlier of these snapshots; so the effects of the reflection are seemingly negligible, and the main difference is simply the strength of the cells, which are all decreasing over time.

A more imposing numerical effect is a wave, seen most clearly in the vertical velocity, Figure 3.4. ‘Wave’ here is referring to the horizontal oscillation in the vertical velocity field, which is seen in the jaggedness of the contour between white and blue at 7 days and also in the vertical stripes seen in magnitude within the regions

of positive velocities. To force this wave to be clearly visible in streamfunction, the maximum diffusivity was increased to  $0.3m^2/s$  while the other parameters remained at their initial values, since the wave becomes more prominent as vertical diffusivity is increased. By repeating the same high diffusivity simulation with different horizontal discretizations, the grid-scale can be seen to directly influence these waves. Figure. 3.5 shows a closer shot of this wave with horizontal grid having spacing of 1000m, 750m and 200m. The subregion was chosen from the center of the domain to contain the interface between the two cells, as can be seen from the color change. Even at the most refined case,  $dx = 200m$ , the wave still shows an amplitude extending several grid levels. Though the interface seems to move, the calculated diagnostic,  $\delta$ , does not show much change between the refinements, 295, 290.2 and 290.4m for the 1000, 750 and 200m cases respectively. Given these findings, the middle ground will be taken using the first refinement of 750m horizontal spacing, which again saves on computational expense compared to the large refinement yet appears to obtain most of the change in terms of the diagnostic  $\delta$ .

From these few preliminary simulations, it is assumed that the source of the phenomena are spurious jets caused by the fluid moving toward the boundary being forced upward. The step representation of topography redirects the momentum upward, and although the partial steps reduce the effect from what full steps would produce, it is still present. This wave and theory helps motivate choices in our second model to ensure the wave's absence; the ability to resolve terrain was prioritized, which can be done easily with nonuniform meshes used by finite element methods.

### 3.3 Other Checks

Besides what are assumed to be the primary parameters controlling these simulations, there are many other choices made in setup ranging from boundary conditions, to implicit effects of topography specification, to temperature profile. These all were all looked at in varying degrees of detail, many of which are presented here. Figure 3.6 contains an array of plots displaying many of these changes side by side.

The issue with possibly the greatest influence on the study is the one originating as a side-effect of the method of altering the topography slope. In keeping the same x-intercept and changing the rise (and slope) through variation of the z-intercept, the length of slope remains approximately the same. Though this methodology choice is believed to be sound, since the effects seen from changing parameters are not dependent on the slope length, the dependence on slope length must still be investigated.

The base slope of 0.005 is a 400m rise over the leftmost 80km of the domain, displayed in Figure 3.6a. This intentionally flat 20km region allows testing different lengths for the span of sloping topography without altering the domain size completely. The second and third plot, Figure 3.6b and c, present the streamfunction from two such alterations of the base case. Plot 3.6b is extends the sloping region to cover the entire 100km domain, and so rises an extra 100m on the left boundary. The case of Figure 3.6c shortens the sloping region by 20km and correspondingly loses 100m of rise on the boundary. The two diagnostics both show dependence on these changed parameters. Lengthening the slope strengthens the minimum of the streamfunction, from  $-8.37$  to  $-11.30 m^2/s$  while decreasing the slope by the same amount weakens it, to  $-6.92 m^2/s$ . Proportionally, this increases and decreases the slope length by approximately 25%, which creates significant changes of 35% and -17% to the streamfunction minima. The effect of  $\psi_{min}$  in increasing the slope length is roughly twice that of decreasing, in this instance, yet the layer thickness suggests a different relation. The layer height changes very little in response to these variations, 217, 218, and 209m for 100, 80 and 60km slope lengths. While caution must be taken when considering values so close together, as the grid spacing in the vertical is 10m, the result further supports the independence of the two diagnostics. To remain conservative with preliminary simulations  $\delta$  will not be analyzed here. The simulation comparison, Figure 3.6a-c, shows  $\psi_{min}$  has definite dependence on the length of area covered by the sloping topography and must be looked at more comprehensively, later.

Another choice that needs some investigation is that of the vertical decay of

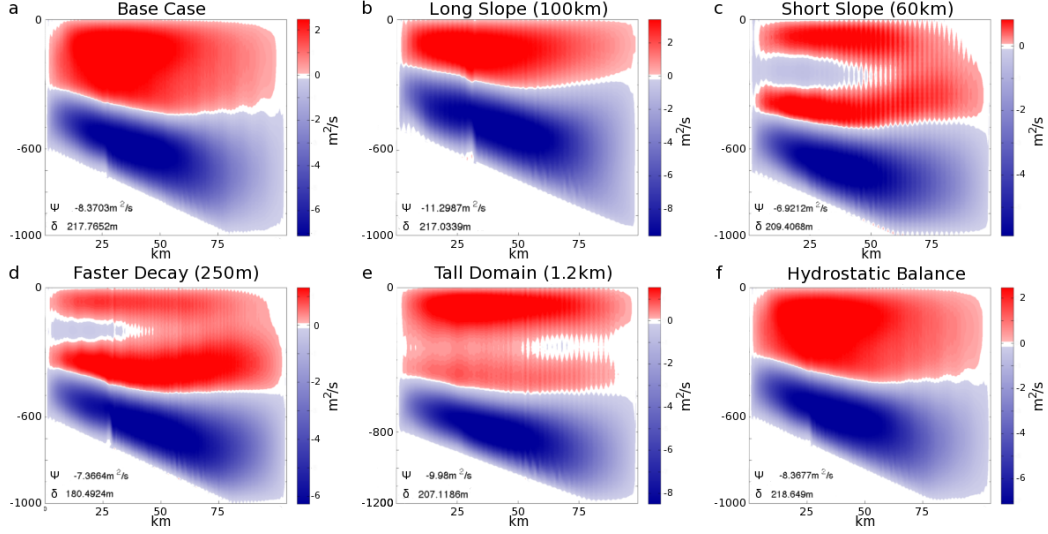


Figure 3.6: Shows an array of streamfunction plots testing the labeled parameters. All plots shown are at 20days and vary from the base case only in the way described; a) Base case has no changes, b and c) the 400m rise is translated up(down) to increase(decrease) the length of the sloping region, d) the decay scale of  $\kappa_{max}$  is halved, e) the domain is extended upward, and f) hydrostatic balance is assumed. All the variations shown have visible effects, besides that of hydrostatic balance.

diffusivity. The shape of exponential decay was justified by observation, 1.3. While the original decay scale was roughly based off the height of enhanced mixing as well, the choice of 500m was less firmly founded than other parameters and may be too large. The domain height being 1km only allows 2 e-folding lengths. This means diffusivity does not decrease even a full order of magnitude, although close to it, within that space. The diffusivity at the top of the domain, over the sloping topography, is even greater as there is less space to decay. With this in mind tests were done halving the decay scale to allow for a 98% decrease given the whole domain height, and still a full order of magnitude decrease over the shallowest part of the base case. The effect of this change is seen in Figure 3.6d in comparison to the base 3.6a. The reported strength of the streamfunction between these drops  $\psi_{min}$  from  $-8.37$  to  $-7.37 m^2/s$  (a 12% decrease) but the layer height drops more dramatically, 217m to 180m (17% decrease), indicative of the velocities actually

increasing when the decay rate increases in this range. With the other characteristics of the streamfunction solution remaining similar, the faster decay scale of 250m is adopted, replacing the larger initial length of 500.

The domain height was also increased to see the effect. Figure 3.6e shows the same parameterization as the base case with the, now old, decay scale of 500m and the domain extended upward a further 200m. The main difference noted is the formation of upper cells which appear to be splitting but not significantly different than in the previous cases of faster decay or shortened slope. Though the strength of  $\psi$  does increase, it is thought more significant in this case that the layer height does not. In fact the layer height is slightly shallower and so for the cases here the original 1km domain is kept.

The final plot of this figure, 3.6f shows a simulation where nonhydrostatic terms are neglected. This binary decision has very little effect on the simulation results even after allowing for differences to accumulate over the standard 20 days. Both diagnostics are very similar between the two simulations, and neither show a change of even half a percent. These results support the simplification to a system in hydrostatic balance, which will have the benefit of eliminating two terms in the model equations since it is setting  $\epsilon_{nh} = 0$  in (3.1b).

Through brief investigations, several of the model's parameters are specified to simplify the system, yet the reduced version is still complex. Though there is a dependence on domain height, the original domain will be kept constant with knowledge of this dependence noted. Similarly the dependence on slope length will be respected by maintaining the length of the sloping region throughout the experiments. The look at decay scale resulted in a change to the initial case to a state that is less diffusive overall. The base case, used in final simulations, makes use of the smaller e-folding length of 250m. Finally the look at hydrostatic balance supports the approximation in these scenarios.

Having looked first at what might be considered secondary parameters, the importance of the viscous and diffusive coefficients have yet to be established. Vertical diffusion being the exception, already known to be a central aspect to the simula-

tions, the other three are tested. A look at the dependencies included simulations each varying one of these parameters both up two orders of magnitude and down. The established spinup time was used and the resulting streamfunctions are shown in Figure 3.7

The array of plots shows the different choices of vertical viscosity and horizontal viscosity. The array omits the test cases for horizontal diffusivity since they were almost identical to horizontal viscosity, and in which  $\psi$  shows little sensitivity. Using this similarity, both horizontal coefficients are represented by  $\nu_h$ : having very large magnitude,  $0.1\text{m}^2/\text{s}$  in the first row, and small,  $10^{-5}\text{m}^2/\text{s}$  in the second. The three columns allow a side-by-side look at not only the stream function but also horizontal and vertical velocities. While the scales for the  $\psi$ -plots are dependent on case, the scales for each of horizontal and vertical velocity are uniform and so not shown; the horizontal velocities range from  $-10\text{cm/s}$  to  $5\text{cm/s}$  and the vertical color extremes are  $\pm 10^{-3}$ . Between the three variables, the differences with respect to  $\nu_h$  can be most noticeable in the vertical velocity field. The low viscosity case allows slightly more horizontal advection of momentum, spreading the velocity and connecting the contours slightly more. Besides this slight assurance that there actually is a difference, the simulations are essentially the same and the central value of  $10^{-3}\text{m}^2/\text{s}$  will remain the standard.

The bottom two rows of Figure 3.7 show variation from the base case with respect to vertical viscosities. In the case of high viscosity,  $v_{vhi}$ , the regions of positive and negative velocities are well defined and clearly separated, with both vertical and horizontal components being weaker than the previous cases. These characteristics are all present in the streamfunction as well, though partially obscured by the adjusted color scale. The low viscosity field is considered completely noise. The spurious vertical jets at the grid scale are not damped at all and even overwhelm the horizontal velocities. This explanation is analogous to the one made when considering the horizontal resolution, page 38. The velocities and streamfunction values obtained are unrealistic and, in combination with the high viscosity simulation, the choice of  $10^{-3}\text{m}^2/\text{s}$  is supported.

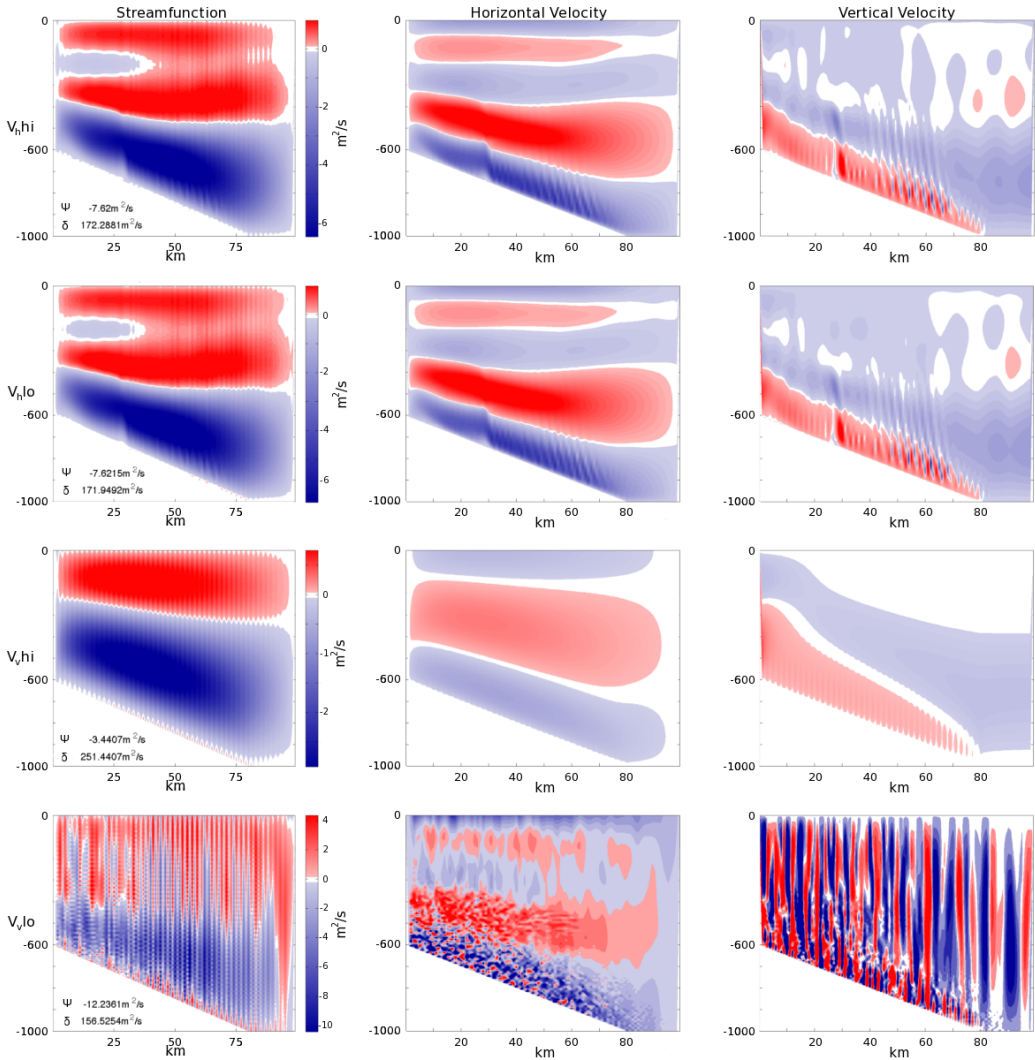


Figure 3.7: Shows sensitivity to viscosity coefficients, noting that  $\kappa_h$  is almost identical to  $\nu_h$ . The columns are  $\psi$ , U and W. The rows are of simulations with  $\nu_h$  100 times higher than lower, then the same changes to  $\nu_v$ . While the horizontal coefficients have almost no effect, vertical viscosity plays a huge part in suppressing or allowing the vertical waves seen at the grid scale.

The simulations just described cumulatively show that the MITgcm is capable of simulating the upslope dynamics caused by diffusion of a stable temperature gradient over sloping topography. The presence of features like the vertical waves motivate a second model, which will support the assumption they are numerical artifacts if they are indeed not reproduced under different numerics. The last results, of the parameter study, supports the choices made for the base case, and that it is adequate as a central point for the further investigation of the bottom-most cell, analogous to that seen in canyons near mid-ocean ridges.

## Chapter 4

# Finite Elements: The FEnICS Project

A second model was developed in order to help strengthen any conclusions based on MITgcm simulations and to help ensure effects that were assumed numerical are indeed not present in other model formulations. Though referred to as the FEniCS model, FEniCS technically refers to a group of interconnected coding libraries, the core of which are used to automate the process of interpreting the equations and creating the elements [Logg, 2007].

### 4.1 Equations

#### 4.1.1 Strong $\psi - \omega$ Form

From preliminary analysis on the MITgcm runs it is known that the streamfunction provides direct insight into the problem. With this information it was decided that a streamfunction formulation of (2.2) (p.23) would be beneficial and most accessible. The streamfunction with the sign convention already mentioned, with the negative on the vertical velocity (3.3), was used in substitution. In this way the conservation of mass, (2.2c), nicely becomes

$$\frac{\delta^2\psi}{\delta x \delta z} = \frac{\delta^2\psi}{\delta z \delta x}, \quad (4.1)$$

showing transitivity of derivatives. Substituting the streamfunction into the velocity equations, Equations 2.2a-2.2b, as well gives

$$\frac{D}{Dt} \frac{\delta\psi}{\delta z} + \frac{1}{\rho_c} \nabla_z p' = \nu_h \frac{\delta^3\psi}{\delta x^2 \delta z} \quad (4.2a)$$

$$-\frac{D}{Dt} \frac{\delta\psi}{\delta x} + \frac{gp'}{\rho_c} + \frac{1}{\rho_c} \frac{\delta p'}{\delta z} = -\nu_v \frac{\delta^3\psi}{\delta z^2 \delta x}. \quad (4.2b)$$

The total derivatives of Equations 4.2 are expanded, and partial derivatives are taken: the derivative of 4.2a with respect to  $z$  and the derivative of 4.2b with respect to  $x$ . Finding the difference these allow many cancelations which, when written with partial derivatives as subscripts, gives

$$(\psi_{tzz} + \psi_z \psi_{zzx} - \psi_x \psi_{zzz} - \nu_x \psi_{xxzz}) - (\psi_{txx} + \psi_z \psi_{xxx} - \psi_x \psi_{xxz} + \nu_z \psi_{xxzz}) = \frac{gp'_x}{\rho_c}, \quad (4.3)$$

in which pressure remains only in the term with gravity. Defining the vorticity with respect to stream-function and the Jacobian in the normal way,

$$\omega = -\psi_{xx} - \psi_{zz}, \quad \text{and} \quad J(a, b) = \frac{\delta a}{\delta x} \frac{\delta b}{\delta z} - \frac{\delta a}{\delta z} \frac{\delta b}{\delta x},$$

yields further simplification upon substitution when used in combination with Greene's formula. Dropping fourth order derivatives on viscosity produces the simpler-looking single equation,

$$\frac{\delta\omega}{\delta t} + J(\psi, \omega) = -\frac{\delta}{\delta x} \left( \frac{gp'}{\rho_c} \right) + \bar{\nu} \nabla^2 \omega. \quad (4.4)$$

As in the MITgcm model, salinity will be constant leaving pressure gradients solely dependent on temperature. Defining  $\alpha$  as the coefficient of thermal expansion, substitutions analogous to those resulting in (4.4) are performed on the equation for heat, (2.2d) (p.23). These two equations plus the definition used for vorticity are the strong form of the streamfunction vorticity equations for this system;

$$\frac{\delta\omega}{\delta t} + J(\psi, \omega) = -\frac{\alpha g}{\rho_c} \frac{\delta\theta}{\delta x} + \bar{\nu} \nabla^2 \omega \quad (4.5a)$$

$$\frac{\delta\theta}{\delta t} + J(\psi, \theta) = \kappa_x \frac{\delta^2\theta}{\delta x^2} + \frac{\delta}{\delta z} \left( \kappa_z \frac{\delta\theta}{\delta z} \right) \quad (4.5b)$$

$$\nabla^2 \psi = -\omega. \quad (4.5c)$$

### 4.1.2 FEniCS Equations

Several more manipulations must be done to this form to make it more suitable for use in numerical modeling. The first, nondimensionalization, introduces some complexity in the form due largely to requiring a separate scale for each length and height. Defining the scaling in terms of the domain size so that the new form will be on a unit square,  $x = L\hat{x}, z = H\hat{z}$ . Distributing the length and height scales through the Jacobian is simply a derivative in both directions,  $J(\cdot, \cdot) = \frac{1}{LH}\hat{J}(\cdot, \cdot)$ . The scaling for temperature is simply  $\theta = \Theta\hat{\theta}$ , which will be set to one. Matching units of the remainder of the variables suggest a common scaling, and particularly one that allows the streamfunction to scale with horizontal viscosity;  $\psi = \nu_x\hat{\psi}$  implying  $\omega = \frac{\nu_x}{H^2}\hat{\omega}$ . Assuming advective time scaling,  $t = \frac{HL}{\nu_x}\hat{t}$ . These produce the nondimensional version of (4.5) which, neglecting hats, is

$$\frac{\delta\omega}{\delta t} + J(\psi, \omega) = -Ra\frac{\delta\theta}{\delta x} + A_r\frac{\delta^2\omega}{\delta x^2} + r_\nu A_r^{-1}\frac{\delta^2\omega}{\delta z^2} \quad (4.6a)$$

$$\frac{\delta\theta}{\delta t} + J(\psi, \theta) = Pr^{-1} A_r\left(\frac{\delta^2\theta}{\delta x^2} + A_r^{-2}\frac{\delta}{\delta z}(r_\kappa\frac{\delta\theta}{\delta z})\right) \quad (4.6b)$$

$$A_r^2\frac{\delta^2\psi}{\delta x^2} + \frac{\delta^2\psi}{\delta z^2} = -\omega. \quad (4.6c)$$

These equations already have scales combined and simplified to include a Rayleigh number,  $Ra = \frac{g\alpha H^3\Theta}{\rho_c\nu_x^2}$ , a Prandtl number,  $Pr = \frac{\nu_x}{\kappa_x}$ , and several other nondimensional parameters  $A_r = H/L$ ,  $r_\nu = \nu_z/\nu_x$ , and  $r_\kappa = \kappa_z/\kappa_x$ . This last parameter is notably different than the others mentioned as it is not constant for a given simulation. It can be thought of as weighted by the horizontal diffusion, while still a function of spatial position,  $r_\kappa = r_\kappa(\vec{x})$ , which is the parameter that is altered when simulations change  $\kappa_{max}$ . The parameters varied within the FEniCS model are most accessible in this form. From testing done with the MITgcm, base case values have already been determined for the aspect ratio of the domain ( $A_r = 0.01$ ) as well as the constant viscous and thermal diffusion ratios ( $r_\nu = 1 = Pr$ ). The Rayleigh number reflects the changes to a single aspect of the domain scale since the dependence on  $H$  is the only influence on the equations besides the aspect ratio.

Though this form is nondimensionalized, a weak form must be found to be interpreted by the FEniCS software. In general a weak form is found by multiplying each equation by a test function and integrating over the domain. The test function is denoted  $v_.$ , where the subscript is the dependent variable of a given equation. Then integration by parts can be used on terms with second-order derivatives. Though differentiation introduces a requirement on  $v_.$ , the requirement on the dependent variable is weakened. As an example this process will be carried out for the Poisson equation (4.6c); after multiplication by the test function and integration over the domain,  $\Omega$ , the equation is

$$\int_{\Omega} v_{\psi} (A_r^2 \frac{\delta^2 \psi}{\delta x^2} + \frac{\delta^2 \psi}{\delta z^2}) dx = - \int_{\Omega} v_{\psi} \omega dx.$$

A benefit of the weak form is to reduce the order of derivatives which can be seen from the terms on the left after integrate by parts

$$\int_{\delta\Omega} (v_{\psi} A_r^2 \frac{\delta \psi}{\delta x} + v_{\psi} \frac{\delta \psi}{\delta z} ds) - \int_{\Omega} (A_r^2 \frac{\delta v_{\psi}}{\delta x} \frac{\delta \psi}{\delta x} + \frac{\delta v_{\psi}}{\delta z} \frac{\delta \psi}{\delta z}) dx = - \int_{\Omega} \omega v_{\psi} dx.$$

The first term here simplifies, as the derivative over the boundary can be broken into Dirichlet and Neumann parts. Test functions,  $v$ , are chosen to vanish where the function is known on the boundary, precisely the Dirichlet boundary condition, and so the integral over that portion is identically zero. The remaining portion,  $\bar{h}_{nbc}$ , is named to reflect its dependence on the Neumann condition and results in the full weak form

$$\int_{\Omega} (A_r^2 \frac{\delta v_{\psi}}{\delta x} \frac{\delta \psi}{\delta x} + \frac{\delta v_{\psi}}{\delta z} \frac{\delta \psi}{\delta z}) dx = \int_{\Omega} \omega v_{\psi} dx + \int_{\delta\Omega} v_{\psi} \bar{h}_{nbc,\psi} ds.$$

The process performed for the Poisson equation is extended, with no new difficulties, to the other two equations. The result is the weak nondimensional streamfunction-

vorticity equations, that are the basis for the implemented FEniCS model,

$$\begin{aligned} & \int_{\Omega} (v_{\omega} \frac{\delta \omega}{\delta t} + v_{\omega} J(\psi, \omega)) dx \\ &= - \int_{\Omega} v_{\omega} Ra \frac{\delta \theta}{\delta x} dx - \int_{\Omega} (A_r \frac{\delta v_{\omega}}{\delta x} \frac{\delta \omega}{\delta x} + r_{\nu} A_r^{-1} \frac{\delta v_{\omega}}{\delta z} \frac{\delta \omega}{\delta z}) dx \\ &+ \int_{\delta\Omega} \phi k v_{\omega} \bar{h}_{nbc,\omega} ds \end{aligned} \quad (4.7)$$

$$\begin{aligned} & \int_{\Omega} (v_{\theta} \frac{\delta \theta}{\delta t} + v_{\theta} J(\psi, \theta)) dx \\ &= - \int_{\Omega} (Pr^{-1} A_r (\frac{\delta v_{\theta}}{\delta x} \frac{\delta \theta}{\delta x} + A_r^{-2} r_{\kappa} \frac{\delta v_{\theta}}{\delta z} \frac{\delta \theta}{\delta z})) dx \\ &+ \int_{\delta\Omega} v_{\theta} Pr^{-1} A_r \bar{h}_{nbc,\theta} ds \end{aligned} \quad (4.8)$$

$$\begin{aligned} & \int_{\Omega} (A_r^2 \frac{\delta v_{\psi}}{\delta x} \frac{\delta \psi}{\delta x} + \frac{\delta v_{\psi}}{\delta z} \frac{\delta \psi}{\delta z}) dx \\ &= \int_{\Omega} \omega v_{\psi} dx + \int_{\delta\Omega} v_{\psi} \bar{h}_{nbc,\psi} ds. \end{aligned} \quad (4.9)$$

To emphasize, no variables need more than to be once differentiable. A boundary integral incorporating any Neumann conditions appears in the other two equations from differentiation by parts, just as with the Poisson equation. The boundary of the domain is represented by  $\delta\Omega$  in the line integrals and  $s$  is the associated variable of integration.

Finite element methods here, as is usually the case, only deal with spatial discretization, so time must still be considered. Temporal discretization is done with finite difference methods, splitting time into steps of length  $k$  with the current and previous time's parameter values denoted by subscripts 1 and 0, respectively, on all three of the dependent variables,  $\omega$ ,  $\theta$  and  $\psi$ . A discretization parameter,  $\phi$ , is introduced for generality, though only the Crank-Nicholson scheme,  $\phi = 0.5$ , is used. Culminating from this described process are the nondimensional equations for this variational problem in their fully discretized form,

$$\begin{aligned}
& \int_{\Omega} v \omega_1 + \phi k [A_r \frac{\delta v}{\delta x} \frac{\delta \omega_1}{\delta x} + r_\nu A_r^{-1} \frac{\delta v}{\delta z} \frac{\delta \omega_1}{\delta z} + v J(\psi_1, \omega_1)] dx \\
&= \int_{\Omega} (v \omega_0 + (1 - \phi) k v [A_r \frac{\delta^2 \omega_0}{\delta x^2} + r_\nu A_r^{-1} \frac{\delta^2 \omega_0}{\delta x^2} - J(\psi_0, \omega_0) - Ra \frac{\delta \theta_0}{\delta x}]) dx \\
&\quad - \int_{\Omega} \phi k v Ra \frac{\delta \theta_1}{\delta x} dx + \int_{\delta\Omega} \phi k v \bar{h}_{nbc} ds
\end{aligned} \tag{4.10a}$$

$$\begin{aligned}
& \int_{\Omega} (v \theta_1 + \phi k [Pr^{-1} A_r (\frac{\delta v}{\delta x} \frac{\delta \theta_1}{\delta x} + A_r^{-2} r_\kappa \frac{\delta v}{\delta z} \frac{\delta \theta_1}{\delta z}) + v J(\psi_1, \theta_1)]) dx \\
&= \int_{\Omega} (v \theta_0 + (1 - \phi) k [Pr^{-1} A_r (\frac{\delta^2 \theta_0}{\delta x^2} + A_r^{-2} \frac{\delta}{\delta z} [r_\kappa \frac{\delta \theta}{\delta z}]) - J(\psi_0, \theta_0)]) dx \\
&\quad + \int_{\delta\Omega} \phi k v Pr^{-1} A_r \bar{h}_{nbc} ds
\end{aligned} \tag{4.10b}$$

$$\int_{\Omega} (A_r^2 \frac{\delta v}{\delta x} \frac{\delta \psi}{\delta x} + \frac{\delta v}{\delta z} \frac{\delta \psi}{\delta z}) dx = \int_{\Omega} \omega v dx + \int_{\delta\Omega} v \bar{h}_{nbc} ds. \tag{4.10c}$$

The boundary conditions applicable to the modeled area make use of either pure Dirichlet or Neumann conditions. The temperature condition is the no-flux boundary condition pictured in the physics explanation, Figure 2.2. This corresponds to the homogenous Neumann condition which, although affects the equations, is simply  $\bar{h}_{nbc} = 0$  eliminating the integral. As already described, Dirichlet conditions do not appear in the weak form of the equations explicitly. This type of boundary condition is accounted for in the matrix representation of the equation. The streamfunction, by definition is only accurate up to a constant, so a homogenous Dirichlet condition is used to specify this. The most straightforward boundary condition for vorticity makes use of the free-slip condition on velocity,

$$\frac{\delta \vec{u}_\parallel}{\delta \hat{n}} = 0 \quad \text{for } \vec{x} \in \delta\Omega,$$

where parallel and normal directions are in relation to the boundary. In addition to this, there is also a logical no-flux condition on velocity which when combined imply a homogenous Dirichlet condition for vorticity.

## 4.2 FEniCS Components and Equation Implementation

The weak form of the equations, (4.10), are written in the ‘Unified Form Language’ used by FEniCS to represent differential equations independent of compiler choices. The ‘FEniCS Form Compiler’ (FFC) is software that interprets this description and generates C++ code. The FFC is one of the main components of the FEniCS libraries allowing a variational form, such as 4.10, to be quickly implemented for finite element solving methods. For this compiler, the weak form is separated into bilinear and linear parts, RHS and LHS of the equations (4.10) respectively, for formulation into their own matrices. The components are further specified as test functions, trial functions, and variable coefficients allowing the compiler to treat them as needed during the construction. Construction also requires knowledge of the mesh and type of elements, with the end result being a linearization of each equation into a form analogous to the classic  $Lx = b$ .

The ‘FInite-element Automatic Tabulator’ (FIAT) is able to generate the elements needed for the matrices with arbitrary order and with choice of many of the common forms. For most simulations done here, the most basic first order Lagrange elements are used. The elements referred to here include a basis function over each of the cells, which for our two dimensional domain are triangular. First order indicates the basis functions are each piece-wise linear and so only need nodes at the mesh vertices. FIAT will generate these elements with little involvement after generating the mesh and determining the element type. These basis functions are doubly useful given the Galerkin methods that are used, which uses them to specify both the test and trial functions of the equations (4.10). Besides automating the process for the interior, creating additional basis functions for boundary elements, for use when needed for Neumann conditions, is also handled at this point.

Once the matrices representing these equations are created, the FEniCS software allows multiple backends for solving the resulting linear algebra problems. All model simulations in this study made use of PETSc LU-solver. This type algorithm relies on decomposing a matrix into lower and upper triangular parts which, although requiring computation to find the two parts, becomes very efficient if the same

operator is used repeatedly as it is in our time-series simulation.

The system of equations present in Equation 4.10 are not directly solvable by these linear methods due to the inherently nonlinear nature. To get around this, the equations are solved with a Picard-Newton method. For this, each equation assumes the other variables are constant while solving for the new state. In terms of the interpretation by the FEniCS components described, this iterative method makes the system into three separate variational problems which are related only in the highest level of FEniCS components, Dolfin [Logg and Wells, 2010]. Dolfin is the user interface of the FEniCS ‘model’ and provides a wrapper for the other components, managing most of the communication between the core components and also third-party programs such as PETSc . Version 0.9.10+ was used for the simulations documented within this study.

The Picard-Newton iterative scheme used updates a solution while checking the residual concerning convergence, as summarized in Algorithm 4.1. More specifically the three equations in their linear forms,  $Lx = b$ , are solved in series to find an intermediate state, and the process repeats until deemed close enough to a converging solution. Within the algorithm, subscripts with n’s are an iteration index, superscripts are a time index, and the variables being solved for,  $\theta$ ,  $\psi$ , and  $\omega$  are analogous to the linear form’s x. The  $L$ . is an operator that assumes its indicated dependencies are constant and  $b$ . is fully determined by previous states of the model. First, the streamfunction state from the previous timestep is assumed close to its solution for the new time, which makes use of continuity of the variables. These values are used, as if a true solution, to solve for a new state of potential temperature. The pair,  $\psi$  and  $\theta$  is used to solve for an intermediate solution to  $\omega$ , which is then used to update the streamfunction through the poisson equation. The whole process is repeated at least once starting with the solutions from the previous cycle, and checked for convergence. The  $L^2$ -norm of the residual between the latest version of streamfunction,  $\psi_{n+1}$ , and that of the one before,  $\psi_n$  is calculated, where subscripts denote the iteration index. Once this proxy for convergence is below a set tolerance the last state of all three variables are considered the solution for the new timestep.

```

 $\psi_0 = \psi^t$ 
For n=1 until convergence
 $\theta_n = L_\theta(\psi_{n-1}) \setminus b_\theta$ 
 $\omega_n = L_\omega(\psi_{n-1}, \theta_n) \setminus b_\omega$ 
 $\psi_n = L_\psi(\omega_n) \setminus b_\psi$ 
<Convergence test>:
If  $\|\psi_n - \psi_{n-1}\|_2 < tol \|\psi_n\|_2$ 
 $\{\omega, \psi, \theta\}^{t+1} = \{\omega, \psi, \theta\}_n$ 
End

```

Algorithm 4.1: Picard-Newton iteration algorithm used within FEniCS model. Solving the three distinct linearized systems, with subscripts of n representing the intermediate values and superscripts representing time step. Only the dependencies on the current timestep are noted, while the previous timestep is considered implicit in the linearization.

If this does not occur within 20 iterations or if the norm increases above an upper limit, the model is forced to halt.

A first test case of the model reduces the system back from the three-equation discretization of Equations 4.10, and temporarily postpones the need for the iterative solving scheme. A basic test of the advection scheme was done with  $\kappa_x = 0 = \kappa_z$  and omitting the Poisson equation. Specifying a uniform constant background that will sweep a gaussian of temperature across half the domain in 50 time steps is easily checked by an analytical translation of the initial temperature. Making use of the  $L^2$  norm, it is shown that the even at these high velocities the advection scheme has greater than 98% accuracy. The quick calculation having such a result brings confidence that the Crank-Nicholson scheme with linear elements is sufficient, at least in terms of advection.

As the model is expanded back to three equation simulations, some post-processing is required before easily comparing with the MITgcm results. A uniform grid similar that used by the MITgcm is created and the FEniCS model interpolates the

solutions onto it before recording any output. The data in this form are easily translatable into all the methods for analyzing the previous cases. Finally, with all the pieces assembled, simulations are performed to check the full system and explore the differences as compared to the MITgcm.

## 4.3 Preliminary Examination

### 4.3.1 First Simulation

Trivial cases run on the MITgcm, such as no slope and uniform temperature, were run as tests and passed. While many other cases were rerun, the agreeing results are omitted to avoid unnecessary redundancy. After these the base case simulation was run with the FEniCS model, which in useful repetition of the MITgcm will be examined. While the variables stated in the initial case of the MITgcm were mostly kept, the one difference is repeated: the smaller decay scale of  $250m$  was adopted to obtain diffusion values of less intensity at the top of the domain. In contrast from the MITgcm, the transients will not be viewed over as wide an interval of time but will make use of the decided spinup time and look more closely around it, Figure 4.1.

The first things to note are that the streamfunction minima, shown by a green line at the top of Figure 4.1 is very similar to what was seen in the MITgcm (green line in the time series from Figure 3.4 (p.36)). In addition, the central plot of the 20 day snapshot of the streamfunction, is also similar to that shown from the other model. The remaining eight snapshots of streamfunction are all from the same simulation run, with base case parameterization, and were chosen to display the transience of the dynamics near the allocated spin up time. The top left streamfunction plot is from 12 days, and like all these plots is labeled by the model time elapsed and marked on the timeseries with a black circle.

A distinct characteristic of these plots is the temporal dependence of the upper third of the domain, changes most easily observed by watching the upper negative cell. In the first image, 12 days, the left of the positive cell splits to have two extrema visible. This weakens the right side so in the next two snapshots a negative cell is

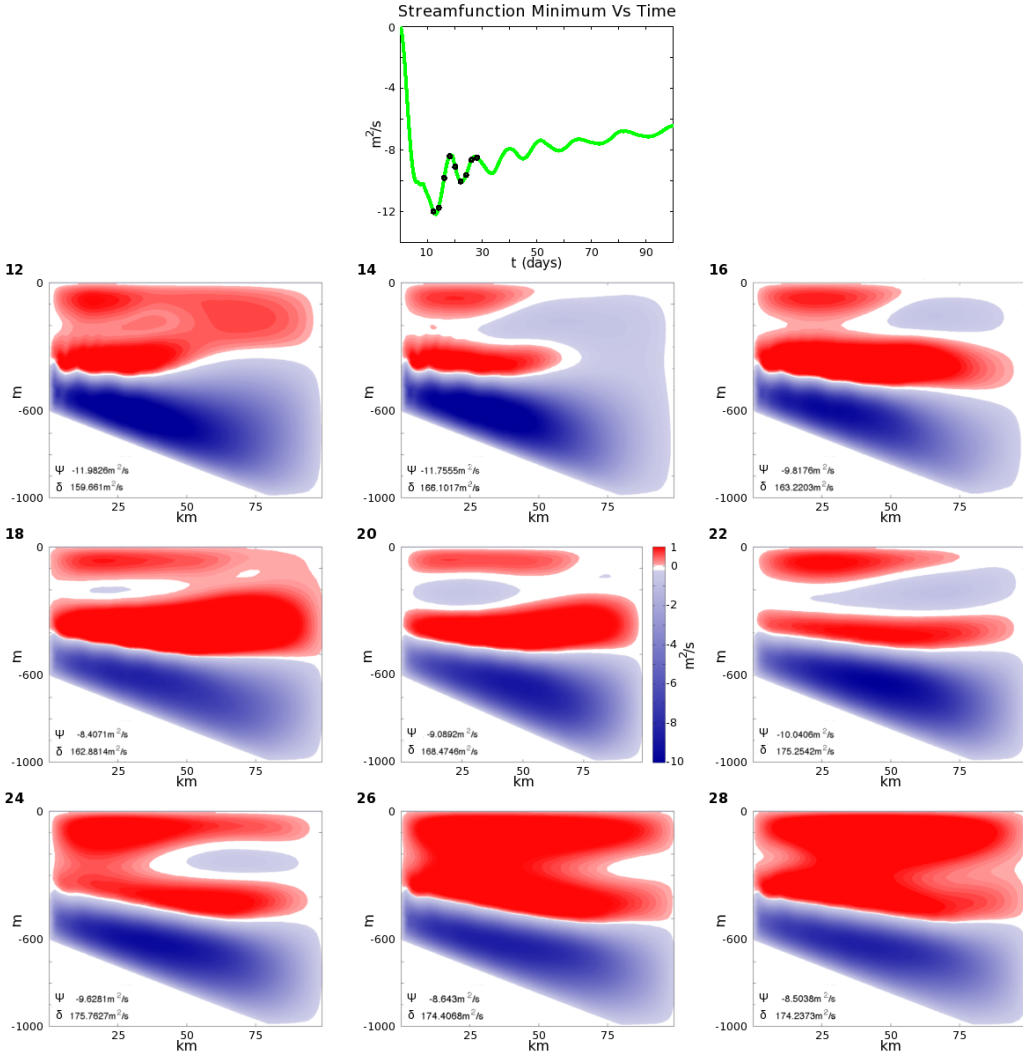


Figure 4.1: Shows  $\psi_{min}$  vs time along with plots of streamfunction near the spinup of 20 days. The circles on the green line indicate the times where snapshots are shown. The nine snapshots are labeled by the number of days elapsed in simulation, progressing two days at a time, from left to right then top to bottom. The normal spinup is centered showing the scale all plots have. Within the 16 days displayed, an upper negative cell makes two full oscillations of the domain length, demonstrating the transience of this upper region.

moving across to the right. The shift is not fully obvious as the contours from the lower cell actually merge into the top. By day 16 the negative cell is weakening, becoming more positive, as the maxima of the positive cells shift toward the right. Though never fully reconnecting there is almost no true negative  $\psi$  as the local minimum moves back across to the left. This is shown at day 18, which is almost exactly at the time of an extrema of the timeseries. The remaining snapshots show the negative cell moving back across the top through the allocated spin-up time, 20 days, and another local extrema of the timeseries, 22 before almost all trace of the cell is gone at the next timeseries extrema at 28 days. After this the uppermost positive cell becomes more stable and the oscillation is confined to the strength of a central positive cell near the left and a central negative cell near the right. From this view, the behavior in these cells can be seen to be a wave oscillating back and forth across the entire domain.

Attempts to match this wave-like behavior to the oscillations seen in the time-series of streamfunction minima reveal little connection. Qualitatively the streamfunction snapshots from day 12 and 28 might be considered similar, but they represent a local minimum and maximum in the timeseries, at the top of Figure 4.1. Not only that but  $\psi_{min}$  has two other local extrema within this time-range, near 18 and 22 days, that do not appear to be special places within the wave of the upper cells. In another attempt to connect  $\psi_{min}$  with the behavior of the upper cells, the oscillation in the timeseries was looked at as a wave. The period almost doubles by the end of the 100 day run from its original length of about 10 days for the range of snapshots depicted. Yet at no point is it quite as short as the period of the wave seen in the upper cells. With similar-looking snapshots of  $\psi$  matching different timeseries extrema, some extrema not aligning to anything apparent in upper cell behavior, and different periods of oscillation, there is basically no connection seen between the upper cells and the strength of the lower cell. This apparent disconnect is used as justification for ignoring the behavior of the upper domain when analyzing the lower.

The temporal oscillation in the streamfunction minimum raises questions about

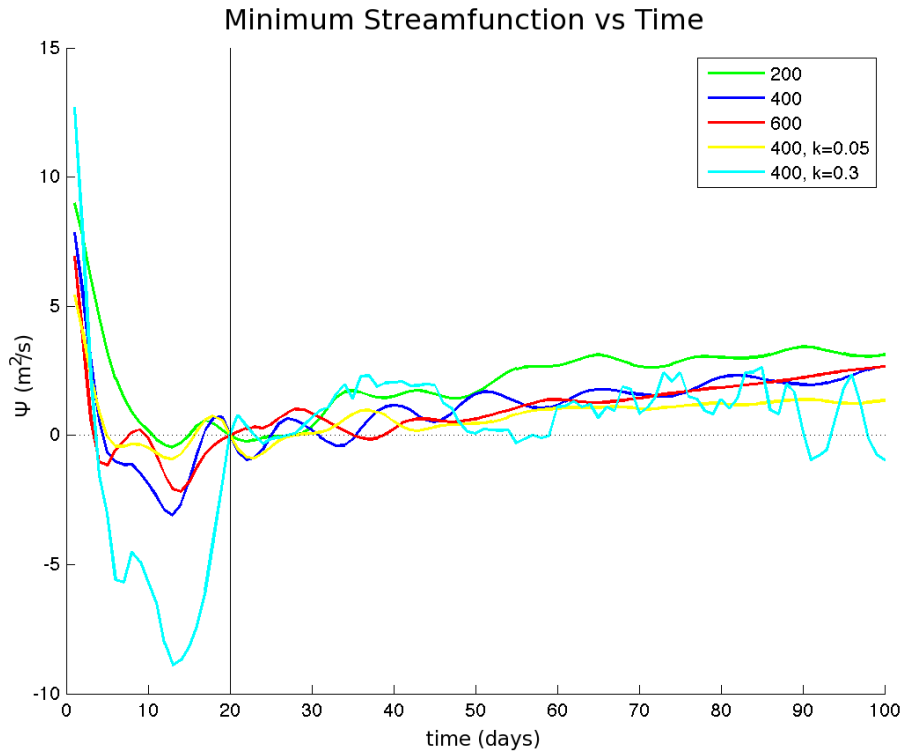


Figure 4.2: Shows timeseries for streamfunction minima for a variety of simulations. The diagnostic  $\psi_{min}$  was calculated as normal for a variety of simulations. Except for the ones noted in the legend, all values are from the base case. The first three simulations, in green, blue and red, show rises of 200, 400, and 600m at base diffusivity of  $\kappa_{max} = 0.1m^2/s$ . The last two, in yellow and cyan, show the base rise of 400m with lower and higher diffusivities. All series were shifted by a constant so that the value of  $\psi_{min}$  was 0 at 20 days.

the usefulness of a spin-up period fixed across all simulations. While there would be some difference in  $\psi_{min}$  dependent on the phase of oscillation occurring at that time, the obvious methods to account for it introduce many of their own problems. Figure 4.2 shows the timeseries for the diagnostic  $\psi_{min}$  of multiple simulations at base parameterizations except for the indicated changes. Each timeseries is shifted to be zero at the spinup time, 20 days, and so the value plotted is actually the difference of  $\psi_{min}$  from the value at that time. The 20 day ‘zeroing’ is further emphasized by a vertical line at this time and a dotted line at  $y=0$ . Simulation results from runs with three different slope angles were plotted using green, blue and red, for rises of 200, 400 and 600m. Two other simulations are shown having diffusivities other than the base of  $0.1\text{m}^2/\text{s}$ : yellow has  $\kappa_{max} = 0.05\text{m}^2/\text{s}$  and cyan  $\kappa_{max} = 0.3\text{m}^2/\text{s}$ . They all have a positive trend after the spinup period, which indicates a weakening lower cell, but the strongest diffusion appears to display influences not present in the others reaching stronger values at a few timesteps. Another notable feature is that, besides the base case blue, the oscillation does not appear to have a clear period, much less a constant one. This would create issues with the most obvious alternative to a single spin-up time, including an average over an interval of steps. Without a clear period, even dynamically choosing an interval to average over will likely be biased, not unlike a single timestep, and would additionally obfuscate what that bias is. The qualitative decay after the given point further support the time chosen is large enough, while the simplicity of a single time makes it more telling than alternatives. To support the choice of the given spinup time, a few of the later plots will also include data taken at 30 days to show the same trends occur.

Besides this oscillation in time, there is also a wave that appears between the cells. Especially visible before 20 days in Figure 4.1, it can be seen by following the interface between the lowermost cell and the one above it. Focusing on the left boundary, the negative cell is noticeably higher than a smooth interface would place it. The apparent overshoot followed into the interior, oscillates and seems to be damped. Though the amplitude appears to dissipate over time, it motivates a look at resolution to assess if it is completely numerical and minimize any such part

of the phenomena.

### 4.3.2 Resolution

Other qualitative comparisons were performed during the establishment of the FEniCS model, many of which will be covered in the results chapter 5. This included several of parameter tests done in simple repetition of the ones reported in chapter 3. Besides this, significant work was put into studying resolution dependence on the finite element model, as was mentioned after looking at the transient behavior of the streamfunction's upper cells. The implicit nature of the methods for solving the equations make time less important in determining stability of the solutions, making the mesh central in the investigation on resolution.

From the start of the FEniCS models, the simulations took advantage of easy access to nonuniform gridding. The nondimensional nature of the problem means any domain can be a transformation of a unit square. Through the scalings it can be seen this applies only in terms of an aspect ratio and indirectly through the Rayleigh number's dependence on height, best seen in the non-discretized nondimensional equations (4.6). Removing a portion of the unit square creates the sloping region, and Gmsh [Geuzaine and Remacle, 2011] was used to create a triangulation of this region. This triangulation became a globally defined mesh and was used for all simulations of the given slope, but could be refined for a single run through a FEniCS package.

The base slope, 400m rise, was simulated with meshes of various levels of refinement to observe the effect on the solution, specifically the oscillation seen at the cell-interface. Figure 4.3 shows snapshots of streamfunction from these runs taken after 20 days elapsed within the simulation. The specification of the runs having  $\kappa_{max}$  at its largest,  $0.3m^2/s$ , to ensure the interfacial wave is strongly formed. As will be seen, Sec. 5.2.1, the strength of  $\psi_{min}$  increases with  $\kappa_{max}$  and thus so does the amplitude of the perturbation. While being looked at in terms of resolution like the wave seen in the MITgcm, Sec. 3.2 (p. 38), it should be made clear these are not the same as the domain boundary is perfectly resolved though boundary layers

may not be.

In addition to the normal snapshot, the subplots display the top portion of their meshes at depths of 0 to 100m. These sections are a good representation as the mesh parameters are constant vertically, and only including any nonuniform for the last two presented here. The cases shown start with a coarse *mesh*, Figure 4.3-m0 with cell diameter of approximately  $1/20^{th}$  of a side of the unit square containing the mesh. Going down the column the resolution is doubled each time the mesh is refined. Uniform refinement is completed by taking the midpoint of each side of the triangle and connecting the three new nodes, splitting every triangular cell into four. The pattern of doubling continues for m1, m2 and onto m3 in the second column. The remaining two plots are refined in a more complex method that focuses on the boundary at the top of the slope. For the first *nonuniform* refinement mesh, n4, every cell with at least one vertex the leftmost 10% of the domain was refined, this area was halved and the cells closer to the boundary were refined again. The last mesh, n5, was a uniform refinement of the previous.

The coarse mesh case, m0 of Figure 4.3 shows a large perturbation as was expected. The interfacial oscillations dominates the structure of the cells in the center so much to even have resemblance to the grid underneath. One level, m1, of refinement drastically improves the interface even at this intense diffusivity, though none of the get rid of it completely. The second level of refinement does affect the length of the oscillation, implying something is left unresolved but the amplitude remains similar. The finest mesh still shows traces of the perturbation especially at the left boundary, but by now a single oscillation covers many mesh cells. In fact, the perturbation at this point actually has bigger amplitude than the previous refinement. The first case of local refinement seems to do worse than the first uniform refinement, especially considering the interface away from the left boundary. For accurate comparison, the characteristics of the mesh in Figure 4.3-n4 are equivalent to m3 near the left boundary but in between m1 and m2 over most of the domain. Whereas n5 has a mesh finer than m3 near the left boundary and equivalent to m2 over the majority.

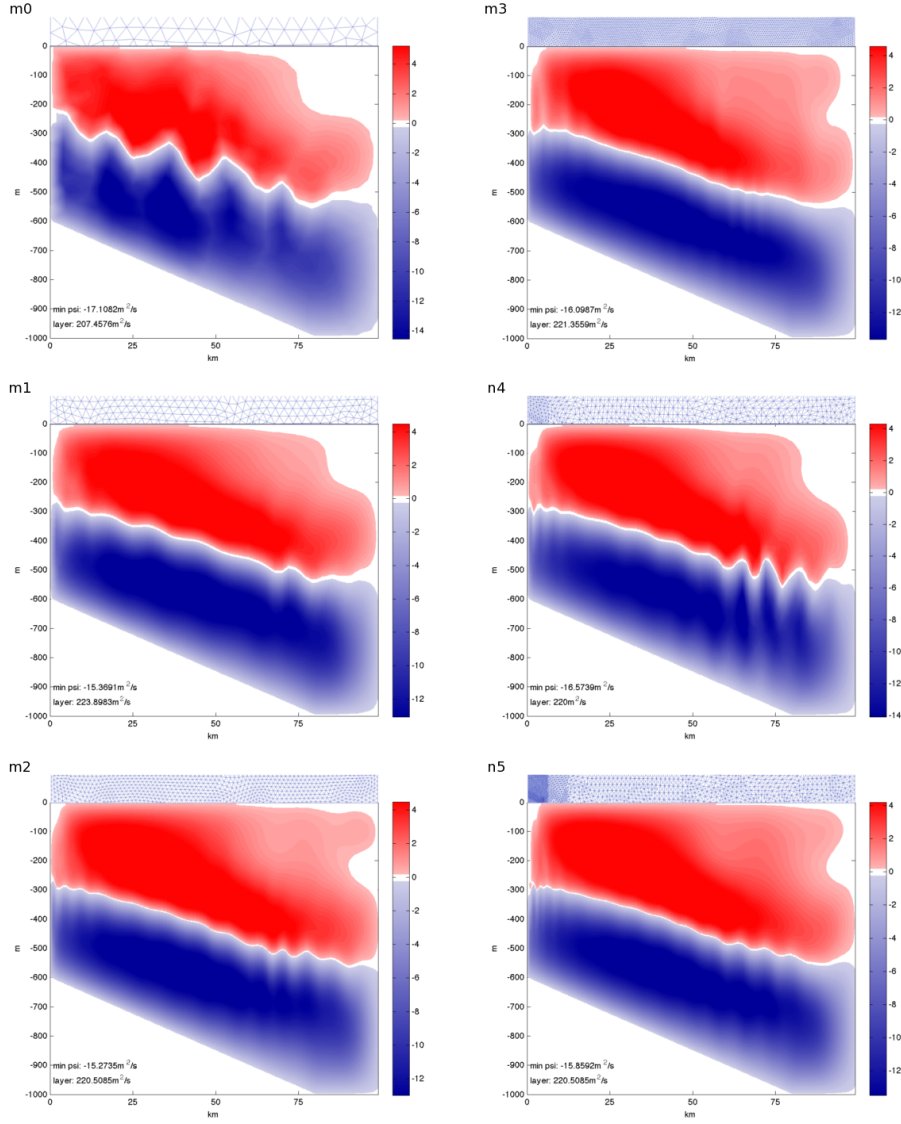


Figure 4.3: Shows the base simulation at 20days with different meshes. The simulations were of the base case with  $\kappa_{max} = 0.3m^2/s$  and meshes with different levels of refinement. Streamfunction is plotted the mesh is visible in extension above each plot. Starting with m0) a coarse mesh with 20 nodes per side, the resolution is doubled once (m1), twice (m2) and finally a third time (m3). The nonuniform refinement focuses on the top boundary where the interfacial perturbation seems to begin (n4) and then doubles that resolution (n5). See text for details.

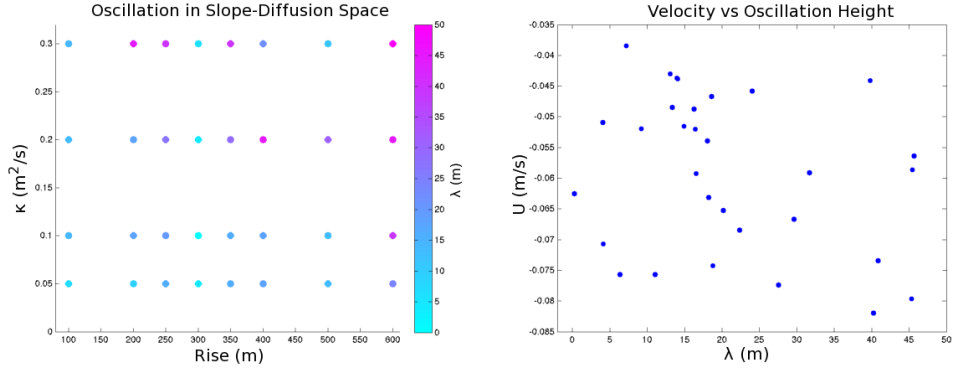


Figure 4.4: Shows two methods of further investigating the oscillation between streamfunction cells. The left displays the wave-height in terms of both the main independent variables. Here, the larger oscillations are seen to occur at higher slopes and diffusivities in general, yet there are cases such as central slopes at highest diffusivity where small amplitudes are found. The right plot shows the same wave-height with respect to a derived horizontal velocity, found from  $\psi_{min}$ . The lack of apparent correlation further emphasizes the absence of straightforward explanation.

The result of these simulations suggest that there is, in fact, a numerical effect, likely related to a boundary layer that is not being fully resolved even at the scale of the n5 refinement. Using an inertial argument, the upward flow in the partially resolved layer has momentum and overshoots the point where buoyancy is neutral. As the oscillation moves away from the wall it is damped by viscosity. Relating the cause of this effect to a discontinuity implies the perturbations are analogous to a Gibb's phenomena, which explains why the amplitude did not improve much after the first uniform refinement. Accepting that the boundary layer causing this oscillation will not be adequately resolved without high levels of refinement, as supported by the same amplitude appearing in the finest meshes tested, the mesh of first refinement was assumed adequate for diffusion up to the displayed  $0.30 m^2/s$ .

Having chosen an adequate mesh refinement, some further investigation was performed in attempt to explain the hypothesized physical aspect of the phenomenon. In order to do so a wave-height ( $\lambda$ ) was defined and compared throughout the slope-diffusion space of the simulations. First, the interface was located by determining

the position in each column where  $\psi$  rises to 0. The series of these positions,  $H(x)$ , was examined to find the first local maximum and then minimum, with respect to the left boundary. The difference in interface height between these two points is the wave height used. Figure 4.4 shows two attempts at determining a scaling of the heights. On the left, the grid of experiments is shown with maximum diffusivity increasing upward and slope increasing to the right. The color is  $\lambda$  and shows no obvious pattern. While the experiments with both low  $\kappa_{max}$  and shallow slope have smaller wave-heights, the cases with either high rise or diffusion are not as consistent. For specific examples,  $\lambda$  remains relatively constant between all used diffusions for a rise of 300m and actually decreases for the strongest mixed case at 500m rise.

Another method of comparison was to compare the oscillation change to a calculated horizontal velocity. The velocity used,  $U$ , is determined by the two global diagnostics  $\psi_{min}$  and  $\delta$ , which will be thoroughly explored in the next chapter (Ch. 5). Although velocity and wave-height are intuitively connected, in the sense of inertia, the right side of Figure 4.4 shows very little correlation. Thus the explanation supported within these studies remains tied to numerical resolution, while any physical influences are not obvious from the main parameters varied in these simulations.

The faster progression through preliminary results of the FEniCS model relied heavily on the presentation of the MITgcm's results. Even so this more brief presentation is sufficient to include the differences. A direct comparison between results of the two models will be done, Sec 5.1, before launching into results from the models in the balance of Ch 5. The focus on the FEniCS model did further justify several of the choices made in Ch. 3, like spin-up time, while making use of others, such as the viscosity values. Though a new perturbation appears from a boundary layer at the top of the slope that is not full resolved, the previously seen vertical waves from the MITgcm do not appear in the nonuniform meshes approximation of the terrain. With the qualitative similarities to MITgcm results and the look at several parameters already, there is much confidence in the FEniCS built model capturing the important aspects of the dynamics occurring within the simulated MOR canyons.



## Part II

# Analysis and Discussion



## Chapter 5

# Results and Analysis

In the model specific chapters, Ch. 3 (p. 25) and Ch. 4 (p. 45), the validity of each model was established with respect in and of itself. There were several loose ties made between them, such as using parts of the robustness testing from the MITgcm in directing the choice of initial parameterizations for FEniCS (ex. viscosity values and  $\psi$ ). Due to this the models could be run in parallel and quickly compared. The first part of the present chapter, Section 5.1 does just that, closely comparing a single run and also the diagnostics from a variety of runs. Due to the similarity that will be demonstrated, the FEniCS model becomes the primary focus to allow continuity in the presentation of results. Section 5.2 goes into details with respect to the two main diagnostic values, layer height ( $\delta$ ) and streamfunction minimum ( $\psi_{min}$ ), and two independent parameters are focused on in determination of dependencies, namely slope and maximum diffusivity. The last section, 5.3, expands the focus somewhat by introducing a few other parameters largely to generalize the results.

### 5.1 Model Comparison

The base case setup is used as a starting point for this and the following comparison, which remains the same as in the development chapters, Ch. 3 and 4. The slope is proportional to a 400m rise in topography over 80km to reach the left boundary, and the maximum diffusivity at each point along the topography is  $0.1\text{m}^2/\text{s}$ . A standard

spin-up of 20 days results in qualitatively similar dynamics between models, shown in Fig. 5.1. The main focus of this study is on the upslope flow generated near the boundary, and so the similarity in the negative cell of  $\psi$  is most important. As during the models' development, the negative (positive) values of streamfunction are represented in blue (red) and indicate clockwise (counterclockwise) flows. The figure also lists both extrema of the streamfunction which are comparable, having about a 20% difference in magnitude for the bottom cell. In addition to magnitude, the shape of the lower cell is very similar and the size, most easily noticed where the cell interfaces intersect the left boundary, is approximately the same.

While there is nothing significant enough to overturn the agreement between the models on this run, there are several differences to be noted. Discrepancies in the magnitude of  $\psi_{min}$  have already been pointed out, and the noise-like waves in the MITgcm and interface oscillation in the FEniCS model are expected from preliminary testing. The other main difference is the shape of the upper cells, which while briefly described already, will be covered more later. In the case of this current figure (5.1), the differences in the upper part of the domain are mostly temporal as the additional negative cell(s) spreads across the domain. With behavior like this in mind, the MITgcm actually contains two positive cells that are being forced apart as the negative cell forms and spreads across.

The similar nature so far is based on a single case, which is extended by comparing the minimum streamfunction and layer height across the parameter space. The independent variations of two parameters, both centered on the base case, are listed for comparison in Table 5.1. Specifically, the maximum diffusivity is halved and doubled from the central value ( $0.1 \text{ m}^2/\text{s}$ ) and also the rise in topography is decreased and increased by 200m from the base 400m. The layer height,  $\delta$ , is an estimate of the thickness of the layer of upslope velocity and is not the cell height which would include some down-canyon velocities. This thickness is derived from the mean location of column streamfunction minimums for a given timestep, as was demonstrated previously by Figure 3.3 (p. 35). In correspondence to the visual estimate of cell heights in the streamfunction snapshot, Figure 5.1, the values for  $\delta$  are

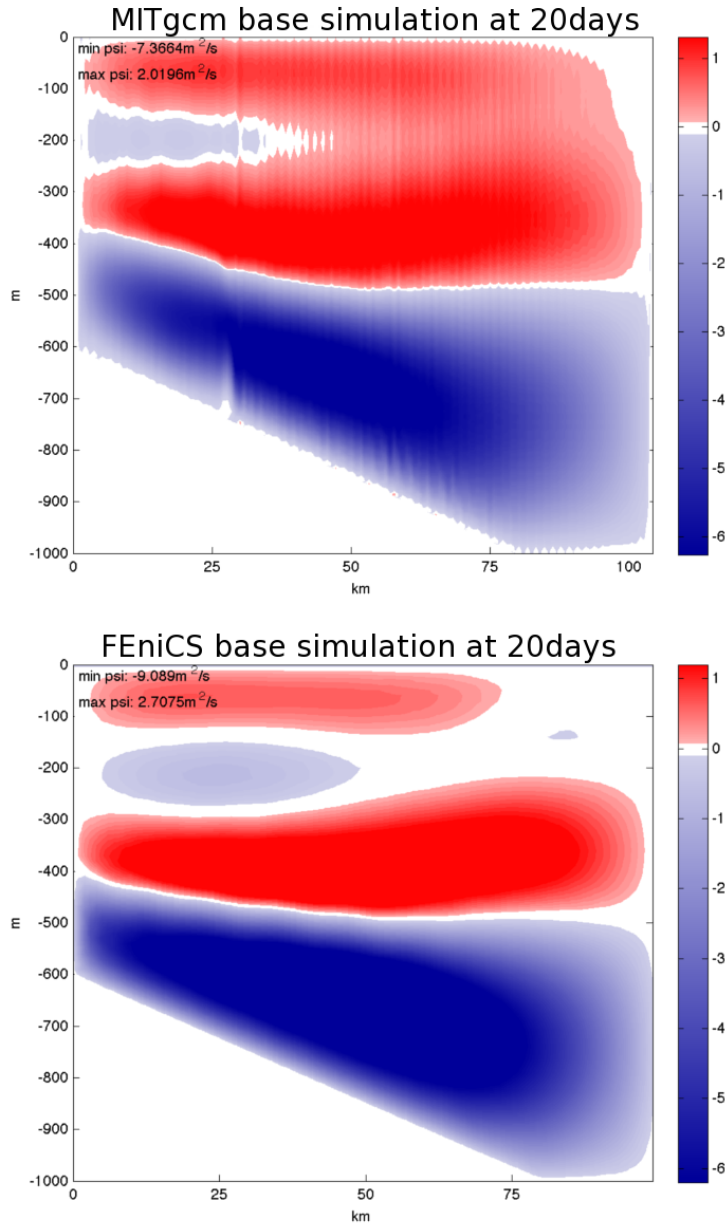


Figure 5.1: Shows streamfunction snapshots at 20 days with the base case parameterization, as simulated by both the MITgcm and FEniCS. The bottom cell is extremely similar qualitatively between the two simulations. The upper cells show some differences that can be attributed to the temporal variability of the upper cells.

Model	Rise (m)	$\kappa_{max}$ $m^2/s$	$\delta$ (m)	$\psi_{min}$ $m^2/s$
MITgcm	400	0.1	178	-7.366
FEniCS	400	0.1	170	-9.089
MITgcm	400	<b>0.05</b>	138	-4.822
FEniCS	400	<b>0.05</b>	133	-6.138
MITgcm	400	<b>0.2</b>	218	-9.835
FEniCS	400	<b>0.2</b>	205	-11.90
MITgcm	<b>200</b>	0.1	134	-8.124
FEniCS	<b>200</b>	0.1	153	-9.607
MITgcm	<b>600</b>	0.1	158	-7.760
FEniCS	<b>600</b>	0.1	192	-8.555

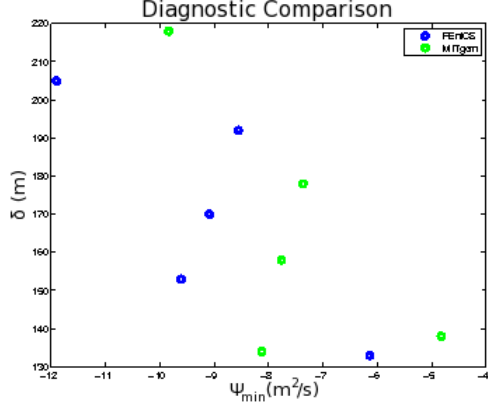


Table 5.1: Diagnostics from simulations alternating between models. The second and third column list the imposed parameters as they were varied for these simulations. Each pair of lines run the same simulation in different models starting with the base case. The differences from base parameterization are in bold highlight the order of change: diffusivity is halved and doubled, then the rise of topography is decreased and increased by 200m. The diagnostics are plotted together with blue circles for FEniCS and green for the MITgcm. The FEniCS-MITgcm pairings for simulations is easily visible.

very similar between models. The values of  $\psi_{min}$  are also consistent with the base case, hovering around a 20% difference throughout. To make a more visual case for these similarities a scatter plot shows  $\delta$  versus  $\psi_{min}$  in the Figure of 5.1. With blue circles representing the FEniCS simulations and green for the MITgcm, the pairings for the same setup parameters are very clear. The center six dots representing the simulations with base diffusivity,  $\kappa_{max} = 0.1 m^2/s$ , appear systematically shifted. In comparison with both the high and low diffusive cases, there is a greater difference but still distinct pairing between MITgcm and FEniCS simulations.

Since the ratio of velocities in the vertical and horizontal is similar to the aspect ratio of the domain, it follows that the majority of the streamfunction magnitude is actually from the horizontal flow. The roughness seen in the MITgcm runs, which in

extreme cases such as low vertical viscosity actually formed into vertical cells (bottom of Figure 3.7, p.43), works against the development of the horizontal component. Though this can account for some of the difference in  $\psi_{min}$ , a different explanation, relying on trends that will be described in the following section, can explain the discrepancies in both diagnostics. Increases in diffusion will both strengthen the up-canyon flux of the lower cell and increase its height, thus numerical diffusion in the FEniCS model being greater than that of the MITgcm is a likely component of the differences seen in the scatter plot.

Even with differences such as that just described, the comparison supports and extends the assertion that the FEniCS model and MITgcm are not only showing similar results in one simulation but are representative of the same internal dynamics. This allows for the already proposed direction of only referencing one model, the MITgcm, for support while thoroughly reporting results from the FEniCS model.

## 5.2 Model Diagnostics

The simulations from this point onward are primarily FEniCS results, as just mentioned, for consistency in presentation. As functional dependencies are explored, three parameters are used in determining two diagnostics. The maximum vertical-diffusion,  $\kappa_{max}$ , is set at every point on the boundary and decays exponential in the vertical, as stated previously. Taking advantage of this and of the horizontal diffusion being constant, diffusion will be used interchangeably with the ‘vertical diffusion maximum.’ The second parameter varied is the slope of the topography which is used analogously to the term *rise*. This is not ambiguous as the portion of the domain with sloping topography is always the same 80km and so  $slope = \frac{rise}{80000}$ . Finally, the influence of the slope length is investigate by scaling the entire domain and thus keeping the aspect ratio constant.

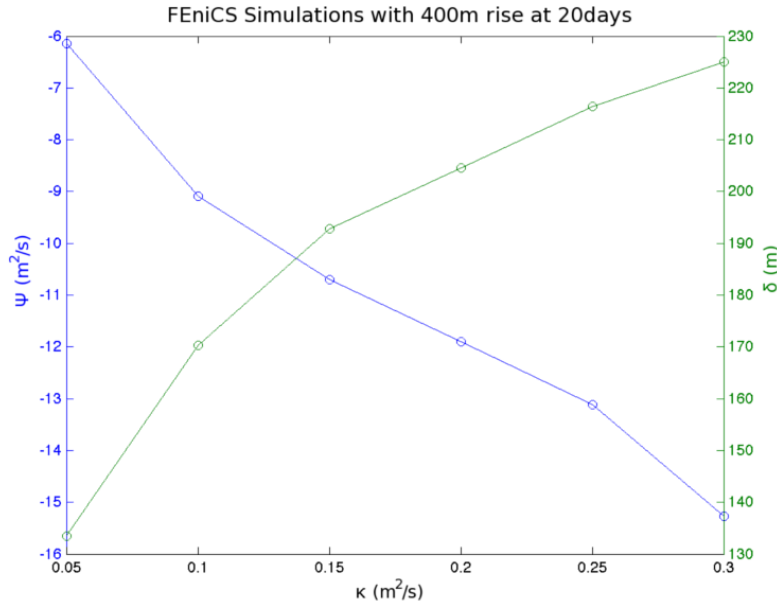


Figure 5.2: The effects of diffusion when the rise in topography is held constant at 400m. The diagnostics were calculated from six simulations all after 20 days of spin-up. The blue curve shows the dependence of the streamfunction magnitude is approximately linear. The green curve shows the influence on the layer height diminishes as diffusivity increases through the range.

### 5.2.1 Diffusion

The maximum vertical diffusivity most directly ties in to previous studies and is therefore the first parameter of focus. A glimpse at the dependency of the two diagnostics is shown in Figure 5.2. The simulations are filtered to only those with a rise of 400m, which are then examined at the 20 day timestep. An expected monotonic trend for  $\psi_{min}$ , in blue, shows the maximum diffusivity of the bottom cell increases in strength (becomes more negative) when  $\kappa_{min}$  is increased. The actual data are marked with open circles for the six simulations over the full range of explored diffusivities,  $0.05m^2/s - 0.3m^2/s$ . With y-axis on the right, the green line shows, to zeroth order, that the layer height grows as the diffusivity increases.

The linear trend shown in Figure 5.2 generalizes to other slopes as well. Fig-

ure 5.3 shows the previous streamfunction data plus the curves of two more slopes. The blue solid lines are the base case, rise of 400m, while the red have an increased slope, rise of 500m, and the green have a decreased slope, rise of 300m. The solid lines are simply piecewise linear connections between the simulation data, indicated by circles. The plot on the left is from the determined 20 day spin up, while the simulations are plotted again in the same way on the right after 30 total days of simulation. The dotted lines show linear regressions for each slope-series, both plots having fits from the 20day data. The fits of these timeseries reveal more than simply a good approximation: the  $r^2$  value increases with the slope. While the later data, on the right, do not align with the slopes found they are still linear and do not contradict the type fit. As listed in the figure legend, the shallow slope has a fit of 0.95 while the steepest slope has more than 99% of its value predicted by a line. Caution must be taken with these linear regressions, even having strong fits, since they do not converge to the expected limiting solutions. In the lower limit of diffusivity, ie  $\kappa = 0$ , the model has no forcing and the streamfunction must disappear entirely. While the intercepts of the lines plotted (-5.75, -5.14, and -2.23  $m^2/s$  for 3, 4 and 500m rise) are decreasing with increased slope, are always distinct from zero.

To tie this into previous results,  $\psi_{min}$  can be thought of as up-canyon mass flux. The streamfunction implicitly represents the integral of velocities, and the model was based on the assumption its two-dimensional domain is representative of an average over the width of the flow,  $w_f$ . Thus it is directly proportional to an estimate for flux,  $Q$ ,

$$Q \approx \psi_{min} w_f.$$

This proportionality allows direct comparison with established flux parameterizations such as those in Wunsch [1970]. A linearization for flux was found relating it to diffusion and the angle of slope,  $\alpha$ ,

$$Q = \cot(\alpha)\kappa. \quad (5.1)$$

His linearization is justified while  $\sin(\alpha) < Ra^{-1/4}$  which translates into a rise of just under 100, agreeing both with the trend seen and the decrease in fit as the

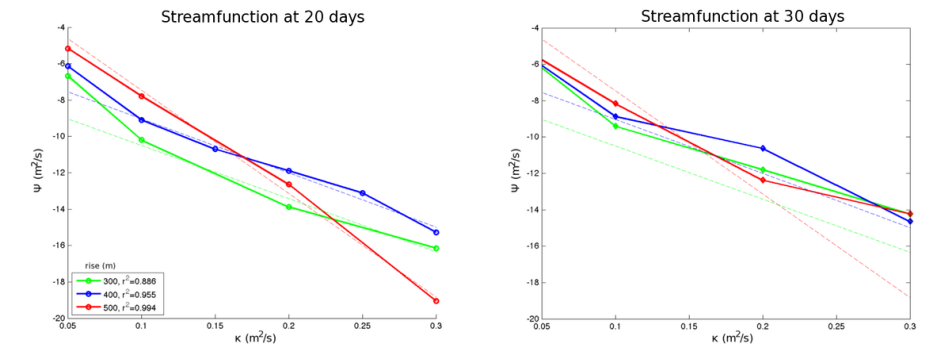


Figure 5.3: The trend of  $\psi_{min}$  as it is dependent on maximum diffusivity. The blue as before is the base slope, equivalent to a rise of 400m. The red is at 500m and the green at 300m. The simulations are marked with circles and the left plot is data at the 20day spin-up. Solid lines show piecewise linear connections between simulations, linear regressions are shown with dotted lines. The  $r^2$  values listed in the legend show increasing the slope increases the quality of the fits on  $\kappa$ . Shown on the right are the same series but with ten more days of simulation, and the linear fits from the 20day regressions.

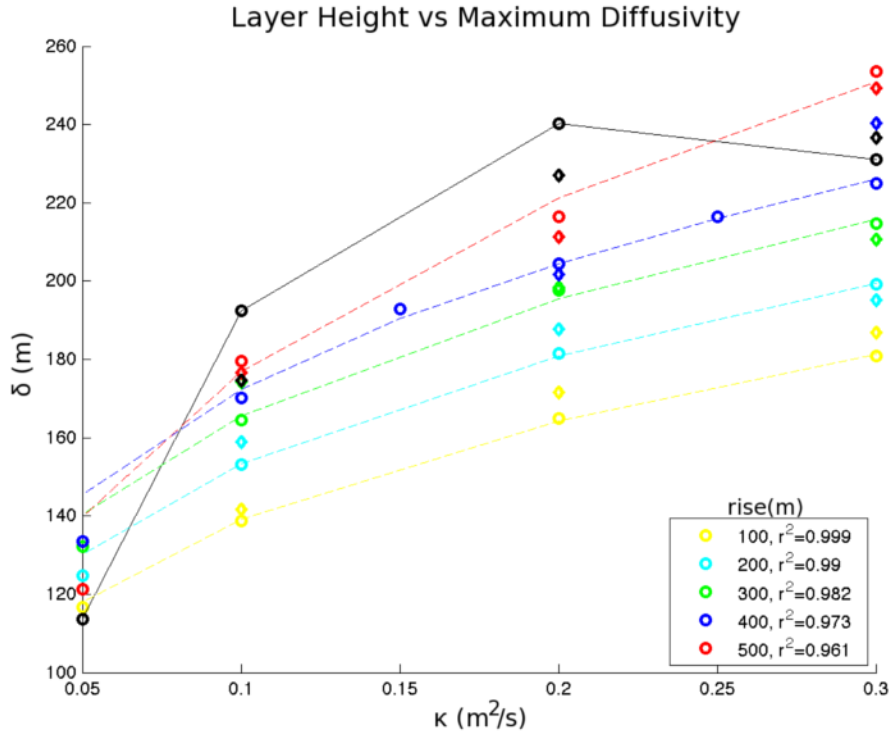


Figure 5.4: The thickness of the layer of upslope flow as a function of maximum diffusivity. The slopes simulated are identified by color. Circles indicate data taken at 20 days and diamonds are from 30 days. A monotonic trend is seen across all simulation for all slopes beside largest, 600m rise. The dotted lines show good fits of the 20 day data to a  $\kappa^{-1/4}$  type power-law.

numerical simulations approach the cutoff for linearization.

There are also estimates on boundary layer thickness with related dependencies. Phillips *et al.* [1986], in their original physical models, predict such a boundary layer flow using the approximation

$$\delta \approx \left( \frac{\nu \kappa}{N^2 \cos^2(\alpha)} \right)^{1/4}. \quad (5.2)$$

This approximation is directly compatible with the decision to follow layer height instead of cell height. Figure 5.4 shows the layer height as related to  $\kappa$  for the range of simulated slopes. The simulations are marked by circles of color corresponding to the slope. The layer height,  $\delta$ , increases in loose agreement with the form from

Equation 5.2. To show the agreement, the least squares fit for curves this form are plotted as well with dashed lines. The large divergence seen from this theory occurs at the single simulation at highest diffusion and slope approaching the range where boundary effects are visibly observed. Again data from ten further days of simulation are plotted, with diamonds, and support that the trends at 20 days are not unique.

Even omitting the simulation with  $\kappa = 0.3m^2/s$  does not fix this divergence from theory though. Using the model values for turbulent diffusion and viscosity, Equation 5.2 gives a boundary layer height on the order of 1-10m, not at all the 1-200 seen across simulations. The disagreement in predicting even the order of the layer thickness serves as a reminder that Equation 5.2 was intended for true boundary layers, which would not be resolved within this model, and not the observed bottom-layer being studied. The equation was used as a basis for the fit, allowing for the possibility that the underlying form itself could be governing these layers as well. It should also be noted that although the fits are seemingly good in terms of  $r^2$  values, as shown in the figure legend, similarly strong values are found when regressing to functions  $\kappa^{\frac{1}{n}}$  for all tested integers from 3 to 12. This is actually better than expected as physical models see divergence from this theory starting around  $4^\circ$  [Peacock *et al.*, 2004], at least in velocities.

### 5.2.2 Topography

The dependence on sloping topography, assumed from the beginning, has departed from the range of established theory, even as loosely related as (5.2). Continuing with a focus now on slope angle, the diagnostics will be examined directly in terms of this independent variable. Looking at the effect on streamfunction first, as before, does not give the simple picture for which Eq. 5.1 might lead one to hope. Translating from angles to rise using small angle approximation leads to

$$Q = \kappa \cot(\alpha) \approx \frac{\kappa}{\alpha} = \kappa \frac{80000}{rise}.$$

This is far simpler than what is found from simulations, as can be seen in Figure 5.5. This figure shows the dependence of  $\psi_{min}$  on topographic rise, calculated by the

simulations marked as usual with open circles. Unlike previous figures, color now distinguishes the maximum diffusivity in the simulation run. Not only is a local minimum seen between 200 and 300m rise but it is consistent across changes in diffusivity.

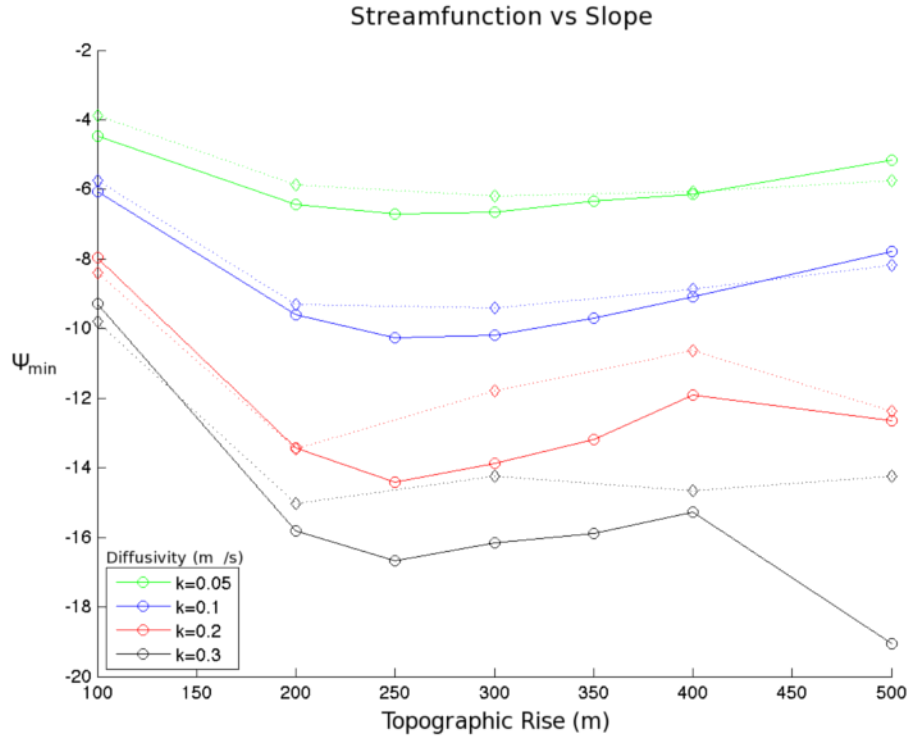


Figure 5.5: Minimum streamfunction as a function of slope. The contours are the four main diffusivities used and are plotted as usual, with circles indicating the diagnostics of simulations calculated at 20 days. All four show a local minimum at a topographic rise between 200 and 300m. The stronger diffusivities,  $\kappa = 0.2 \text{ m}^2/\text{s}$  and  $0.3 \text{ m}^2/\text{s}$  indicate slightly weakening streamfunction before strengthening again for rises above 400m. Again data from 30 days has been added with diamonds, connected with dotted lines, that shows similar behavior with the possible exception of a simulation at the highest diffusivity.

Especially when looking at the more diffusive cases, the figure splits slopes into two distinct regions. The first region, which consists of the shallow slopes up to

and including 400m rise, contains the mentioned local minimum. The magnitude of  $\psi_{min}$  extrema does not appear to be dependent on slope and are aligned at about 250 rise. The transition back to a strengthening layer, for increases in slope, is less clear as the local maxima for these series occur at different slopes. For the highly diffusive case,  $\kappa = 0.3m^2/s$ , the streamfunction is strengthening rapidly as rise increases from 400m to 500m. In contrast, the minimum streamfunction in the base series and low diffusion series continues to weaken through at least a rise of 500m. Several additional runs at rises of 600m and 700m were considered to check that the trends seen from 400 to 500m were not simply outliers.

The diamonds, connected by dotted lines on Figure 5.5, show the minimum streamfunction from after 30 days of simulation. These data show the most disagreement with the trends seen from the 20 day spinup. The black line of highest diffusivity no longer has a single local minimum at shallow slopes, which can be accounted for by a single data point. Even so, error of less than 10% would be enough to strengthen the streamfunction of the 300m and  $0.3m^2/s$  simulation and correct the discrepancy. With this being the largest qualitative difference observed between the two timesteps, the 30 day data is still taken to support that there is nothing unique about results seen from at the 20 day spinup.

While obtaining a complex equation to explain all the intricacies seen would be useful, it would require many more simulations than were run. Even if possible, attention should be drawn to the more realistic of the cases, for simpler but perhaps equally as useful observations. The lowest simulated diffusivity,  $\kappa_{max} = 0.05m^2/s$  is still large when considering turbulent diffusivity even in what is assumed an enhanced layer near the ocean floor. While this case, the green line from Figure 5.5, does exhibit the same shape as the others, it has much smaller variability. To show this more clearly,  $\psi_{min}$  has been normalized and plotted again, Figure 5.6. For each series of  $\kappa_{max}$  the mean and standard deviation were calculated and used to shift and weight the data within the series. The importance of diffusivity in determining the streamfunction magnitude is reemphasized by this, as it was already shown by the investigation into that parameter (Figure 5.3).

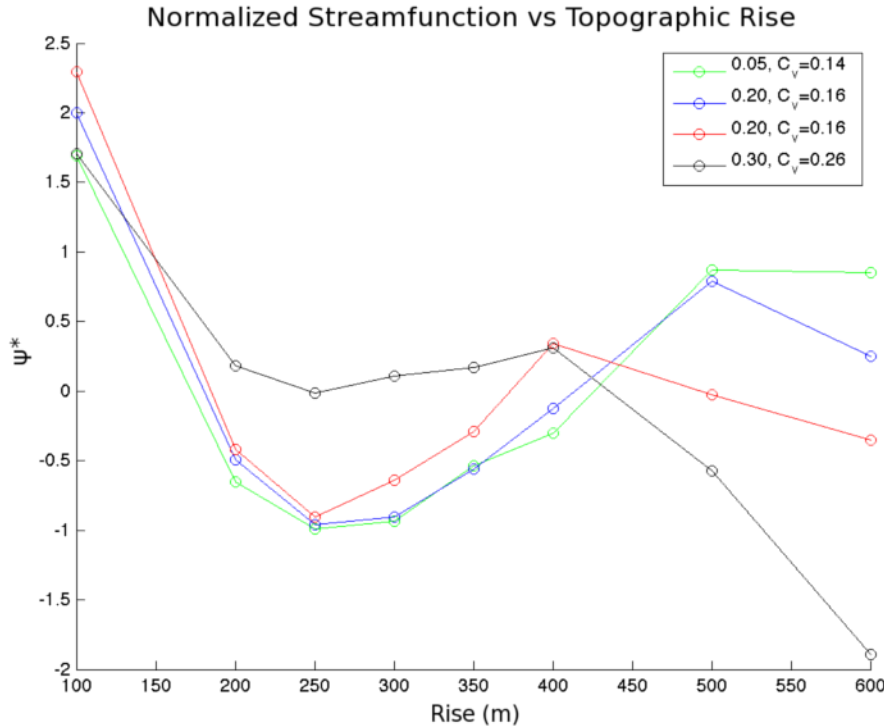


Figure 5.6: A normalization of  $\psi_{min}$  plotted against the rise of the topography. The colors separate the data into four series based on  $\kappa_{max}$  and were normalized as such. The  $\kappa_{max}$ -series have each been shifted by their means and then weighted by the standard deviation to reveal the similarity between the curves, independent of scale. The coefficient of variance for each series is listed as also show a clearly decreasing trend with diffusivity.

This presentation of similarities sets up data to allow use of the coefficient of variance, a mean-weighted standard deviation. As can be seen from the legend, the percent of variance improves with decrease in diffusivity. The highest diffusive case varies by 26% of its mean value compared with 16, 16 and then only 14% for decreasing  $\kappa_{max}$  values of 0.2, 0.1, and  $0.05\text{m}^2/\text{s}$ . The trend shown, assuming it continues, would indicate even less variability at the more likely diffusivities one or two orders of magnitude lower.

The relationship between rise and layer height is not nearly as complex when

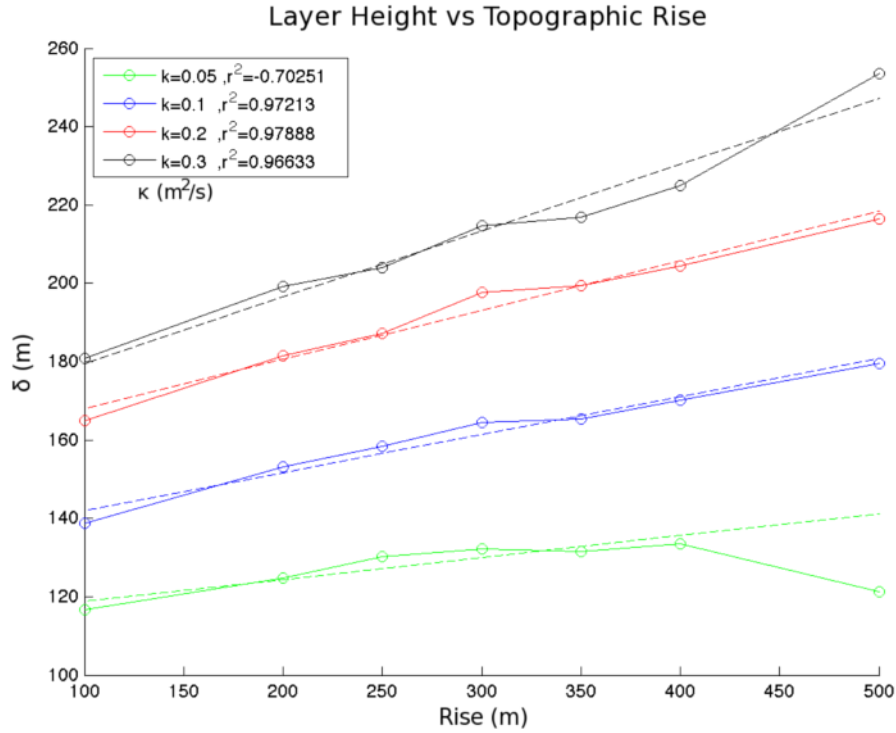


Figure 5.7: Layer thickness as a function of slope. Diffusivities are indicated by color across the whole array of slope angles. A linear trend was found for each and plotted with a dashed line. While three cases are approximately linear, the weak diffusivity not on shows a different form but even has a smaller layer at the steepest slope.

limited to simulations with rise of less than 600m. In another case where all but one simulation follows a trend, Figure 5.7 displays how the layer height responds to changes in topographic height. The now standard forms are used in plotting; circled data are connected piecewise linearly with solid lines colored in accordance with diffusivity. A linear regression is calculated for each case and plotted with a dashed line, and a goodness of fit is presented in the legend.

The trend to zeroth order is simply increasing layer thickness in response to increases in slope angle. Even though the approximations from literature break down in this range, as warned again by Peacock *et al.* [2004], no leaps of faith

are required to understand the correlation. Though a first connection would be that in satisfying the no-flux condition at the boundary, shallower (non-zero) slopes require steeper gradients, this does not imply the scale on which those gradients exist. An argument based on conservation of momentum can be made making use of the MITgcm's ability to resolve the dynamics with its z-grid representation of topography. Simplifying beyond the shaved cells actually used, the topography is approximated by steps, and the height of the steps change analogously to slope. To get any fluid up and over a step requires vertical motion. For the upslope velocity to remain constant the vertical component must increase in magnitude as the step grows, which is nothing more than the trigonometric relation based on the angle. The forces opposing the upward motion of this parcel are limited to viscosity and gravity, both of which are constant. At this point the argument reduces to a problem analogous to inertia and the larger velocities must make their way farther up before being overcome. This inertial description more aptly connects slope to the layer thickness than the consideration of gradient steepness. A key assumption here is that the upslope flow remains constant, or increases, as the slope increases. While justifying the existence of the vertical flow relates back to the original force balance explanation (Figure 2.2, p. 18), the assumption has been shown to be true by similar physical experiments that found the velocity has a local maximum at around  $3^\circ$  [Peacock *et al.*, 2004].

### 5.2.3 Slope Length

When the MITgcm domain was altered to allow for the base slope, 400m rise, to be longer or shorter than the normal 80km length, there was an influence on the strength of the bottom cell, Figures 3.6a-c. The nondimensionalization of the FEniCS model allows a different approach to investigating this parameter without having to generate completely new meshes. While varying the slope length, it was decided to keep as many nondimensional numbers constant as possible, specifically  $A_r = 0.01$ . This constant means a percentage change in slope length has a proportional effect on the domain height as well, but only changes the equations through

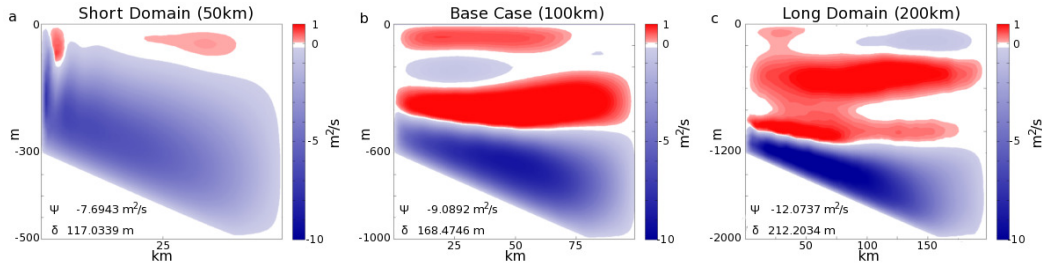


Figure 5.8: Three streamfunction plots with different size domains. The base case streamfunction is shown in the center, b. The case to the left and right have a smaller and larger  $Ra$  respectively, by a factor of 8, so that the length scales are both halved and doubled. The small case, a, shows a definite decrease in  $\psi_{min}$  while only having one large cell. While the large domain, c, does show even more complexity than usual in the extra room above topography, the most significant aspect is the more intense upward flow.

the Rayleigh number ( $Ra \propto H^3$ ). Using these decisions, many of the simulations were redone in a domain both half and double the base size.

Comparison of these three domain sizes can be seen in Figure 5.8, making use of the streamfunction at 20 days. The central plot here is the standard base case, which has a domain length of 100km and thus a height of 1km. Looking first at the short domain, it is seen that the dynamics stretch nearly to the top of the region. The available height in this simulation ranges from 300m at the left boundary to 500m at the right, so even though  $\delta$ , at 117m, is less than the base case, it is still possibly influenced by the top boundary. For this reason the layer height will not be considered, but the magnitude of  $\psi_{min}$  will still be examined. In the doubled domain there is an increase in strength as expected, giving a monotonic trend between all three, -7.69, -9.09, and  $-12.07 \text{ m}^2/\text{s}$  for lengths of 50km, 100km and 200km. The upper cell dynamics of the large domain should also be noted to have extra cells. This is uncorrelated with the bottom cell strength, which is an assumption that while partially supported already when examining spinup times, 4.1 (p. 4.1), will be examined again in terms of other variables later.

Simulations at the three domain sizes already displayed were done over the

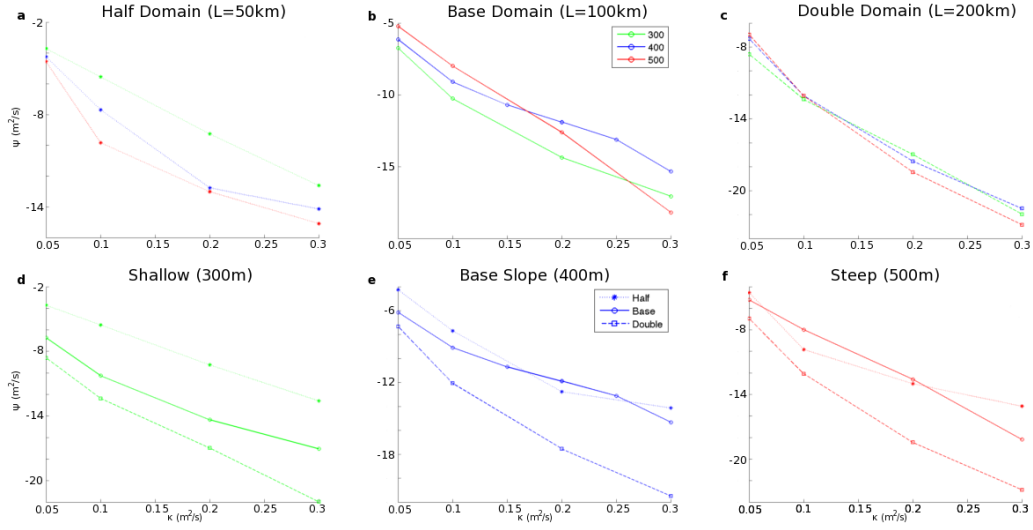


Figure 5.9: Plots sampling data from simulations including multiple domain sizes. The simulations sampled are at the three domain sizes (50, 100, and 200km domain lengths), and are at three slope angles (300, 400, and 500m rise) All plots are diffusion versus  $\psi_{min}$  at 20days, with color indicating slope and line-type indicating the domain size. The center top, b, is the same as Figure 5.3 as solid lines indicate base size. The dotted lines in a are indicative of the small domain and the dashed to the right are the large. The second row groups slopes together. The first row together shows that multiplying the length of space has more effect then small changes in the slope, but the smaller domains in e. and f. show that the slope's value is still a significant factor.

range of slopes and diffusivities. The streamfunction-minima diagnostic is displayed against the maximum diffusivity in Figure 5.9, partitioned in several ways. Within the figure, domain sizes are differentiated by the type of line; the normal size is a solid line, the small domain is dotted (5.9a) and the large domain is dashed (5.9c). With all three groups, each showing series at slopes equivalent to rise of 300, 400, and 500m, it can be seen that the strength of the bottom cell clusters well and with increasing tightness as domain size increases. The small domain has the series clearly separated by slope, and though the values are smaller, the difference in magnitude scale between these first three plots is not large.

The top row of this figure, 5.9b, shows how changing the slope length influences the trend already seen between  $\psi_{min}$  and diffusivity. The center plot of this row, b, is at the normal domain size and just repeats Figure 5.3. The spread in the three series of this line is the variability at a given diffusivity, which is affected by the slope length. While the series are much closer together in the long slope case, Figure 5.9c, it should also be noted that the magnitudes of  $\psi_{min}$  being presented are more negative. Comparing these to the short slope, a, supports both trends. Increasing the length of the sloping region will decrease the variability of  $\psi_{min}$  at a given diffusivity while also increasing the flux of the upslope flow.

The figure, 5.9, does not say domain size is more important than slope as a first glance might indicate, since the changes are not directly comparable. Size of the domain increases by multiples of two from left to right, and the slope change is simply increments of 100m additional rise for each 80km of length. The second row can be used as a reminder of the difference and shows the slope angle's importance, since at larger slopes the domains cannot confidently be distinguished. The shallow slope, d, shows a large influence from domain length, with the strength roughly doubling when the domain is increased by a factor of four, between dotted to dashed series. In this plot, the base domain already shows 65% of the increase, well over half as should be expected due to diminishing significance of changes in size. For the slopes steeper than 300m rise, and consequently having larger magnitudes of  $\psi_{min}$ , the percent increase is smaller for the same change in slope length. The base domain is more intense than the half domain when averaged over the whole series, but the difference is well within a band of 10% error. The 200km domain shows an increase of over 50% in the base slope and still has 42% in the steep case. The trend described with dependent on slope angle is an important one. Together these imply that increasing slope weakens the influence on, and decreases the variability seen in,  $\psi_{min}$  with respect to slope length.

## 5.3 Further Directions

As with any complex research, issues arise during study that cannot be overlooked, though they can vary wildly in their relevance to the main focus of the study. At the very least, it must be determined if any such issues effect the phenomena being researched or possibly even overwhelm it. A couple such topics demanding discussion will be presented here. Starting with the one of lesser significance to the direction of study but no less interesting, the presence of cells in the upper domain will be discussed. Finally an additional direction is taken, as the model is expanded to make use of a periodic domain.

### 5.3.1 Upper Cells

An avenue of investigation tangent to that of the dynamics of the lower cell appeared early on in simulation comparison, and concerns the cells in the interior and top of the domain. Mainly ignored before, they should be described and their form investigated. The number of cells in most of the simulations is either two or four, while cases with very weak and shallow slope may have more. More complex than simply having two or four times as many domain-wide cells, there is significant horizontal dependence to their shape. Therefore, rather than create and explain enough parameters to adequately describe the common occurrences, an array of snapshots is used, Figure 5.10. This array contains some of the direct model output that was used to create the diagnostics analyzed. The model's variable streamfunction is displayed at the 20 day mark for each of fifteen simulations. The maximum diffusivity is constant within columns; 0.05, 0.1 and 0.2  $m^2/s$  from left to right. Topographic rise is constant across rows; 200, 300, 400, 500, and 600m rise from top to bottom. The plot shading indicates the magnitude of streamfunction and has a consistent scale between simulations; blues are negative values with darkest at  $-12m^2/s$ , white is a band around zero, and reds are positive streamfunction with darkest at  $4m^2/s$ .

The top row, with topographic rise of 100m, consistently shows three upper cells. As an example of the extra complexity the upper negative (blue) cell appears most

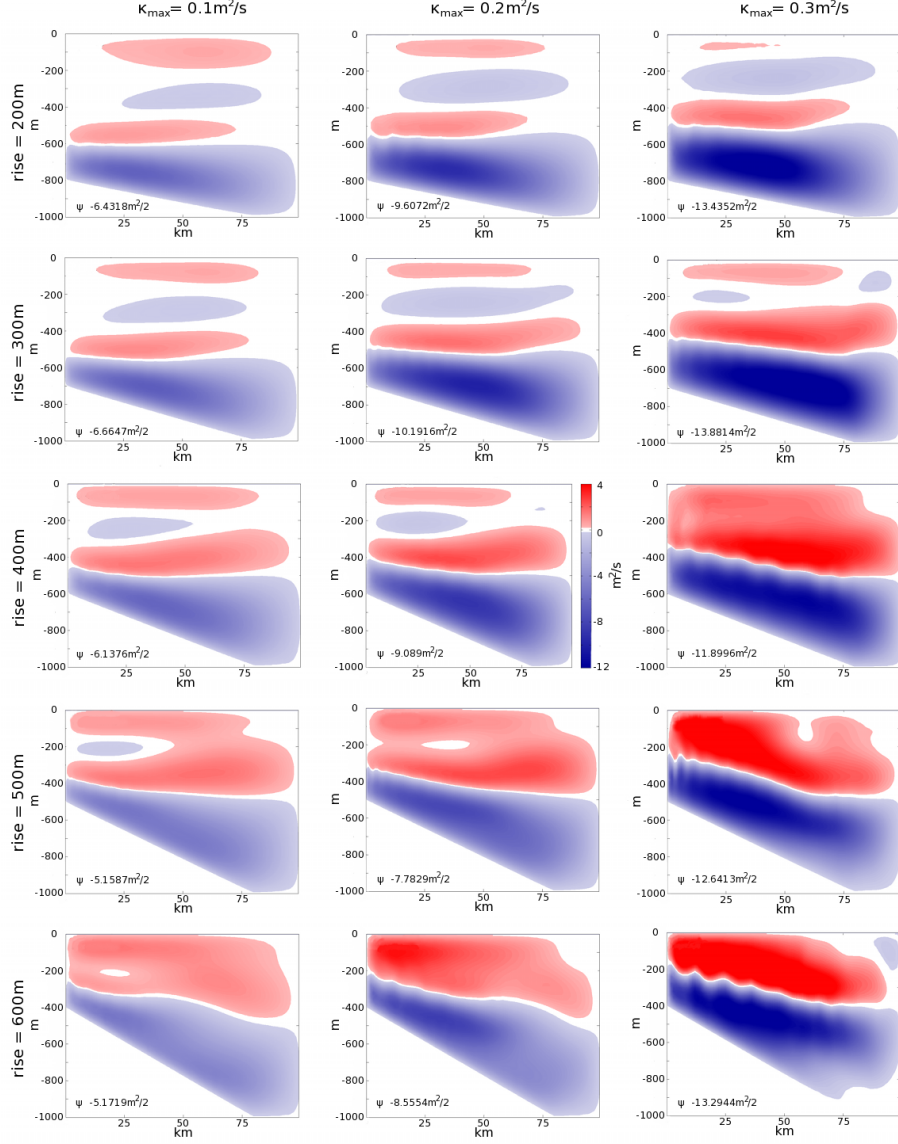


Figure 5.10: A table of streamfunction snapshots all taken at 20days, from the FEniCS model. The rows are each of a different topography with the rise increasing down the column: 200, 300, 400, 500, and 600m. The columns show diffusivities of  $\kappa_{max} = 0.1, 0.2$ , and  $0.3\text{m}^2/\text{s}$  from left to right. Together these show some of the transience of the upper cells, and also that increases in either slope or diffusivity can suppress the formation of additional cells.

dominant and if judged only from these three snapshots seems to be overpowering the topmost red cell. In almost all other cases it is the extra red cells that dominate, increasing in strength and size until only the two cell-form remains that is common in the high slope cases like rise of 500 and 600m shown in the bottom two rows.

The previous description and inclusion of  $\psi_{min}$  for each plot of Figure 5.10 should not be taken to mean that the strength of the bottom cell is directly related to the formation of cells in the upper layer. The tendency to have only two cells correlates more with increasing slope than to strengthening streamfunction minima. This can be seen by first noting the 600m case at  $0.05m^2/s$ , bottom left corner, has  $\psi_{min} = -5.2m^2/s$  and a ‘hole’ in its dominant upper cell. This is actually weaker than the 100m rise case at  $0.1m^2/s$ , top middle snapshot, which has four distinct cells and a  $\psi_{min}$  approaching  $-10m^2/s$ .

While  $\kappa_{max}$  does have some affect on the number of cells, the slope appears to have multiple paths of influence to these cells. It has already been seen that increasing the topographic rise increases the layer height, and it seems natural this progress upward to limit the space for upper cells. An even more direct path in which increasing slope limits the space is due to the finite height of the model. Increasing slope effectively shrinks the vertical height over part of the domain. Yet a third way is indirectly changing the diffusivity. Since  $\kappa$  is specified on the bottom boundary and then decays upward, increasing slope can be thought of as moving the bottom edge up which drags that intensified mixing region with it. For a given interior point, this creates the same situation, in terms of physics, as if  $\kappa_{max}$  had been increased, and the vertical shear cannot develop.

Interesting physics is behind these variations without doubt, and some of the explanations just presented are part of the dynamics of the bottom layer. Even so, the upper cells do not appear to be affecting the focus of the study. Perhaps the easiest feature to look for within these plots is the local minimum of  $\psi_{min}$  that so consistently occurred between cases of 200 and 300m rise, Figure 5.5. The trend should be between the first and second row of this figure 5.10, yet nothing significant is visible in terms of these upper cells. Even in the case of  $\kappa_{max} = 0.2$  and rise=400m

, the middle right snapshot, the upper cells have finally merged yet this aligns with a local maximum (weakest) for  $\psi_{min}$ .

### 5.3.2 Periodic Domain

A logical next step from the closed domain simulations presented so far is creating a channel-like domain with periodic boundaries. Periodicity will allow similar study without having to deal with many of the types of boundary effects included with solid walls. However, to allow for such boundaries in a consistent way, several changes need to be made to the model. The biggest needed difference is that the left and right boundary need to be made equivalent before they can be identified numerically as two sides of the same edge. The concept behind the extension used here was simple mirroring. While the choice of which boundary to mirror is essentially arbitrary, it was decided to extend the domain on the left boundary at the peak creating ridge-type domains.

As a first check, a simulation was run with the new ridge domain, while still incorporating closed boundaries. When run with the same slope on both sides of the ridge, even opening the boundaries is still a trivial case because of the methods of images. The idea behind this method is actually the model expansion in reverse. The method of images considers a virtual extension across a boundary to solve for the single side [Vallis, 2006]. The virtual image consists of a reflection of all the forces as well as the state of the system. The symmetry created the original plus this virtual image is often easier to solve analytically than the original portion alone. The model from the previous sections solved for a single side, while the periodic domain creates exactly the mirrored area the images would assume. Since no new forces exist to break the symmetry, the two sides of the simulation are the same as is seen remarkably well in the mirrored base case, Figure 5.11. This plot is of the streamfunction after the usual 20 days have elapsed. The only differences between half of this figure and the original, as seen before in Figure 5.1, are a few ten-thousandths difference in  $\psi_{min}$  and a different aspect ratio of the plot to display double the domain width.

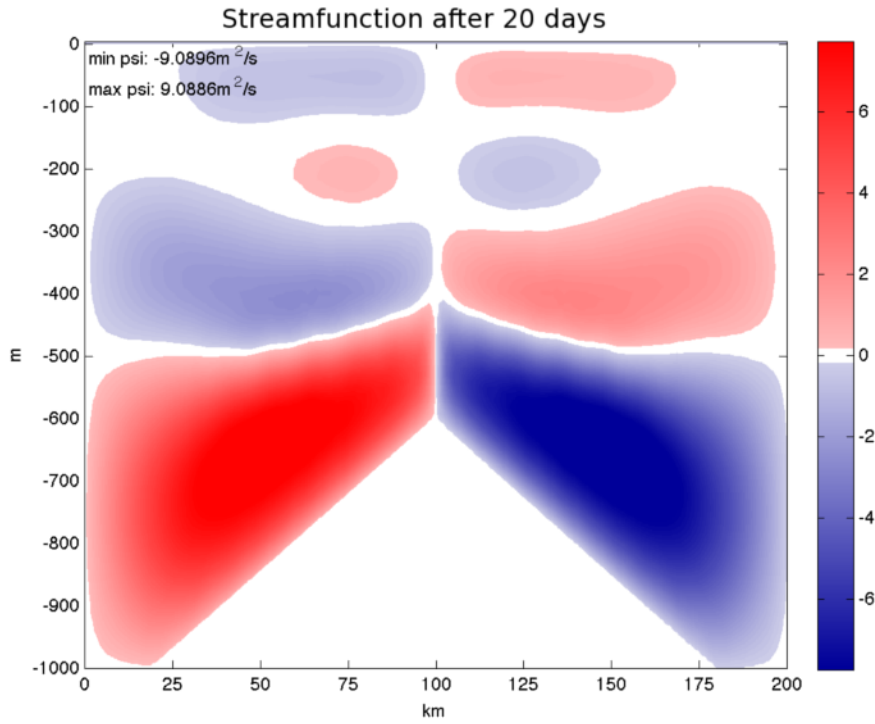


Figure 5.11: A snapshot of streamfunction after 20 days in a periodic ridge-type domain. This run is the normal base parameters, simply extended into a mirror image allowing periodicity in the horizontal. In this setup, the symmetry of the topography and initialization remain unbroken and evolve just as the slope-type case.

In order to yield new results the symmetry must be broken. The method chosen for creating an asymmetry was to have the ridge sides differ in slope angle. Several choices were made in an attempt to allow easy comparison with the closed ‘slope-type’ simulations. With this purpose the right side’s slope was kept at the original 80km length while the other side would be shortened to generate the desired slope. The method of only shortening the left slope ensures that there is always a region of maximum depth, and more strictly that the slope always has at least the 20km plain. As some of the power of symmetry has already been shown, mirroring any of the new domains is redundant and so skipped. An additional convenience taken was that

the models were setup so that one side or the other contains the slope of our base case, either on the right or the left flank. In the case where the right flank contains the slope of the base case, nothing changes on this half of the domain compared to the base setup (Figure of 3.1. The 80km region allows the full 400m rise to the peak. The flank opposite will have a steeper slope and so reach the maximum 1km depth in less than 80km. This description points out that the term rise is no longer analogous to slope as it was in the smaller closed domain. To work around this the term will now be specified as ‘equivalent rise’ or the amount topography would rise if given a full 80km. So when the left flank has an equivalent rise of 400m, it will be adjusted to meet the peak determined by the slope on the right side and also be shortened to stop at the maximum depth. Examples of this with a right-flank rise of 200 and 300m can be seen on the right of Figure 5.12 (c&d).

The conventions used until now concerning the diagnostic of streamfunction *minimum* must also be addressed. The purpose of  $\psi_{min}$  was to indicate the strength of the bottom cell and also be proxy for the flux of this upslope flowing layer. With a single slope the sign was consistent, but with two slopes of opposite sign  $\psi_{min}$  is not always appropriate. The extension is straightforward but should be made explicitly, the magnitude of the extrema of  $\psi$  will be the actual diagnostic where minimum and maximum will indicate which side of the ridge is being discussed, if necessary.

All other parameterizations remain the same, including that a single value of  $\kappa$  specifies the vertical diffusivity at every point on the topography no matter which side of the peak. The peak however introduces two discontinuities in the diffusivity profile. Previously, there was a corner caused by single point transition between the slope and the plain at the end of the domain. Now in addition to the corner like this for the other side of the ridge, there is also one at the peak which is even sharper due to the slopes being of opposite sign. To compensate for some of these effects, the FEniCS model took advantage of its already non-uniform mesh and was refined locally around this protrusion.

With the new model domain in place, simulations develop several observable

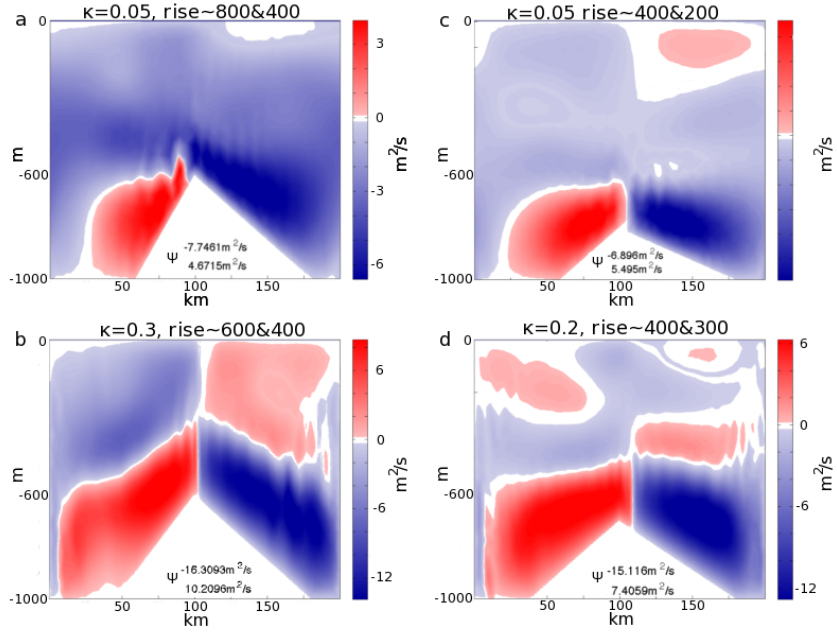


Figure 5.12: Streamfunction snapshots from four periodic domain simulations. These plots are all at the 20 day mark, allowing for the normal spin-up, and have the color scheme used in previous streamfunction plots. They have four separate values for limits on colors adapted to the individual snapshots extrema. The periodic simulations show more waves at the interface than the slope-type models even with their meshes refined at the center. The right-slope has a stronger bottom cell on all of them but there are cases of the right and left cell being the one to flow over the peak as well as cases where they appear to meet at the peak.

differences. The most qualitatively noticeable one is the upper cells. Four cases are displayed in Figure 5.12 to demonstrate this and point out several other significant points. The models shown include cases between which vertical cells vary in number and also the cell dominating the peak changes in sign. The plots are labeled with three parameters; the maximum diffusivity which is equal on both flanks of the ridge, the rise the left slope angle would result in over 80km, and the actual rise (for the right flank) as was used in the closed simulation results. They were ordered so the two on the left would include a portion of topography identical to the base case and increasing diffusivity downward; the two on the right having different ridge configurations both including an equivalent rise of the base 400m over their left-flanks.

The easiest to compare with previous results is Figure 5.12d, as it is close to a mirrored configuration of the original base case. The ratio of slopes determines the percentage of the standard 80km, so this case of 300 and 400 has a left-flank extending 60km, which is more than the other simulations. Because of this, much of the observed dynamics are similar as well, if the waves at cell interfaces being more prevalent is not taken into account. Looking at the right side reveals roughly four cells in the vertical. The magnitude of this side is actually stronger than was seen before,  $-15.1 m^2/s$  compared to  $-13.9 m^2/s$  in the slope case of 300m rise and  $\kappa = 0.2 m^2/s$ , which was part of Figure 5.10. The left side with the steeper yet shorter slope, 400m rise, has three or four cells in the vertical depending on where along the slope a column is taken. The upper negative cells seem to merge with the help of the one from the right side. The strength of this side is much less than what it would be in the previous domain, as is consistently seen for this side. A final point to note is the bottom cells do not meet exactly at the ridge crest. In fact, the left-flank's cell protrudes over the ridge peak though it has the weaker magnitude of  $\psi = 7.4 m^2/s$ , which is roughly half the right-flank's extrema.

The other three cases do well to show the variety of differences from the portion just described. The top left snapshot of Figure 5.12a shows an example of the flow from the right side extending over the peak to the left. The other two, while not

exactly centered show the upslope flows colliding only slightly to the right peak. The ratio between the extrema has a wide range with the top right case having very similar extrema for  $\psi$ , yet the bottom left has an even wider deviation than the first, over a factor of 3 change. Investigating these show one commonality between all four, the right side is always stronger than the left as alluded to before. The explanation for this consistency can be approached from two directions and also identify a limitation of the setup. In all these cases the stronger bottom cell forms over the longer and shallower slope, and so the weaker cell is over the shorter one. Obviously a long steep slope can not be included with a short shallow one while maintaining a single periodic domain.

However, it can be seen that relative magnitudes from individual slope simulations cannot simply carry over. Dependencies between cell strength and length covered by sloping topography have already been shown and can be seen again here. The steepest slopes, up to twice the slope of the right, will then have as little as half the length and should be comparable to that seen in the small domain cases studied before. This dependency is directly related to the consistency in the location of the streamfunction's strongest point. In all the periodic cases, the most extreme value for  $\psi$  was not only always on the right, but the value was consistently similar to that of the simulation done in the closed slope-type domain. This consistency provides some motivation for why only the right sides of the periodic results were analyzed for comparison with previous results, Figure 5.13. This choice is further justified due to the sloping region staying constant, at 80km. As noted before, Sec 5.2.3, the length of slope does have an effect so the restriction to the right flank helps ensure that the comparisons are being made between like portions.

One plot was redone from each of the topography and diffusion sections, adding the data from periodic runs. Figure 5.13a shows the comparison for the streamfunction minima as it depends on the diffusion maximum. The circles identify the slope-type domain runs from before with their linear trends as solid lines. The periodic simulations are searched for  $\psi_{min}$  just as before as the method will still find it above the right-side slope. An additional variation between the data plotted is the angle of

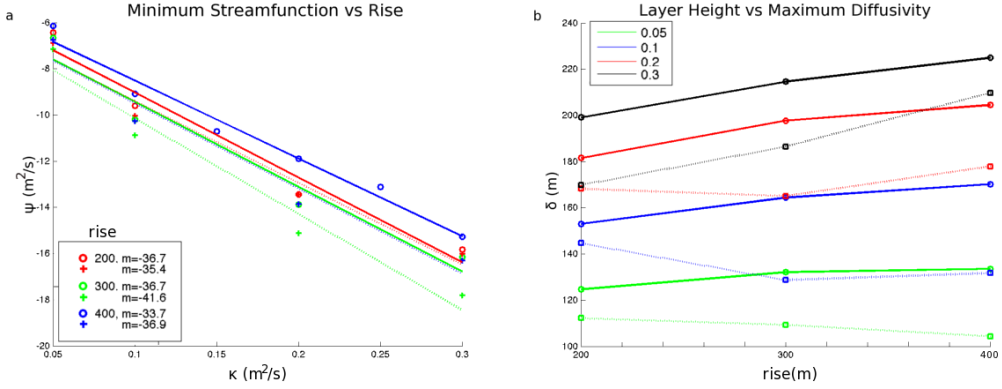


Figure 5.13: Repeats two previous figures adding data from periodic-domain simulations. A) The left figure shows that the linear trends from the slope-type model holds for the simulations when just considering the right half of the periodic domain. Circles show the slope-type simulations and their linear regression, pluses show the periodic data. Slope angles for the simulations are relative to rises of 200, 300, and 400m. In addition the slope of the linear regressions are shown for each. B) The right plot repeats a topographic dependence and while showing significant difference shows the ridge-type model has the extrema consistently shallower than the slope-type.

the opposite side of the flank. The simulation series for 200 and 300m rise are both opposing flow generated over an equivalent 400m rise, while the 400m is opposite a 600m rise. Again noting that slope length has an effect, the three flanks of 400m rise are three different lengths.

Comparing the magnitudes of streamfunction minima, the simulations from the periodic domain are consistently more intense but very similar to the previous findings and are plotted with pluses. Another way to see the similarity between them is in the slope predicted by the linear regression, listed in the figure's legend. All paired series show less than a 10% difference greatly supporting the same dependence controlling the streamfunction in both. While the sign of the difference in slope is different for the shallow case, the ridge-type model is completely consistent in having stronger flow up the right slope, even when fighting an opposing flow.

From inspection of Figure 5.12 the dominance of negative (blue) values of streamfunction is very apparent, yet can be misleading as to where the upslope actually stops. The layer height of the periodic simulations is still comparable to the closed domain, as seen in Figure 5.13b plotted against topographic rise. The previous slope-type domain results are plotted with solid lines, while the ridge-type data are connected with dotted lines. The most prominent trend seen in this plot is that the ridge-type model has upslope layer that is consistently thinner than the corresponding closed simulation. Though not so similar that one could identify individual periodic simulations given the series from the slope-type simulations, the  $\kappa_{max}$  triplets connected are distinguishable.

The examination of the right-flank of the periodic models shows some additional complexities, as is expected of any model extension, yet the previous dependencies are still present. The addition of counter flows, forming on the left-flank, having nonuniform slope lengths should be expected to force these results to diverge. The observed discrepancies did not appear connected to the upper domain, which was able to contain a nonzero mean flow due to the periodicity. This background flow is thought to be a considerable improvement for this model extension, and the absence of influence support the robustness of the previous results. In addition to these, the significance of the lower cells must not be overlooked. Whether on the flank against or with the background flow and no matter the diffusion, all simulations developed non-negligible flux up the slopes over both short and long flanks.



## Chapter 6

# Summary and Discussion

The numerical studies of this thesis were based around characteristics of canyons in the Brazil Basin such as the one shown in Figure 1.6 (p.10). An idealized version of this canyon was created as an initial parameterization of a well established model, checkpoint 63a of the MITgcm [Marshall *et al.*, 1997]. Preliminary investigation on the sensitivity of the parameters both showed the model could realistically represent the dynamics occurring with a deep ocean canyon and established a base case for further investigation of this area. Though some purely numeric features presented themselves within the results, particularly in the vertical velocity field, they are explained away by the representation of topography by the z-coordinates within the model and correspondingly did not appear within the second model and its terrain following mesh.

Use of this second model repeated many of the steps of the MITgcm after the extra steps involved in its creation. This time the model used was developed specifically for the purpose of simulating the area in this study. Using a finite element approach called for a variational form of equations. Such a form was derived in terms of streamfunction and vorticity with an equation for potential temperature completing this system. The FEniCS project, version 0.9.10+ [Logg, 2007], was used in creating the model by automating the processes tabulating the finite elements and reducing the equations, (4.10) (p. 49), to a series of linear algebra problems that were solved numerically. In addition it provided a front end that handled the

communication between its parts and third party software including the PETSc routines used in the computation of the reduced linear algebra problems. Comparison between this model with the MITgcm confirmed that both models were descriptions of the same situation, as intended.

This redundancy between models strengthens the confidence in the trends resulting from this investigation and their application to actual MOR canyons. Having this for support, several parameters were looked at in detail pertaining to the physical situation. The results concerning slope length will be discussed before reverting to the order of study in which they were originally presented (Sec. 5.2, p. 71). This change is because an assertion here illuminates important restrictions on the relevance of the remaining results. After that, cases for the diagnostics' dependence on enhanced diffusion and slope angle of topography will be made.

The slope length was determined to have a significant impact on the dynamics, though it was not a focus of investigations covered from the literature. The main simulations varying this parameter kept the aspect ratio the same, and so the domain height varied along with the length itself. When considering the original equations 2.2 (p.23), it may appear that changing both length and height would cloud any result, yet the nondimensionalized form of (4.6) (p.47) make it clear that this method is only altering a single parameter. Two domain sizes besides the base case were tested, each having a factor of two difference in the simulated domains, a small 50km long case and a large 200km one. Comparing these lengths to the physical observation, even the large domain has a slope much shorter than the full flank of the MOR, which can be around to 1000km in the Atlantic. Yet when looking at the Brazil Basin canyon (Figure 1.6, p. 10), using 100km resolution is still too coarse to capture all the features seen. The influence such changes in length make, plus the inconsistency for parameterizing these regions as scale increases, make conclusions less generalizable than might be hoped. Referring back to Figure 5.9 (p.83), two counteracting trends are competing as resolutions improve. Improved bathymetry means the slope lengths will decrease, else the bathymetry itself is not actually improving, but it also implies steeper slopes are includes. The two possibilities to

obtain the average slope angle of a coarse resolution are the mean of steep and shallow slopes or the mean of multiple steep slopes, of both positive and negative sign. This means that, although slope length decreasing produces a weakening flow and increased variability in  $\psi_{min}$ , (5.9a-c), increasing slope angle can save the conclusions. The second row of the figure, (5.9d-f), shows how the dependence on slope length decreases with increased slope, as well as the magnitude of  $\psi_{min}$  increasing. The competing influences of the related changes from resolution improvement make the situation complex. Determining which effect has larger influence undoubtedly depends on the specifics of the topography itself. Even so, the reduction from length is at least partially countered by the steepening slopes that must occur, reestablishing some of the significance of simulations with coarse bathymetry.

Diffusion is known to be a key factor within overturning circulation and the same is true within the model, though for the latter the dependence is implicit, being the only forcing included. The first relationship investigated was the dependence of  $\kappa_{max}$  on the overall strength of the streamfunction. It was shown that increasing diffusivity increased the strength; a relationship that simplified well to a linear proportionality. The diagnostic  $\psi_{min}$  is a proxy for an average flux within the canyon and was unexpectedly similar to a proportionality used by Wunsch [1970]. It is unexpected because the dependency resulting from Wunsch's derivation breaks down at small angles in the range of those simulated here. Though the smaller slopes have weaker fits, it is thought that the higher order terms of the linearization are not yet dominating. This stretch of previous theory inspired an even bigger deviation in trying to apply the estimation of boundary thickness from Phillips *et al.* [1986] to other simulations. While not expected to apply, the similar nature of their domain suggested the possibility of a similar theoretical form. A power law type behavior does appear to be behind the dependence of layer thickness, and although the regressions to a  $\kappa^{1/4}$  works there is little confidence behind the choice of power.

The estimates of slope itself have a complex relationship with the magnitude of the upward flow, but seemingly straightforward dependence to layer height. For

the range of slopes simulated, there is a definite linear trend between rise and layer height, as was shown in Figure 5.7 (p. 80). In summary of the previous chapter's expansion, an increase of slope directly implies that there is more flux in the vertical over a given horizontal distance. Assuming that the situation allows it to exist, this additional vertical flow should communicate farther into the interior simply through inertia. This type argument has limitations dependent on the velocities themselves which will eventually start slowing along with slope, but it is thought to hold if the velocity does not decrease with angle. Making use of the results from Peacock *et al.* [2004] which used physical experiments focused primarily around much larger slopes, they report that velocity increases with angle until it peaks at around  $3^\circ$ . This slope is a full order of magnitude greater than the base case, but it must be noted they indicate that their critical slope is expected to have an (unspecified) dependence on the Rayleigh number which is several orders of magnitude different than the simulations of this study.

The less understood dependence on topography appears in the diagnostic  $\psi_{min}$ , which is split into two distinct regions. The first region contains a local maximum occurs near a rise of 250, aligning over all the diffusivities, and ending at a local min at 400m or after depending on the diffusivity. While the dependencies governing the partitioning of  $\psi_{min}$  in terms of slope angle are unclear, the amount of variability increasing with diffusivity is a definitive relationship. This is not actually a new result, simply the way the previous linear relationship between  $\kappa_{max}$  and  $\psi_{min}$  manifests with the addition of second variable. Previously, the strong fit for these linear trends brushed over the fact the slope of the linear fits increased between series of increasing topographic rise. This increase is the variability seen when plotted against rise, which supports the flux being dependent on a nonlinear term including both slope and diffusion.

The models were then extended to periodic domains to evaluate the generalizability of the previous results. Many of the trends noted remained if the results were simplified while focusing on the signal present within the closed domain case. These additional simplifications, while necessary for comparison, do greatly increase

the possible influence of observer bias. That being noted, the reduction to half the domain which is most similar to the previous case is done systematically and, after this change, the original diagnostics apply directly. These diagnostics show similar trends as before; the cell strength increases linearly in response to diffusivity in close agreement to the closed domain cases. The dependence of layer height is decidedly weaker, which is not surprising since there is a portion of the domain working against the flow. Even so,  $\delta$  of the periodic cases is easily comparable with that of the closed domain cases. Together, the simulations in a periodic domain show shifted values, relative to the cases with single flank in a closed domain, but overall are similar in terms of dependencies.

A natural continuation for generalizing the patterns would be to have fully open boundary conditions. This is expected to be an improvement beyond that of the periodic simulations, in that the domain remains the same as in the closed case while including restratification effects of incoming flow. While extending the model into a third dimension increases the realism, of course, and improves any conclusions, such an extension is not as easily comparable with the bulk of simulations done here. Like the increased observer bias with the periodic domain, other simplifications are needed for these extensions. The biggest addition a three dimensional model allows is thought to be the addition of Coriolis forcing, the absence of which restricted the results from this thesis to an average-sense within the up-canyon flow.

Even without these extensions, an improvement on understanding the dynamics of abyssal circulation has been made. The picture of deep circulation, originated from Stommel's [1958] theory has been evolving through the help of many. Numerical work, ex. [Bryan, 1987; Marotzke and Scott, 1999; Fedorov *et al.*, 2007], has shown the importance of localized areas having enhanced dynamics, particularly with respect to vertical diffusivity. Studies on energetics, like [Munk and Wunsch, 1998; Huang, 1999; Wunsch and Ferrari, 2004; Dell, 2010] added to this discussion and support the possibility for the intense local boundary areas to be part of the main pathway to mix the ocean. Observations [Polzin *et al.*, 1997; Mauritzen *et al.*, 2002] made near rough topography further emphasize the impor-

tance of bottom enhanced mixing and the addition it makes to the picture of circulation. Using the observational description of the Brazil Basin [Thurnherr *et al.*, 2005; Thurnherr and Speer, 2003] as a foundation, this thesis has shown that upslope flows are easily formed given stratification, mixing and sloping bathymetry. Significant upslope flow formed for all diffusivities and slopes simulated. The weakest flows within the reported simulations obtain fluxes of at least  $0.1Sv$ , which is in agreement with estimates based of measurements, ( $0.1Sv$  [Polzin *et al.*, 1996]) and penetrated more than 100 meters above the actual topography. These flows, even if weaker from the smaller scales of true bathymetry, should persist in canyons prevalent throughout the ocean basin, shown in Figure 1.5 (p.8). When integrated this should contribute significantly to the ocean's circulation.

# Bibliography

- [Armi, 1978] L. Armi. Some evidence for boundary mixing in the deep ocean. *Journal of Geophysical Research*, 83(C4):1971–1979, April 1978.
- [Boning *et al.*, 1995] C. W. Boning, W. R. Holland, F. O. Bryan, G. Danabasoglu, and J. C. McWilliams. An overlooked problem in model simulations of the thermo-haline circulation and heat transport in the Atlantic Ocean. *Journal of Climate*, 8:515–523, March 1995.
- [Bryan, 1987] F. Bryan. Parameter sensitivity of primitive equation ocean general circulation models. *Journal of Physical Oceanography*, 17:970–985, 1987.
- [Bryden and Nurser, 2004] H. L. Bryden and A. J. George Nurser. Effects of strait mixing on ocean stratification. *Journal of Physical Oceanography*, 33:1870–1872, August 2004.
- [Cummins and Foreman, 1998] P. F. Cummins and M. G. G. Foreman. A numerical study of circulation driven by mixing over a submarine bank. *Deep-Sea Research I*, 45:745–769, 1998.
- [de Verdiere, 1988] A. C. de Verdiere. Buoyancy driven planetary flows. *Journal of Marine Research*, 46:215–265, 1988.
- [Dell, 2010] R. W. Dell. Abyssal mixing from bottom boundary effect in mid-Atlantic ridge flank canyons. Master’s thesis, Massachusetts Institute of Technology; Woods Hole Oceanographic Institute, 2010.

- [Fedorov *et al.*, 2007] A. Fedorov, M. Barreiro, G. Boccaletti, R. Pacanowski, and S. G. Philander. The freshening of surface waters in high latitudes: Effects on the thermohaline and wind-driven circulations. *Journal of Physical Oceanography*, 37:896–907, April 2007.
- [Gade and Gustafsson, 2004] H. G. Gade and K. E. Gustafsson. Application of classical thermodynamic principles to the study of oceanic overturning circulation. *Tellus*, 56A:371–386, 2004.
- [Garrett *et al.*, 1993] C. Garrett, P. MacCready, and P. Rhines. Boundary mixing and arrested ekman layers: Rotating stratified flow near a sloping boundary. *Annual Reviews of Fluid Mechanics*, 25:291–323, 1993.
- [Garrett, 2001] C. Garrett. An isopycnal view of near-boundary mixing and associated flows. *Journal of Physical Oceanography*, 31:138–142, January 2001.
- [Geuzaine and Remacle, 2011] Christophe Geuzaine and Jean-François Remacle. Gmsh. <http://geuz.org/gmsh/>, 2011.
- [Gregg, 1987] M.C. Gregg. Diapycnal mixing in the thermocline: A review. *Journal of Geophysical Research*, 92(C5):524905286, 1987.
- [Hogg and Owens, 1999] N. G. Hogg and B. Owens. Direct measurement of the deep circulation within the Brazil Basin. *Deep-Sea Research II*, 46:335–353, 1999.
- [Huang and Jin, 2002] R. X. Huang and X. Jin. Deep circulation in the South Atlantic induced by bottom-intensified mixing over the midocean ridge. *Journal of Physical Oceanography*, 32:1150–1164, April 2002.
- [Huang, 1999] R. X. Huang. Mixing and energetics of the oceanic thermohaline circulation. *Journal of Physical Oceanography*, 29:727–746, April 1999.
- [Ivey and Corcos, 1982] G. N. Ivey and G. M. Corcos. Boundary mixing in a stratified fluid. *Journal of Fluid Mechanics*, 121:1–26, 1982.
- [Ivey, 1987] G. N. Ivey. Boundary mixing in a rotating, stratified fluid. *Journal of Fluid Mechanics*, 183:25–44, 1987.

- [Ledwell and St. Laurent, 2011] J. R. Ledwell and L. C. St. Laurent. Diapycnal mixing in the antarctic circumpolar current. *Journal of Physical Oceanography*, 41:241–246, 2011.
- [Ledwell *et al.*, 2000] J. R. Ledwell, E. T. Montgomery, K. L. Polzin, Louis C. St. Laurent, R. W. Schmitt, and J. M. Toole. Evidence for enhanced mixing over rough topography in the abyssal ocean. *Nature*, 403:179–182, January 2000.
- [Logg and Wells, 2010] A. Logg and G. N. Wells. DOLFIN: Automated finite element computing. *ACM Transactions on Mathematical Software*, 37(2), 2010.
- [Logg, 2007] A. Logg. Automating the finite element method. *Arch. Comput. Methods Eng.*, 14(2):93–138, 2007.
- [Marotzke and Scott, 1999] J. Marotzke and J. R. Scott. Convective mixing and the thermohaline circulation. *Journal of Physical Oceanography*, 29:2962–2970, November 1999.
- [Marshall *et al.*, 1997] J. Marshall, A. Adcroft, C. Hill, L. Pererlman, and C. Heisey. A finite-volume, incompressible Navier Stokes model for studies of the ocean on parallel computers. *Journal of Geophysical Research*, 102(C3):5753–5766, March 1997.
- [Mauritzen *et al.*, 2002] C. Mauritzen, K. L. Polzin, M. S. McCartney, R. C. Millard, and D. E. West-Mack. Evidence in hydrography and density fine structure for enhanced vertical mixing over the Mid-Atlantic Ridge in the western Atlantic. *Journal of Geophysical Research*, 107(C10), 2002.
- [MIT, 2011] MIT. Mitgcm manual. [http://mitgcm.org/sealion/online\\_documents/manual.html](http://mitgcm.org/sealion/online_documents/manual.html), 2011.
- [Munk and Wunsch, 1998] W. Munk and C. Wunsch. Abyssal recipes II: energetics of tidal and wind mixing. *Deep-Sea Research I*, 45:1977–2010, 1998.
- [Munk, 1966] W. Munk. Abyssal recipes. *Deep-Sea Research*, 13:707–730, 1966.

- [NOAA, 2011] NOAA. The first climate model. [http://celebrating200years.noaa.gov/breakthroughs/climate\\_model/welcome.html](http://celebrating200years.noaa.gov/breakthroughs/climate_model/welcome.html), April 2011.
- [P-OMIP, 2003] P-OMIP. Pilot ocean model intercomparison project. [http://research.iarc.uaf.edu/pomip/page.php?fig=MOC\\_Global\\_2000](http://research.iarc.uaf.edu/pomip/page.php?fig=MOC_Global_2000), July 2003.
- [Peacock *et al.*, 2004] Thomas Peacock, Roman Stocker, and Jeff M. Aristoff. An experimental investigation of the angular dependence of diffusion-driven flow. *Physics of Fluids*, 16(9):3503–3505, September 2004.
- [Phillips *et al.*, 1986] O. M. Phillips, J.-H. Shyu, and H. Salmun. An experiment on boundary mixing: mean circulation and transport rates. *Journal of Fluid Mechanics*, 173:473–499, 1986.
- [Phillips, 1970] O. M. Phillips. On flows induced by diffusion in a stably stratified fluid. *Deep-Sea Research*, 17:435–443, 1970.
- [Polzin *et al.*, 1996] K. L. Polzin, K. Speer, J. M. Toole, and R. W. Schmitt. Intense mixing of Antarctic Bottom Water in the equatorial Atlantic Ocean. *Nature*, 380:54–57, March 1996.
- [Polzin *et al.*, 1997] K. L. Polzin, J. M. Toole, J. R. Ledwell, and R. W. Schmitt. Spatial variability of turbulent mixing in the abyssal ocean. *Science*, 276:93–96, 1997.
- [Ramsden, 1995] D. Ramsden. Response of an oceanic bottom boundary layer on a slope to interior flow. part I: Time-independent interior flow. *Journal of Physical Oceanography*, 25:1672–1687, July 1995.
- [Smith and Sandwell, 1997] W. H. F. Smith and D. T. Sandwell. Global seafloor topography from satellite altimetry and ship depth soundings. *Science*, 277:1956–1952, 1997.
- [St. Laurent and Thurnherr, 2007] L. C. St. Laurent and A. Thurnherr. Intense mixing of lower thermocline water on the crest of the Mid-Atlantic Ridge. *Nature*, 448:680–683, August 2007.

- [St. Laurent *et al.*, 2001] L. C. St. Laurent, J. M. Toole, and R. W. Schmitt. Buoyancy forcing by turbulence above rough topography in the abyssal Brazil Basin. *Journal of Physical Oceanography*, 31:3476–3495, December 2001.
- [Stommel and Arons, 1960a] H. Stommel and A. B. Arons. On the abyssal circulation of the world ocean - I stationary planetary flow patterns on a sphere. *Deep-Sea Research*, 6(2):140–154, 1960.
- [Stommel and Arons, 1960b] Henry Stommel and A. B. Arons. On the abyssal circulation of the world ocean - II an idealized model of the circulation pattern and amplitude in oceanic basins. *Deep-Sea Research*, 6(3):217–237, 1960.
- [Stommel and Arons, 1972] Henry Stommel and A. B. Arons. On the abyssal circulation of the world ocean - V the influence of bottom slope on the broadening of inertial boundary currents. *Deep-Sea Research*, 19:707–718, 1972.
- [Stommel, 1958] H. Stommel. The abyssal circulation. *Deep-Sea Research*, 1958.
- [Thurnherr and Speer, 2003] A. Thurnherr and K. Speer. Boundary mixing and topographic blocking on the Mid-Atlantic Ridge in the South Atlantic. *Journal of Physical Oceanography*, 33:848–862, April 2003.
- [Thurnherr *et al.*, 2005] A. Thurnherr, L. C. St. Laurent, K. Speer, J. M. Toole, and J. R. Ledwell. Mixing associated with sills in a canyon on the midocean ridge flank. *Journal of Physical Oceanography*, 35:1370–1381, August 2005.
- [Thurnherr *et al.*, 2008] A. Thurnherr, G. Reverdin, P. Bouruet-Aubertot, L. C. St. Laurent, A. Vangriesheim, and V. Ballu. Hydrography and flow in the lucky strike segment of the mid-atlantic ridge. *Journal of Marine Research*, 66:347–372, 2008.
- [Thurnherr, 2011] A. Thurnherr. personal communication, 2011.
- [Turner, 1979] J.S. Turner. *Buoyancy effects in fluids*. Cambridge University Press; Cambridge, 1979.

- [Vallis, 2006] G. K. Vallis. *Atmospheric and Oceanic Fluid Dynamics*. Cambridge University Press, 2006.
- [Wunsch and Ferrari, 2004] C. Wunsch and R. Ferrari. Vertical mixing, energy, and the general circulation of the oceans. *Annual Reviews of Fluid Mechanics*, 36:281–314, 2004.
- [Wunsch, 1970] C. Wunsch. On oceanic boundary mixing. *Deep-Sea Research*, 17:293–301, 1970.
- [Wunsch, 2002] C. Wunsch. What is the thermohaline circulation? *Science*, 298:1179–1180, November 2002.